

# Enhanced upwelling of Antarctic Bottom Water by topographic interaction of water mass interfaces

Lois Elizabeth Baker<sup>1</sup>, Ali Mashayek<sup>1</sup>, and Alberto C. Naveira Garabato<sup>2</sup>

<sup>1</sup>Imperial College London

<sup>2</sup>University of Southampton

December 14, 2022

## Abstract

The lower cell of the meridional overturning circulation (MOC) is sourced by dense Antarctic Bottom Water (AABW), which forms and sinks around Antarctica and subsequently fills the abyssal ocean. For the MOC to ‘overturn’, these dense waters must upwell through mixing with lighter waters above. Here, we investigate the processes underpinning such mixing, and the resulting water mass transformation, using an observationally forced, high-resolution numerical model of the Drake Passage in the Southern Ocean. In the Drake Passage, the mixing of dense AABW formed in the Weddell Sea with lighter deep waters transported from the Pacific Ocean by the Antarctic Circumpolar Current is catalysed by energetic flows impinging on rough topography. We find that multiple topographic interaction processes act to facilitate mixing of the two water masses, ultimately resulting in upwelling of waters with neutral density greater  $28.19 \text{ kg m}^{-3}$ , and downwelling of the lighter waters above. In particular, we identify the role of sharp density interfaces between AABW and overlying waters, and find that the dynamics of the interfaces’ interaction with topography can enhance mixing. Such sharp interfaces between water masses have been observed in several parts of the global ocean, but are unresolved and unrepresented in ocean and climate models. We suggest that they are likely to play an important role in abyssal dynamics and mixing, and therefore require further exploration.

1 **Enhanced upwelling of Antarctic Bottom Water by**  
2 **topographic interaction of water mass interfaces**

3 **L. E. Baker<sup>1</sup>, A. Mashayek<sup>1</sup>, A. C. Naveira Garabato<sup>2</sup>**

4 <sup>1</sup>Imperial College London, United Kingdom

5 <sup>2</sup>University of Southampton, Southampton, United Kingdom

6 **Key Points:**

- 7 • Sharp density interfaces exist between Antarctic Bottom Water and overlying Cir-  
8 cumpolar Deep Water in the Drake Passage  
9 • The sharpness of the interfaces leads to rich submesoscale and internal wave dynamics  
10 and complex topographic interactions  
11 • Such dynamics may contribute significantly to upwelling of Antarctic Bottom Water

---

Corresponding author: Lois Baker, [l.baker18@imperial.ac.uk](mailto:l.baker18@imperial.ac.uk)

## Abstract

The lower cell of the meridional overturning circulation (MOC) is sourced by dense Antarctic Bottom Water (AABW), which forms and sinks around Antarctica and subsequently fills the abyssal ocean. For the MOC to ‘overturn’, these dense waters must upwell through mixing with lighter waters above. Here, we investigate the processes underpinning such mixing, and the resulting water mass transformation, using an observationally forced, high-resolution numerical model of the Drake Passage in the Southern Ocean. In the Drake Passage, the mixing of dense AABW formed in the Weddell Sea with lighter deep waters transported from the Pacific Ocean by the Antarctic Circumpolar Current is catalysed by energetic flows impinging on rough topography. We find that multiple topographic interaction processes act to facilitate mixing of the two water masses, ultimately resulting in upwelling of waters with neutral density greater  $28.19 \text{ kg m}^{-3}$ , and downwelling of the lighter waters above. In particular, we identify the role of sharp density interfaces between AABW and overlying waters, and find that the dynamics of the interfaces’ interaction with topography can enhance mixing. Such sharp interfaces between water masses have been observed in several parts of the global ocean, but are unresolved and unrepresented in ocean and climate models. We suggest that they are likely to play an important role in abyssal dynamics and mixing, and therefore require further exploration.

## Plain Language Summary

Dense, cold waters are formed near Antarctica, then sink and spread through the deep ocean. The global overturning circulation is maintained by the upwelling of these dense waters back to the surface. This circulation allows the abyssal ocean to exchange heat, carbon and other tracers with the upper ocean and atmosphere, and is therefore a key regulator of the climate system. The upwelling happens due to turbulence in the deep ocean mixing together dense waters with lighter waters above. This turbulent mixing is often caused by the interaction of currents with rough seafloor topography, but the processes and resulting upwelling are not well understood. In this study, we use a high-resolution, realistic numerical simulation to investigate the processes causing turbulent mixing and upwelling of dense waters in an energetic region of the Southern Ocean. We find that there are sharp interfaces between the Antarctic-sourced dense waters and the overlying lighter waters, and that these interfaces themselves play a dynamic role in generating turbulent mixing and upwelling. The interfaces are not resolved or represented in global climate models, so their impact on the deep-ocean circulation requires further exploration.

## 1 Introduction

Sea ice formation and surface cooling near Antarctica create the densest waters in the global ocean (Marshall & Speer, 2012; Talley, 2013; A. C. Naveira Garabato et al., 2014). These Antarctic Bottom Waters (AABW) sink and travel northwards below the lighter water masses, filling most of the abyssal ocean with dense, cold, relatively fresh water (Lumpkin & Speer, 2007; Johnson, 2008; Talley, 2013). Such formation of AABW feeds the lower cell of the meridional overturning circulation (MOC). For these waters to upwell back to the surface (for if they did not, the ocean would fill up with dense waters), they must first upwell across density surfaces by transforming diabatically to lighter waters. Once they are sufficiently light, they then enter the upper cell of the MOC, where they are drawn adiabatically to the surface by westerly winds in the Southern Ocean (Toggweiler, 1994; Marshall & Speer, 2012; Talley, 2013). This overturning circulation ventilates the ocean abyss on timescales of centuries to millennia, with leading-order climatic consequences for the deep-ocean storage and release of carbon, heat and other tracers (Talley, 2013; Rae et al., 2018; Skinner et al., 2010).

The primary mechanism by which AABW can upwell across density surfaces is thought to be turbulent diapycnal mixing (Munk & Wunsch, 1998; Wunsch & Ferrari, 2004; De

62 Lavergne et al., 2016; Meredith & Naveira Garabato, 2021), the other non-negligible (yet  
63 secondary) mechanism being geothermal heating (Emile-Geay & Madec, 2009; Mashayek  
64 et al., 2013; Mashayek, Salehipour, et al., 2017; De Lavergne et al., 2016; Cimoli et al.,  
65 2019). Turbulent diapycnal mixing in the ocean occurs when small-scale turbulence causes  
66 irreversible mixing of fluids with different densities. Observations show that this turbulent  
67 mixing is enhanced by several orders of magnitude within a few hundred metres of the  
68 seafloor, compared to at mid-depths (Polzin et al., 1997; Ledwell et al., 2000; A. Naveira  
69 Garabato et al., 2004; J. MacKinnon et al., 2013; Waterhouse et al., 2014; J. A. MacKinnon  
70 et al., 2017). This is due to turbulent processes generated by the interaction of currents  
71 and tides with topography at the sea floor. These processes include internal waves, which  
72 are thought to be a primary source of mixing in the ocean interior (Wunsch & Ferrari,  
73 2004; J. A. MacKinnon et al., 2017; Sarkar & Scotti, 2017; Whalen et al., 2020), and other  
74 non-propagating boundary dynamics such as hydraulic processes (Baines, 1995; Legg &  
75 Klymak, 2008; Alford et al., 2013; Klymak, 2018) and Ekman layers (Garrett et al., 1993;  
76 A. C. Naveira Garabato et al., 2019; Spingys et al., 2021).

77 However, the implication of turbulent processes being bottom-generated is that the  
78 turbulent diffusivity increases towards topography, which induces downwelling rather than  
79 upwelling across density surfaces (Polzin et al., 1997; L. C. St. Laurent et al., 2001; De  
80 Lavergne et al., 2016; Ferrari et al., 2016). This apparent conundrum can be resolved by  
81 realising that, in some boundary layer next to topography, waters cannot become denser,  
82 and so must become lighter by mixing with waters above them, thereby inducing upwelling  
83 (Ferrari et al., 2016; McDougall & Ferrari, 2017). In recent years, there has been a significant  
84 focus on the nature of diapycnal mixing and density stratification in the bottom boundary  
85 layer, due to its key role in facilitating upwelling of dense waters, as reviewed by Polzin  
86 and McDougall (2022). The processes through which near-boundary waters mix, re-stratify  
87 and are exchanged with the ocean interior, and how those processes vary geographically  
88 throughout the global ocean, are a key open question.

89 The difficulty in answering this question resides in the extreme challenge involved in ob-  
90 serving turbulence in the abyssal ocean, particularly close to the seafloor. From a modelling  
91 perspective, high-resolution, process-resolving numerical simulations must be idealised and  
92 small-scale due to computational limitations, while more realistic simulations lack accurate  
93 parameterizations for mixing processes below the grid-scale. In this study, we use a realistic,  
94 wave- and submesoscale-resolving simulation to shed light onto the abyssal processes that  
95 generate mixing and drive transformation of AABW, as this water mass flows northwards  
96 through the Southern Ocean. We choose to study the Drake Passage, a region of intense  
97 flow-topography interaction and diapycnal mixing.

98 The Drake Passage is the gap between the tip of South America and the Antarctic  
99 Peninsula, through which the energetic Antarctic Circumpolar Current (ACC) flows from  
100 west to east. Rough topography including ridges, seamounts and abyssal hills (see figures  
101 1b,d) obstructs the deep layers of the ACC, generating intense diapycnal mixing in the  
102 bottom 1-2 km (A. Naveira Garabato et al., 2004; L. St. Laurent et al., 2012; Sheen et  
103 al., 2013; Mashayek, Ferrari, et al., 2017; Mackay et al., 2018). It is thought that the main  
104 contributor to mixing at depth in the Drake Passage is the breaking of internal lee waves  
105 generated by the impingement of the vigorous mesoscale eddies of the ACC upon the rough  
106 topography (L. St. Laurent et al., 2012; Sheen et al., 2013; Nikurashin & Ferrari, 2010),  
107 although the ways in which lee waves lose energy to diapycnal mixing are still not well  
108 understood (Legg, 2021).

109 The impact of concentrated ‘hotspots’ of topographic mixing, such as the Drake Pas-  
110 sage, on global deep-water upwelling has long been recognised (Munk & Wunsch, 1998).  
111 In addition, increased tracer residence time near large-scale ridges and fracture zones has  
112 been shown to contribute to enhanced diapycnal tracer transport in the Drake Passage  
113 (Mashayek, Ferrari, et al., 2017). This makes the Drake Passage an important location, not

114 only for transformation of dense bottom waters, but also for upwelling of climate-critical  
115 tracers such as heat, carbon and nutrients (Tamsitt et al., 2017).

116 The singular role of the Drake Passage in mixing AABW is partly due to its location. It  
117 is on the northward path of the dense AABW that is formed in the Weddell Sea to the south,  
118 called Weddell Sea Deep Water (Sievers & Nowlin, 1984; A. C. Naveira Garabato, Heywood,  
119 & Stevens, 2002, hereafter, NG02a). In the Drake Passage, Lower Circumpolar Deep Water  
120 (LCDW) sits above AABW, having entered the passage from the Pacific Ocean to the west.  
121 AABW occupies only the south-east part of the Passage (NG02a), so the AABW/LCDW  
122 interface directly impinges on the rough Drake Passage topography, experiencing high levels  
123 of topographically enhanced turbulent diapycnal mixing as a result. However, the processes  
124 by which the mixing at this interface takes place are not well understood. Furthermore, the  
125 boundary layer adjacent to topography in which diapycnal upwelling is expected to happen  
126 exists over a wide range of depths in the Passage, so it is not clear which density classes can  
127 be expected to upwell, and which may instead downwell.

128 Here, we investigate how flow-topography interaction processes in the Drake Passage act  
129 to mix AABW with the overlying LCDW, and quantify the resulting water mass transfor-  
130 mation. Although the Drake Passage is an energetic region, AABW export and northward  
131 transport occur in every major ocean basin, so it is expected that the dynamics described  
132 here are not unique, and could be of more generic importance to the transformation of  
133 AABW as it navigates the ACC and rough topography of the Southern Ocean.

## 134 2 Drake Passage Simulation

135 We use a wave-resolving model of the Drake Passage, described in detail in Baker and  
136 Mashayek (2022) (see Appendix A for summary). The simulation is performed using the  
137 hydrostatic configuration of the Massachusetts Institute of Technology general circulation  
138 model (MITgcm, Marshall et al., 1997), with  $0.01^\circ$  horizontal resolution (600 m to 1100 m)  
139 and 225 vertical levels with variable resolution that is  $< 25$  m at all depths above -4500 m  
140 (the range of depths relevant to this work). The depth and main bathymetric features are  
141 shown in figure 1d. Figure 1b shows a daily average of vertical vorticity in the simulation  
142 domain, demonstrating the interaction of deep-reaching mesoscale eddies with the rough  
143 topography.

144 The simulation is based upon a similar simulation that was developed as part of the  
145 DIMES (Diapycnal and Isopycnal Mixing Experiment in the Southern Ocean) field pro-  
146 gramme (Mashayek, Ferrari, et al., 2017). The DIMES experiment included a release in  
147 2009 of an anthropogenic tracer in the deep ACC upstream of Drake Passage, and subse-  
148 quent measurements of tracer concentration throughout the southeastern Pacific and the  
149 Scotia Sea over the following years, to investigate the impact of turbulent mixing. The mea-  
150 sured tracer distribution was used to infer turbulent diapycnal diffusivities (Watson et al.,  
151 2013; Zika et al., 2020), along with independent microstructure measurements of diffusivity  
152 (L. St. Laurent et al., 2012; Sheen et al., 2013; Merrifield et al., 2016), which are compared  
153 to our model diffusivity in figure 1c. Mashayek, Ferrari, et al. (2017) showed that their  
154 version of this model reproduced the spreading of the DIMES tracer using an imposed di-  
155 apycnal diffusivity distribution based on observations. The current version of the model has  
156 increased vertical resolution, allowing a better representation of topographically generated  
157 processes such as lee waves, and an improved sponge layer to reduce spurious processes at  
158 the open boundaries. We also use an online parameterization of diapycnal diffusivity (to be  
159 discussed later) rather than a static ‘map’, in order to represent the mixing associated with  
160 instability of resolved small-scale processes.

161 The simulation starts in July 2009 (corresponding to the period following the DIMES  
162 tracer release), and is integrated for 100 days. We use the final 30 days of the simulation

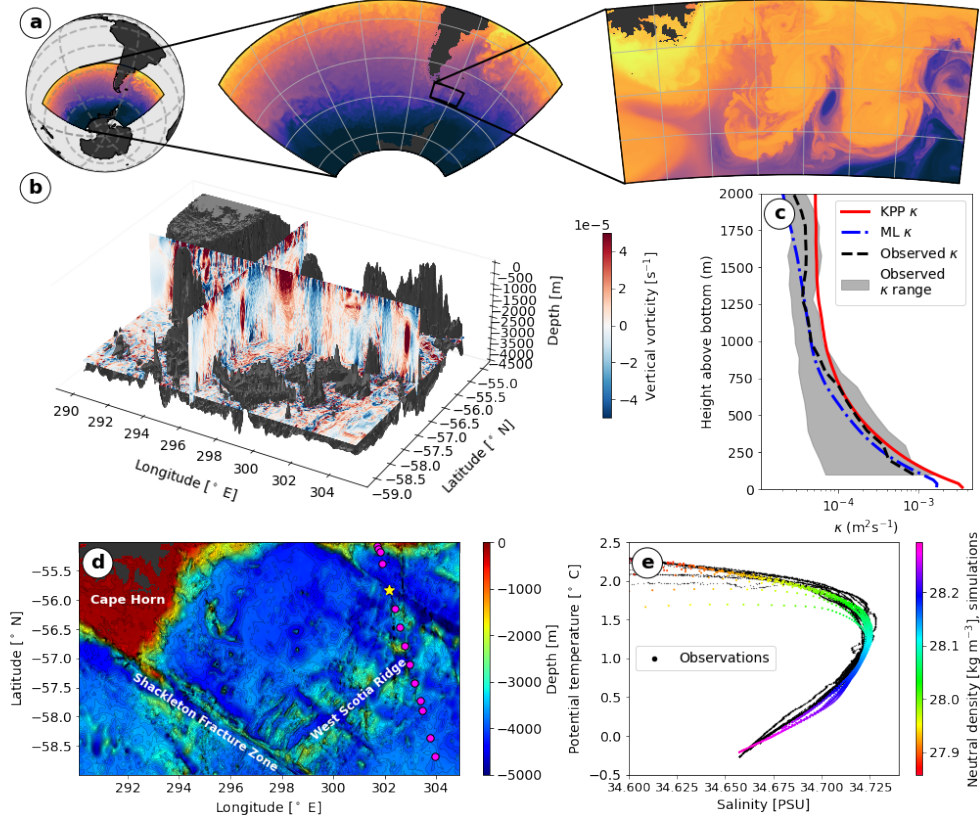


**Figure 1.** (a) Nesting diagram for Drake Passage model, showing parent simulation domain (left) and the Drake Passage domain presented here (right). (b) A daily average of vertical vorticity in the model. (c) Comparison of parameterized KPP diffusivity averaged with reference to height above bottom over the domain with microstructure observations from the Drake Passage (Merrifield et al., 2016) and a machine learning estimate of diffusivity (see §7). (d) Map of the simulation domain; shading and contours show depth. SR1b section stations are shown in pink, and the yellow star indicates the station at which profiles in figure 4 are taken. (e) Temperature-salinity diagram for the SR1b section observations and simulation data shown in figure 2. Simulation data are shaded with neutral density.

163 (early September to early October) for our analyses, with numbering of days referring to  
 164 days from the start of this selected period.

165 The model is nested within a simulation of a larger region of the Southern Ocean,  
 166 described in Tulloch et al. (2014) and shown in figure 1a. The larger simulation is itself  
 167 forced at the open boundaries by restoring velocity, temperature and salinity to the Ocean  
 168 Comprehensive Atlas (OCCA), a 3-year-long ocean state estimate that assimilated altimeter  
 169 data, satellite sea surface temperature, and Argo profiles (Forget, 2010). The hydrography  
 170 and eddy kinetic energy of the larger simulation was verified against observations by Tulloch  
 171 et al. (2014). Neither this simulation, nor ours, includes tidal forcing, thus the interaction  
 172 of tides with topography and corresponding generation of internal tides is not represented  
 173 in our model.

174 Our nested simulation uses open boundary conditions derived from the parent sim-  
 175 ulation for sea surface height, potential temperature, salinity, and meridional and zonal  
 176 velocities. In addition, a restoring boundary condition creates a sponge layer of 1 degree  
 177 thickness (removed for analysis purposes, except in figure 3) in which the potential tem-  
 178 perature, salinity, and zonal and meridional velocities are relaxed to the parent simulation.  
 179 The model hydrography is therefore expected to be realistic, and can be compared to in-situ  
 180 observations.

181 To validate the salinity, potential temperature, and neutral density in our simulation,  
 182 we use a set of shipboard conductivity-temperature-depth (CTD) observations that were  
 183 performed as part of the ACCLAIM (Antarctic Circumpolar Current Levels by Altimetry  
 184 and Island Measurements) project along the SR1b section in the Drake Passage in November  
 185 2009. The stations at which observations were taken are shown in figure 1d. We sample  
 186 our simulation at these locations for a like-for-like comparison, and in both cases compare  
 187 potential temperature, practical salinity, and neutral density (Jackett & McDougall, 1997).  
 188 The date of the fields sampled in our simulation is 10<sup>th</sup> October 2009 (day 30), which is  
 189 close to the observations in November 2009.

190 Figure 2 shows the observational data (left) and simulation data (right). Although  
 191 expectedly not identical (see later discussion of temporal variation of deep-ocean water  
 192 masses), there is very good agreement in temperature, salinity, and neutral density. In both  
 193 cases, a bottom layer of fresh, cold, dense water underlies saltier, warmer, lighter waters. A  
 194 temperature-salinity diagram (figure 1e) for the observations (black) and simulation (colour)  
 195 at the locations in figure 2 confirms the agreement between observations and simulation.

196 Turbulent processes and their associated mixing are not explicitly resolved in the model,  
 197 and must be parameterized. Typically, transition to turbulence occurs due to increased  
 198 vertical shear (shear instability), or unstable buoyancy gradients (convective instability),  
 199 although other instability mechanisms such as symmetric and inertial instabilities can also be  
 200 the primary cause of instability in geophysical flows, leading to secondary shear or convective  
 201 instabilities (Thomas et al., 2013; A. C. Naveira Garabato et al., 2019). The susceptibility of  
 202 flows to be unstable to shear and convective instabilities can be captured by the Richardson  
 203 number  $Ri = N^2/S^2$ , which quantifies the ratio of the stabilising effect of stratification  $N^2$  to  
 204 the destabilising squared vertical shear of horizontal velocities  $S^2$ . The stratification  $N^2 =$   
 205  $\partial b/\partial z$  is defined to be the vertical gradient of buoyancy  $b = -\rho g/\rho_0$ , where  $\rho$  is the density  
 206 and  $\rho_0$  is a reference density, and the squared shear is given by  $S^2 = (\partial u/\partial z)^2 + (\partial v/\partial z)^2$ ,  
 207 where  $u$  and  $v$  are the zonal and meridional velocities respectively.

208 Stratified shear instability can be shown analytically to be possible below a critical  
 209 Richardson number  $Ri_c = 0.25$  by the Miles-Howard Theorem (Miles, 1961; Howard, 1961),  
 210 although at finite model resolution it is not clear what  $Ri_c$  should be, and several shear  
 211 instabilities can occur for  $Ri \sim O(1)$  (Caulfield, 2021). Convective instability occurs when  
 212  $Ri < 0$ , corresponding to unstable vertical buoyancy gradients with  $N^2 < 0$ . Susceptibility  
 213 to submesoscale instabilities, such as symmetric and inertial instabilities, can also be quan-

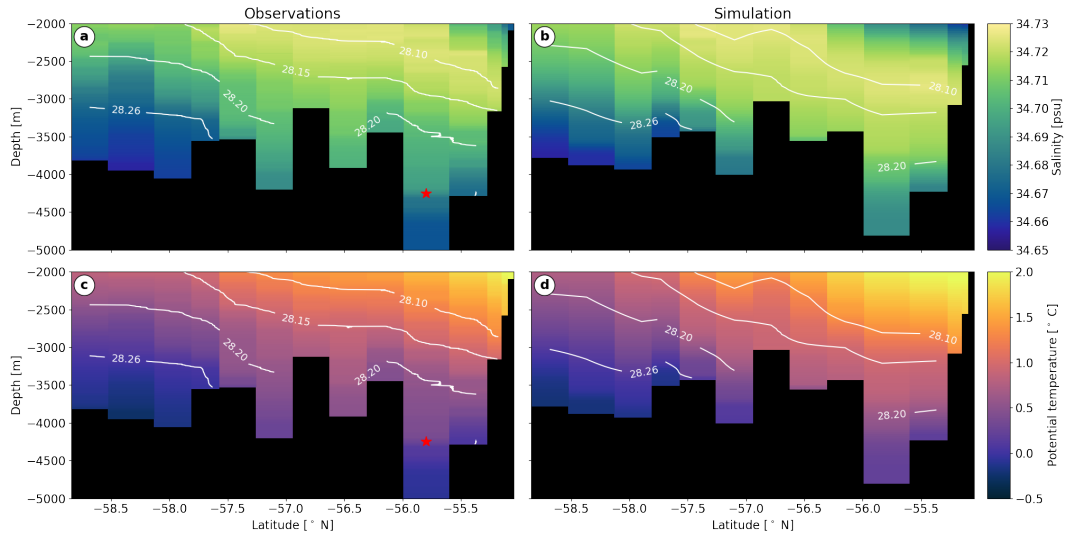


**Figure 2.** Comparison of (top) salinity and (bottom) potential temperature between (right) simulation and (left) observations. Contours indicate neutral density. Observations are from the SR1b section, collected in November 2009 as part of cruise JR195 of the ACCLAIM project, with locations shown in figure 1d. Simulation data are from a daily average on day 30, corresponding to 10<sup>th</sup> October 2009, and sampled at the same locations as the observations.

214 tified using a Richardson number criterion, which reduces to  $Ri < 1$  for larger-scale flows  
 215 in which the Earth’s rotation dominates inertial forces (Thomas et al., 2013). Support for  
 216 a criticality condition in  $Ri$  being appropriate in an oceanic context is given by evidence  
 217 for ‘marginal instability’; that is, observations of the Richardson number in an oceanic flow  
 218 fluctuating close to some critical value, typically near 0.25 (Thorpe & Liu, 2009; Smyth,  
 219 2020; Mashayek, Baker, et al., 2022).

220 The essence of  $Ri$  criticality is captured by the  $K$ -profile parameterization (KPP) (Large  
 221 et al., 1994), which enhances the vertical diffusivity  $\kappa$  when  $Ri < Ri_c$ . Here, we use the  
 222 KPP parameterization with  $Ri_c = 1/3$ , which is a reasonable measure of turbulence stabil-  
 223 ity in an environment when some background turbulence exists; see Mashayek et al. (2021);  
 224 Mashayek, Baker, et al. (2022) for a discussion. In order to validate the use of this parame-  
 225 terization, we compare diffusivity averaged in height-above-bottom coordinates throughout  
 226 our domain with DIMES observational, microstructure-based estimates of diffusivity in the  
 227 Drake Passage obtained by Merrifield et al. (2016). Figure 1c shows these profiles, which,  
 228 subject to observational uncertainty, assumptions with respect to mixing efficiency (Osborn,  
 229 1980; Gregg et al., 2018), and the known temporal and spatial variability of mixing events  
 230 (Moum, 2021), confirm that KPP does a satisfactory job in this domain, at least when  
 231 averaged with reference to height above bottom.

232 We parameterize mixing in this way to support our goal of demonstrating the processes  
 233 that lead to the transformation of AABW. However, in §7, we discuss the sensitivity of water  
 234 mass transformation to the parameterization of mixing, by presenting an independent, offline  
 235 machine learning estimate of diffusivity in our domain. This will highlight the need for more  
 236 sophisticated parameterization of oceanic processes at the sub-grid-scale of ocean models.

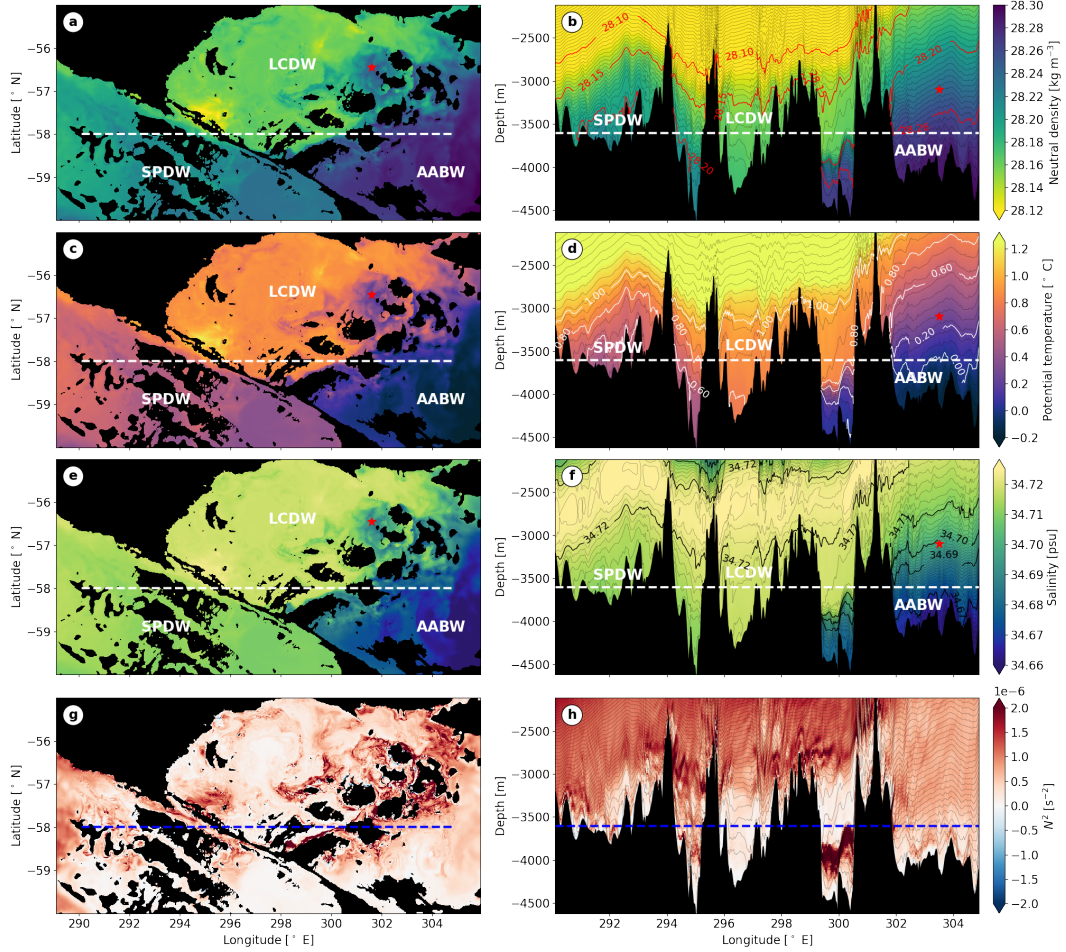


**Figure 3.** (a,b) Neutral density, (c,d) potential temperature, (e,f) salinity, and (g,h) stratification  $N^2$  at (left column) 3600 m depth and (right column)  $-58^\circ$  N. White and blue dashed lines show correspondence between columns. Red stars indicate locations of mixed AABW/SPDW referred to in the main text. A corresponding movie is available in the supporting information (movie S1).

237

### 3 Water mass classification

238

239

240

241

242

243

244

245

246

247

The Southern Ocean connects the major ocean basins (with the exception of the Arctic), and is a hub for global deep water masses. The lack of continental boundaries at the latitude band of the Drake Passage allows the strong westerly winds to draw deep isopycnals up to the surface, along which the deep waters of the global ocean can upwell and ventilate at the surface (Toggweiler, 1994; Lumpkin & Speer, 2007). The Drake Passage region is home to several distinct water masses formed in different parts of the global ocean. These water masses can be identified by their temperature, salinity and density properties, as well as by tracers such as oxygen, silicate and others (Tomczak & Large, 1989; Purkey et al., 2018; Liu & Tanhua, 2021). Here, we focus on temperature, salinity and neutral density, as tracers that can be calculated from our model.

248

249

250

251

The primary water mass of the Drake Passage, and of the Southern Ocean, is Circumpolar Deep Water (CDW), which is advected around the Southern Ocean by the ACC. The denser class of this CDW is called Lower Circumpolar Deep Water (LCDW), and occupies the neutral density range between  $28.0 \text{ kg m}^{-3}$  and  $28.26 \text{ kg m}^{-3}$  (NG02a). LCDW is

252 characterised by a salinity maximum that is derived from North Atlantic Deep Water in the  
 253 Atlantic sector (Sievers & Nowlin, 1984, NG02a). A. C. Naveira Garabato, McDonagh, et  
 254 al. (2002) (hereafter, NG02b) define LCDW in the Drake Passage as having salinity gen-  
 255 erally above 34.70, exceeding 34.73 at its mid-depth maximum, and potential temperature  
 256 between 0.2 and 1.9° C. An additional dense variety of LCDW in the Drake Passage result-  
 257 ing from interaction of LCDW with the deep waters of the Ross Sea was defined by Sievers  
 258 and Nowlin (1984). This Southeast Pacific Deep Water (SPDW) is characterised by neutral  
 259 densities between 28.2 and 28.26 kg m<sup>-3</sup>, and is colder than 0.6 °, and fresher than 34.71  
 260 (NG02a).

261 AABW is defined by NG02a to have neutral densities greater than 28.26 kg m<sup>-3</sup>. In the  
 262 Drake Passage, the relevant variety of AABW is Weddell Sea Deep Water (WSDW), which  
 263 is formed in the Weddell Sea to the south of the Drake Passage by the mixing of dense,  
 264 shelf-derived Weddell Sea Bottom Waters with CDW. WSDW flows northward at depth  
 265 over the South Scotia Ridge and into the Scotia Sea before reaching the Drake Passage  
 266 (NG02b). Using a global simulation with a tracer injection in the Weddell Sea, Solodoch  
 267 et al. (2022) showed that WSDW travels only downstream of the Drake Passage, with high  
 268 concentrations in the Atlantic basin, and eventually occupying the Indian basin and west  
 269 Pacific basin. WSDW is fresher, colder and denser than the overlying LCDW.

270 Figures 3a,c,e show neutral density, potential temperature, and salinity at 3600 m depth  
 271 in the simulation. At this depth, there is a clear demarcation of three distinct water masses,  
 272 separated from each other by the north-west/south-east running ridge of the Shackleton  
 273 Fracture Zone, and the south-west/north-east running West Scotia Ridge system (see figure  
 274 1d for labelling of bathymetric features). The vertical structures of these water masses  
 275 are illustrated in figures 3b,d,f, with the dashed lines showing the depth and latitudinal  
 276 correspondence between the left and right columns. Movie S1 shows some of these panels  
 277 over a 30-day period, and reveals that the locations and depths of the water masses vary  
 278 with time.

279 With reference to the above definitions of Drake Passage water masses, figure 3b shows  
 280 that most of the domain below 2000 m depth is filled with LCDW. The salinity maximum  
 281 described above that is characteristic of LCDW is evident in figure 3f, and has a value of  
 282 34.73. The denser, fresher waters of the LCDW below 28.2 kg m<sup>-3</sup> can be identified as  
 283 SPDW. At 3600 m depth, there is a clear lateral boundary (seen in figures 3a,c,e) between  
 284 the denser SPDW and the lighter class of LCDW, formed by the ridge of the Shackleton  
 285 Fracture Zone. The denser SPDW is unable to overflow this ridge, so the basin in the north  
 286 of the domain is filled with the lighter LCDW only, as can be seen in figures 3b,d,f.

287 The neutral density contour of 28.26 kg m<sup>-3</sup>, potential temperature contour of 0.2°C,  
 288 and salinity contour 34.69 are almost co-located, consistent with the definition by NG02b,  
 289 of the boundary between LCDW and the colder, fresher WSDW. WSDW is only present in  
 290 the south-east of the domain, consistent with its origin in the Weddell Sea and westward  
 291 path from the South Scotia Ridge to the Drake Passage. From figure 3a,c,f, it is clear that  
 292 WSDW is also topographically bounded - to the west from the SPDW by the Shackleton  
 293 Fracture Zone, and to the north-west by the West Scotia Ridge. Some lighter WSDW does  
 294 however overflow the West Scotia Ridge, in particular during a significant event around day  
 295 20 (visible in movie S1, and to be discussed further in §5.3.2). This highlights the temporal  
 296 variability of the water mass locations.

## 297 4 Stratified water mass interfaces

298 There are often sharp interfaces between the different water masses in the simulation,  
 299 with corresponding high stratification due to their differing densities. Figures 3g,h show that  
 300 stratification is enhanced at several interfaces in the domain. The elevated stratification is  
 301 due to sharp gradients in both salinity (figure 3b) and temperature (figure 3d). This is

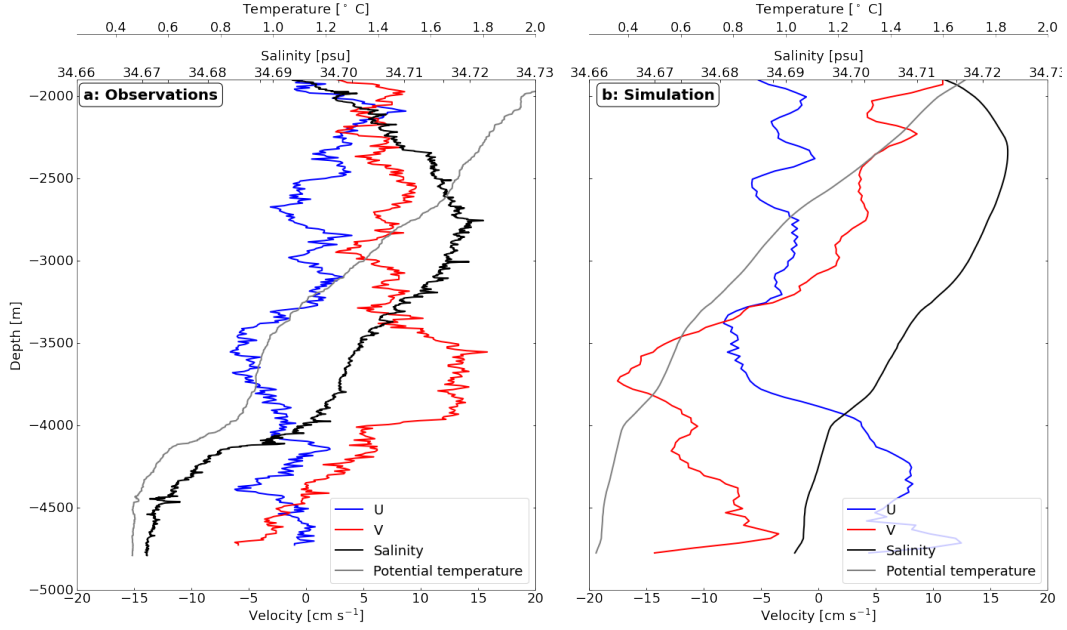


**Figure 4.** Velocity, temperature and salinity profiles at the location shown by the yellow star in figure 1d. Steps in temperature and salinity are accompanied by strong vertical shear of horizontal velocities. (a) In-situ observational data from DIMES, March 2013; and (b) simulation data on day 0.

302 consistent with the observations of Sievers and Nowlin (1984), who, on investigating the  
 303 various water masses of the Drake Passage, found that they were generally separated by  
 304 highly stratified interfaces, which they termed stability strata.

305 Steps in salinity and temperature have been previously observed at many locations in  
 306 the global ocean, and interpreted as boundaries between water masses; in particular in the  
 307 Drake Passage (Sievers & Nowlin, 1984), the East Scotia Sea (Meredith et al., 2013), and  
 308 the South West Atlantic (Reid et al., 1977). In the observations shown in figure 2a,c, sharp  
 309 gradients in temperature and salinity are also visible, for example at the location marked  
 310 by a red star.

311 In a different set of observations along transect SR1b, taken by the DIMES project  
 312 in March 2013, there are similar steps in temperature and salinity at depth, which were  
 313 co-located with high vertical shear as measured with a lowered acoustic Doppler current  
 314 profiler (ADCP). These steps and the corresponding velocities are shown in figure 4a, with  
 315 one such step and associated sharp vertical velocity gradient located just below 4000 m  
 316 depth. A corresponding profile at the same location from the simulation is shown in figure  
 317 4b, also demonstrating a step in temperature and salinity just above 4000 m depth, with  
 318 co-located vertical gradients in horizontal velocities. The occurrence of vertical shear of  
 319 horizontal velocities at a sharp density interface might be expected if the interface is tilted  
 320 horizontally, creating a strong horizontal buoyancy gradient and thereby vertical shear, in  
 321 order to maintain thermal wind balance. We will later demonstrate this mechanism using  
 322 the simulation.

323 The presence of sharp interfaces between water masses and the corresponding high  
 324 stratification, both in observations and in our model, is of great interest, as it is likely to  
 325 relate to how AABW mixes with overlying waters. Can the sharpness of an interface give

us insight into the mixing that its bounding water masses have experienced in the past, or are there other mechanisms that generate and destroy strong interfacial gradients?

There is evidence in the simulation (for example, at locations marked with a red star in figure 3) of waters that have properties intermediate between those of WSDW and LCDW. These waters are lighter than  $28.26 \text{ kg m}^{-3}$  (i.e. lighter than WSDW), but are also fresher than the freshest LCDW (SPDW) entering from the west of the domain. Thus, the waters in question are likely to be the result of WSDW mixing with the LCDW above. NG02a note that the WSDW entering the Drake Passage from the east is the lightest fraction of WSDW overflowing the South Scotia Ridge from the Weddell Sea, and is warmer and more saline than ‘pure’ WSDW following intense diapycnal mixing with LCDW (specifically, SPDW) on its westward transit to the Drake Passage. The easternmost part of the domain shown in figure 3b,d,f,h does not exhibit a sharp interface between AABW and SPDW, suggesting that the water masses have been rather thoroughly mixed.

However, elsewhere in the domain, strongly stratified interfaces do exist, albeit not always exactly aligned with the definitions given above for the LCDW/SPDW/WSDW boundaries (e.g., see figure 3h). These interfaces are also present in the larger SO simulation in which this model is nested (see §2 and figure 1a), which can resolve them with its vertical resolution of 50 m. The interfaces may therefore be inherited from observations via this larger model and the ocean state estimate with which it is itself forced. Although it is possible that the sharp interfaces are purely inherited remnants of the initial meeting of the distinct water masses (and a lack of mixing between such waters), the spatial heterogeneity of interface sharpness points to the leading-order involvement of a dynamical mechanism besides mixing. In the upper ocean, frontogenesis is well known to sharpen pre-existing horizontal density gradients (Hoskins, 1982; McWilliams, 2021), and there is also evidence of frontogenesis acting at submesoscale fronts in the ocean interior (Siegelman et al., 2020). It is clear from figure 3h that interfaces are often tilted from the horizontal. This is likely due to the flow moving over large-scale bottom topography, geographical variations in the water mass locations, and the passing of mesoscale eddies. The horizontal tilting of interface results in horizontal density gradients; frontal processes may therefore occur in the deep ocean to sharpen or widen these ambient gradients.

A further implication of the occurrence of water mass interfaces is the modification of dynamics associated with the layer of high stratification itself. Next, we investigate the potential impact of water mass interfaces on mixing processes in the deep ocean.

## 5 The phenomenology of topographic mixing

We wish to understand how different physical processes contribute to enhancing turbulence near topography. As discussed in §2, the Richardson number  $Ri = N^2/S^2$  can be used to quantify the susceptibility of a flow to shear and convective instabilities, and it is a Richardson number-based criterion that informs the mixing parameterization in the model. We therefore consider mechanisms that decrease stratification  $N^2$  and increase vertical shear  $S^2$  as a proxy for enhancing diapycnal mixing on the sub-grid-scale.

### 5.1 The nature of modelled mixing

Figure 5 and the corresponding movie S2 illustrate the complex dynamics of flow-topography interaction in the simulation. Figure 5a shows the Richardson number, and figure 5b the corresponding vertical diffusivity  $\kappa$ , for an hourly average of a section of the simulation at  $-57^\circ$  N. In general,  $\kappa$  is at its background value of  $5 \times 10^{-5} \text{ m}^2 \text{ s}^{-1}$  outside of the bottom few hundred metres, and outside of the upper-ocean mixed layer (not shown), corresponding to Richardson numbers greater than the critical value  $Ri_c = 1/3$  used here. In some locations, breaking topographic waves enhance  $\kappa$  up to 1000 m above the bottom. Within the bottom few hundred metres,  $\kappa$  is enhanced by the KPP

375 parameterization due to shear instability ( $0 < Ri < Ri_c$ ) or convective instability ( $Ri < 0$ ).  
 376 From consideration of the stratification (figure 5c) and squared vertical shear (figure 5d), it is  
 377 clear that many of the areas of enhanced  $\kappa$  are due to both high shear and low stratification,  
 378 acting together to decrease  $Ri$ . Furthermore, figure 5c shows that there are several areas of  
 379 unstable stratification close to the boundary, indicating conditions for convective instability  
 380 and overturning. These patches of  $N^2 < 0$  are a feature throughout the domain, and play  
 381 an important role in the near-boundary dynamics.

To understand how these areas of convective instability form, we can consider the simple unforced buoyancy equation:

$$\frac{\partial b}{\partial t} = -\mathbf{u} \cdot \nabla b + \frac{\partial}{\partial z} \left( \kappa \frac{\partial b}{\partial z} \right), \quad (1)$$

where  $b$  is buoyancy,  $\mathbf{u}$  is velocity, and the horizontal component of diffusion is taken to be zero, since the vertical gradients of the density and turbulent density flux tend to dominate over the horizontal components (Ferrari et al., 2016). Taking the vertical derivative, we obtain:

$$\frac{DN^2}{Dt} = - \underbrace{\frac{\partial \mathbf{u}_H}{\partial z} \cdot \nabla_H b}_{(A)} - \underbrace{\frac{\partial w}{\partial z} N^2}_{(B)} + \underbrace{\frac{\partial^2}{\partial z^2} (\kappa N^2)}_{(C)}, \quad (2)$$

382 where  $D/Dt \equiv \partial/\partial t + \mathbf{u} \cdot \nabla$  is the full derivative following a water parcel, and  $H$  represents  
 383 the horizontal components of velocity and the gradient operator.

384 Each of the three terms on the right hand side of equation (2) represents a way in  
 385 which the stratification following a water parcel can change. Term (C) encapsulates verti-  
 386 cal diffusion, and it is through this term that turbulent processes (represented within the  
 387 parameterized turbulent diffusivity  $\kappa$ ) act to diffuse vertical gradients in buoyancy, thereby  
 388 causing irreversible mixing. The vertical gradients of  $\kappa$  and  $N^2$  and corresponding turbu-  
 389 lent buoyancy fluxes play a leading-order role in the boundary layer dynamics (Polzin &  
 390 McDougall, 2022). However, this term alone cannot change the sign of  $N^2$  from positive  
 391 to negative. Suppose that (A) and (B) are zero, and that initially  $N^2 > 0$  everywhere  
 392 except on the boundary, and zero at the boundary itself since there should be no buoyancy  
 393 flux across the boundary (an insulating boundary condition). Then, suppose that at some  
 394 interior location  $N^2$  becomes zero. Given  $\kappa \geq 0$ , this point is thus a local minimum of  $\kappa N^2$ ,  
 395 so (C) is greater than zero, and  $DN^2/Dt \geq 0$  by equation (2), hence the sign of  $N^2$  cannot  
 396 change.

397 Similarly, term (B), which represents changes to the vertical buoyancy gradient due  
 398 to vertical convergence or divergence of the vertical velocity, cannot alone change the sign  
 399 of  $N^2$ . If (A) and (C) are zero, the solutions to equation (2) are exponential, and thus  
 400 single-signed.

401 Therefore, term (A) must be responsible for generating areas of convective instability  
 402 from a stable flow. This term corresponds to vertical shear of horizontal velocities acting  
 403 upon horizontal buoyancy gradients, which physical intuition confirms can overturn isopy-  
 404 cnals – by advecting dense water above light water and creating conditions for convective  
 405 instability.

406 An important aspect of term (A) is that, if the velocities and buoyancy gradients are  
 407 in thermal wind balance, such that  $\mathbf{f} \times \partial \mathbf{u}_H / \partial z = -\nabla_H b$ , where  $\mathbf{f} = (0, 0, f)$  with  $f$  as the  
 408 Coriolis parameter, then (A) vanishes and this shear mechanism cannot cause overturning.  
 409 Thus, for convective instability conditions to occur in the absence of forcing (such as surface  
 410 cooling or bottom thermal flux), the flow must be unbalanced; this imbalance could be  
 411 associated with internal gravity waves, fronts, or boundary processes.

412 The preceding analysis serves to highlight the important role of vertical shear in gener-  
 413 ating conditions for instability. Not only is vertical shear needed to destabilise a statically

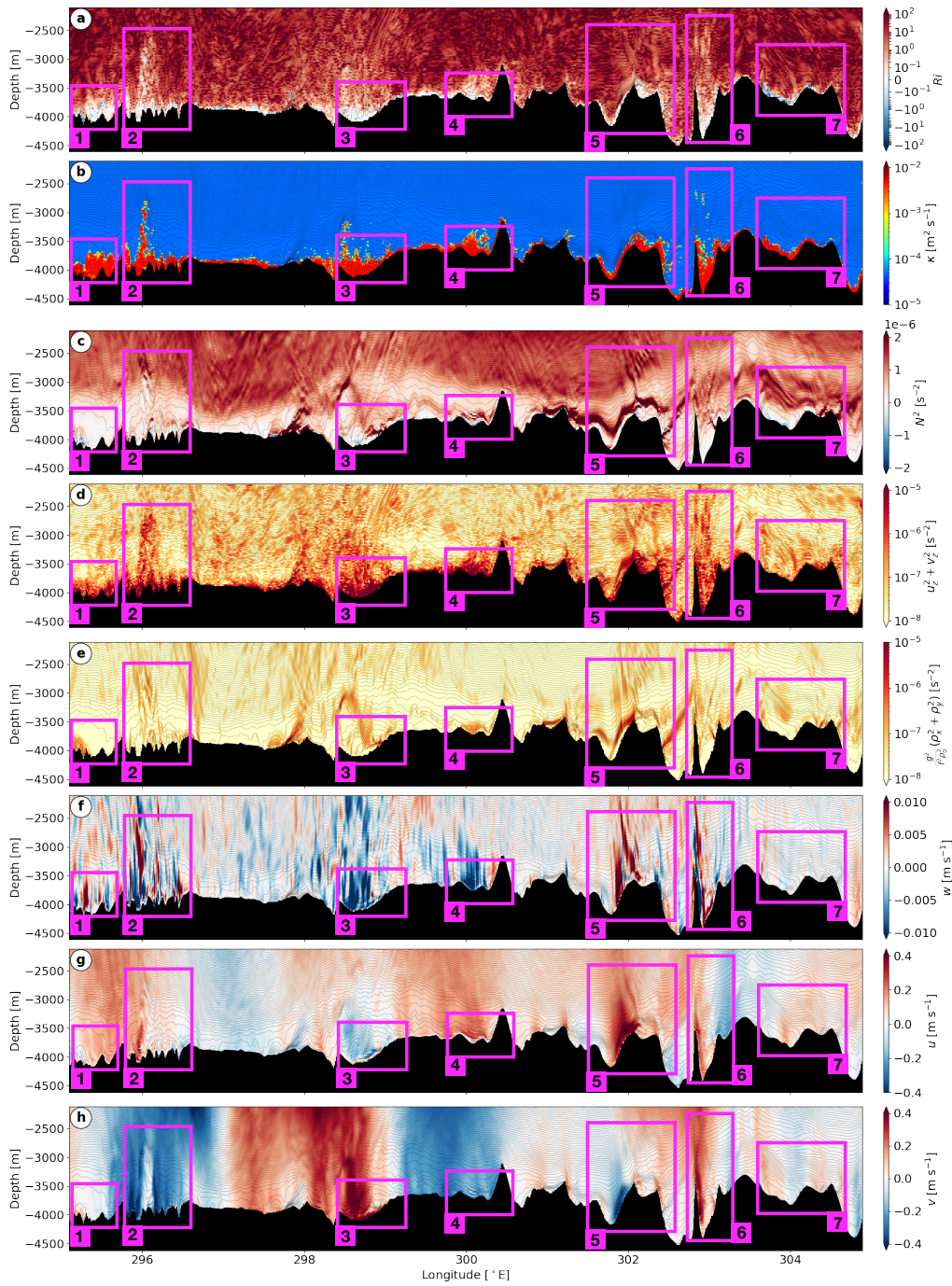


**Figure 5.** Various dynamical variables at  $-57^\circ$  N, demonstrating a range of mixing processes. (a) Richardson number, (b) vertical diffusivity, (c) stratification, (d) squared vertical shear of horizontal velocities, (e) squared vertical shear of horizontal velocities, as implied by the thermal wind balance relation applied to the horizontal density gradients, (f) vertical velocity, (g) zonal velocity, and (h) meridional velocity. Magenta boxes highlight processes discussed in the main text. A corresponding movie is available in the supporting information (movie S2).

414 stable flow via the onset of shear instability, but it is also required to create the conditions  
 415 for convective instability from horizontal buoyancy gradients. Having identified the role of  
 416 vertical shear in creating the conditions for mixing, we now discuss the physical processes  
 417 that govern vertical shear near the boundary.

## 418 **5.2 Topographically-induced processes**

419 First, we consider the complex topographic interaction processes that take place in the  
 420 absence of the highly stratified interfaces separating the different water masses. Then, we  
 421 examine the processes arising from the these interfaces' presence.

### 422 **5.2.1 Boundary layer frictional processes**

423 Wherever a flow encounters a boundary with friction (see Appendix A for a description  
 424 of the modelled no-slip boundary condition), shear may arise as the flow experiences drag  
 425 in a thin boundary layer. This drag alone can be expected to create shear even when the  
 426 topography is flat, and it is clear from figure 5d that vertical shear is always enhanced near  
 427 the boundary.

428 In a rotating geophysical flow, the force balance between friction, rotation, and pressure  
 429 gradients modifies the boundary layer dynamics by generating an Ekman spiral, in which  
 430 the flow turns clockwise (in the Southern Hemisphere) as the boundary is approached. We  
 431 find that the flow direction, averaged over the entire simulation domain, turns on average  
 432  $12^\circ$  clockwise in the bottom 25 m, and on average  $4^\circ$  clockwise in the 25 m above this,  
 433 consistent with Ekman theory. We are therefore permitting Ekman dynamics at the bottom  
 434 boundary, but not fully resolving them, since the depth of the Ekman layer is of the same  
 435 order as the 25 m vertical grid resolution.

436 When the bottom boundary is sloped, these dynamics become more complex yet. A  
 437 cross-slope flow can induce an upslope or downslope Ekman current, which can become ar-  
 438 rested by the restoring buoyancy force on isopycnals (MacCready & Rhines, 1991; Garrett  
 439 et al., 1993; Ruan et al., 2019, 2021). An example of a near-boundary flow that is consistent  
 440 with an unsteady upslope Ekman current is shown by the zonal and meridional velocities in  
 441 figure 5g,h in box 3, in which the flow turns clockwise in the bottom few grid cells, with the  
 442 corresponding enhanced vertical shear shown in figure 5d. Observational evidence suggests  
 443 that a downslope Ekman flow can generate low stratification and large shear near topogra-  
 444 phy, producing conditions favourable for the development of submesoscale instabilities and  
 445 intense mixing in a deep western boundary current (A. C. Naveira Garabato et al., 2019;  
 446 Spingys et al., 2021). Numerical studies also suggest that submesoscale instabilities dur-  
 447 ing Ekman adjustment may have an overlooked role in topographic mixing (Callies, 2018;  
 448 Wenegrat & Thomas, 2020). However, the rough topography and unsteady, energetic nature  
 449 of the flow in the Drake Passage suggests other explanations for the elevated diffusivities  
 450 several hundred metres above topography seen in this model.

### 451 **5.2.2 Lee waves, blocking, and breaking**

452 When stratified flows interact with rough topography, a number of processes can occur  
 453 that generate turbulence and mixing. For topographic wavenumbers  $\mathbf{k}$  such that  $f^2 <$   
 454  $(\mathbf{U} \cdot \mathbf{k})^2 < N^2$ , where  $\mathbf{U}$  and  $N$  are the near-bottom velocity and stratification, vertically  
 455 propagating lee waves are generated. Lee waves extract energy from the mean flow and cause  
 456 turbulent mixing when they break. They are thought to be a leading-order source of mixing  
 457 in the Southern Ocean (A. Naveira Garabato et al., 2004; Scott et al., 2011; Nikurashin &  
 458 Ferrari, 2011; Trossman et al., 2013; De Lavergne et al., 2016).

459 A recent study of the lee wave field in this simulation found that there was strong  
 460 and nonlinear lee wave generation throughout the domain, especially in areas of rough

461 topographic features such as the Shackleton Fracture Zone and the West Scotia Ridge, and  
 462 in areas of high bottom currents (Baker & Mashayek, 2022). The vertical velocity, shown in  
 463 figure 5f, exhibits (for example, box 2) lee waves generated at topography and propagating  
 464 vertically upwards. In this simulation, lee waves can propagate through the entire water  
 465 column and interact with the surface (Baker & Mashayek, 2021).

466 The mechanisms of lee wave breaking and resulting vertical distribution of mixing are  
 467 poorly constrained (Legg, 2021). In the presence of a strong lee wave field in the simulation,  
 468 there is enhanced diffusivity in the bottom 100-400 m (e.g., boxes 1 and 2, figure 5b),  
 469 consistent with the results of Klymak (2018) for idealised simulations with representative  
 470 Southern Ocean parameters and multi-scale topography. The waves generate high shear  
 471 and even areas of static instability in the lee of topography (figure 5c, box 2), and thus  
 472 contribute significantly to mixing near topography.

473 Above the bottom few hundred metres, the modelled lee waves generally do not become  
 474 shear- or convectively unstable, so vertical diffusivity is not enhanced by the KPP parame-  
 475 terization and, instead, the waves experience the background diffusivity. However, in some  
 476 locations, highly nonlinear lee waves do become unstable up to 1000 m above the bottom,  
 477 such as in box 2 (figure 5b,f).

478 The lack of any significant interior lee wave-driven mixing in the simulation suggests  
 479 a need for better parameterization of mixing driven by nonlinear wave interactions in the  
 480 ocean interior in models such as this that resolve only part of the internal wave spectrum.  
 481 However, the ultimate sink for lee wave energy in the interior remains poorly understood.  
 482 Observations in the Drake Passage have shown that rates of dissipation are an order of  
 483 magnitude smaller than would be expected if all lee wave energy was dissipated locally near  
 484 topography, which suggests that the waves have an energy sink elsewhere (Sheen et al., 2013;  
 485 Waterman et al., 2013, 2014; Cusack et al., 2017; Voet et al., 2020; Gutierrez-Villanueva et  
 486 al., 2022).

487 The topographic Froude number  $Fr = Nh/|\mathbf{U}|$ , where  $h$  is the characteristic height  
 488 of topography, indicates the nonlinearity of the generated lee wave field. When  $Fr \gtrsim 1$ ,  
 489 the flow cannot all go over a topographic obstacle, and is instead blocked or split, giving  
 490 rise to non-propagating processes as well as a nonlinear propagating lee wave field. These  
 491 non-propagating processes are also an important source of turbulence and mixing (Klymak,  
 492 2018; Klymak et al., 2021). Such processes include downslope windstorms (Klemp & Lilly,  
 493 1975; Peltier & Clark, 1979; Durran, 1986), hydraulic control and jumps (Winters & Armi,  
 494 2012, 2014), and wake vortices (Srinivasan et al., 2019), which can all generate high shear,  
 495 instabilities, and mixing. Box 6 in figure 5 shows an example of flow interacting with a tall  
 496 topographic feature. At its peak, lee waves are generated (visible in the vertical velocity  
 497 field, figure 5f, box 6), but velocities are accelerated down to the feature's base as the flow  
 498 is topographically steered (figures 5g,h, box 6). This generates shear (figure 5d, box 6) and  
 499 high diffusivity (figure 5b, box 6).

### 500 **5.3 Role of stratified interfaces**

501 The layers of high stratification that separate the various water masses discussed in §3  
 502 can dynamically influence the topographic interaction processes discussed above, as well as  
 503 creating new mechanisms of mixing.

#### 504 **5.3.1 Generation of vertical shear**

505 The interfaces between different water masses can be identified by the layers of high  
 506 stratification in figure 5c and movie S2, panel c. There is not one continuous interface, rather  
 507 several interfaces, separating different layers of fluid that move throughout the domain (as  
 508 illustrated by the salinity in movie S2, panel e). The complex patterns of the areas of high  
 509 stratification in figures 3g,h are further evidence of this. The layers are not horizontal,

510 but undulate with the topography (e.g., figure 5c, box 5), with the geographical location  
 511 of the water masses (e.g., figure 3b), and with the translation of mesoscale eddies through  
 512 the domain. The tilting of these vertically stratified interfaces creates strong horizontal  
 513 buoyancy gradients. In a non-rotating flow, baroclinic production of vorticity would act to  
 514 flatten the tilted isopycnals. However, in a rotating fluid, geostrophic adjustment acts to  
 515 increase vertical shear, such that the horizontal buoyancy gradients approach thermal wind  
 516 balance.

517 Figure 5e shows scaled horizontal buoyancy gradient  $g^2(\gamma_x^2 + \gamma_y^2)/f^2/\rho_0^2$ , where  $g$  is the  
 518 acceleration due to gravity,  $\rho_0$  is a reference density,  $\gamma$  is the neutral density, and subscripts  
 519 denote derivatives. Not only does this figure show that strong horizontal buoyancy gradients  
 520 correspond to the stratified interfaces (e.g. box 5), but it can also be compared to the vertical  
 521 shear in figure 5d. Were the flow in exact thermal wind balance, the two panels d and e  
 522 would be identical. There is a clear correspondence between areas of high vertical shear  
 523 (panel d), high horizontal buoyancy gradients (panel e), and stratified interfaces (panel c).  
 524 The zonal and meridional velocities (panels g and h) also exhibit jets next to topography  
 525 in box 5 due to the locally elevated vertical shear. Observational evidence for vertical shear  
 526 associated with stratified interfaces was presented in figure 4a, and based on this and our  
 527 simulation, we conclude that one of the mechanisms of generating vertical shear in the deep  
 528 ocean is the tilting of water mass interfaces.

529 However, it is not clear that this vertical shear and the interfaces themselves can then  
 530 cause instability. It was already shown in equation (2) that vertical shear in thermal wind  
 531 balance cannot cause overturning, and the interfaces by definition possess large stratification  
 532  $N^2$  alongside high squared vertical shear  $S^2$ ; thus, the Richardson number is not necessarily  
 533 reduced at the interfaces. For example, the regions of high shear in figure 5d, box 5, do not  
 534 correspond to increased diffusivity in figure 5b. Instead, it is the interaction of the interfaces  
 535 with topography that causes instability and generates mixing.

### 536 **5.3.2 Interaction with topography**

537 When the strong horizontal buoyancy gradients of the water mass interfaces interact  
 538 with the rough topography of the Drake Passage, they frequently cause overturning of  
 539 isopycnals and conditions for instability. Areas of unstable stratification near topography  
 540 associated with the passing of horizontal gradients in buoyancy (tilted isopycnals) can be  
 541 seen in figure 5c, boxes 1, 3, 4, and 7, and in movie S2. Friction at the boundary (§5.2.1) or  
 542 small-scale topographic processes such as lee waves (§5.2.2) perturb and sometimes overturn  
 543 tilted isopycnals as a dense water mass moves along topography, leaving behind it weakly  
 544 stratified or unstable fluid. This mechanism relies strongly on the temporal variability of  
 545 the water masses.

546 To demonstrate this temporal variability, we show in figure 6 and movie S3 an example  
 547 of a fast-moving overflow of dense waters over the West Scotia Ridge. As discussed in  
 548 §3, this class of water is lighter than the WSDW to the south-east of the domain, as it  
 549 has mixed with LCDW above. The top row of figure 6 shows salinity at 3600 m depth,  
 550 demonstrating how over a period of seven days, dense, fresh waters that were previously  
 551 trapped by the ridge (e.g., see figure 3c, showing the salinity field on day 0) push through  
 552 the topography and enter the northern part of the domain. This overflowing event is driven  
 553 by fast northward velocities associated with a surface-enhanced mesoscale eddy that spans  
 554 the entire water column (figure 6j,k,l). The corresponding motion of the stratified interface  
 555 over topography contributes to turbulence and mixing in its wake.

556 The second row of figure 6 corresponds to the white dashed lines in the top row, and  
 557 shows the progression of the denser water class as it flows northwards, using salinity as  
 558 a tracer. There are several stratified interfaces, the movement of which is clear from the  
 559 stratification time series in the third row, and from movie S3. Behind (to the south of) the  
 560 contact point of the interfaces with topography, there are areas of negative stratification

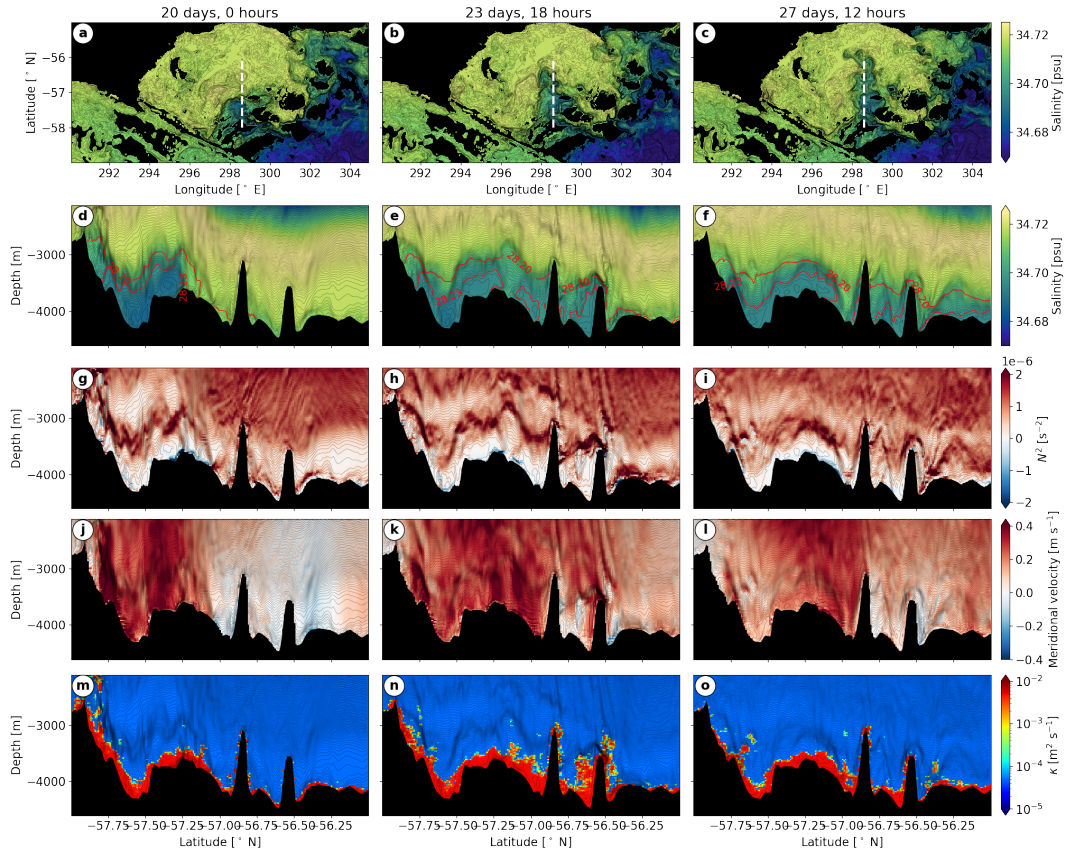


**Figure 6.** Time series (time increasing from left to right) over  $\sim 7$  days of an overflow of AABW passing northwards over the West Scotia Ridge. (a-c) Salinity at 3600 m depth, with white dashed line indicating the section shown in the remaining panels at  $298.6^\circ$  E. (d-f) Salinity, (g-i) stratification (or squared buoyancy frequency), (j-l) meridional velocity and (m-o) vertical diffusivity. All contours show neutral density. A corresponding movie is available in the supporting information (movie S3).

561 caused by the isopycnals overturning with the motion of the front. Beneath the interface,  
 562 after the contact point has passed, the fluid is weakly stratified and the areas of negative  
 563 stratification are persistent, slowly increasing in stability as they are mixed by the enhanced  
 564 vertical diffusivity.

565 The fast flow speeds and tilted isopycnals of the dense bottom current moving over the  
 566 rough topography result in increased diffusivity along the current's path, as shown in the  
 567 bottom row of figure 6. We will later present evidence that this event is associated with  
 568 increased upwelling of the dense waters.

### 569 **5.3.3 Impact on propagating lee waves**

570 The presence of the stratified interfaces near topography can also influence the genera-  
 571 tion, propagation and breaking of lee waves. While the deep ocean is generally considered to  
 572 be weakly and uniformly stratified, the impact of a stratified interface has been extensively  
 573 studied in the context of atmospheric mountain wave generation beneath a temperature  
 574 inversion or the highly stratified stratosphere. The occurrence of hydraulic jumps, breaking  
 575 lee waves, lee wave rotors (flow circulations in the lee of topography), resonant trapped lee  
 576 waves on the interface, and downslope wind storms have been found to be highly dependent  
 577 on the height of the stratified interface, the density difference across the interface, and the  
 578 topographic Froude number  $Fr$  (Klemp & Lilly, 1975; Durran, 1986; Vosper, 2004; Sheri-  
 579 dan & Vosper, 2006). Jagannathan et al. (2020) established that the location of a strong  
 580 density step above topography impacted whether or not it plunged downwards in the lee  
 581 of the topography, thereby giving rise to a wave field aloft that was six times more ener-  
 582 getic than in the absence of interface plunging. Armi and Mayr (2015) found that when a  
 583 strong density step exists above topography, this can act as a 'virtual topography' control-  
 584 ling the stratified flow response aloft. The presence of these density steps in the deep ocean  
 585 could therefore have implications on the way we represent topography in oceanic lee wave  
 586 parameterizations.

587 Away from topography, when encountering a region of high stratification, lee wave  
 588 horizontal velocities increase, resulting in enhanced nonlinearity, wave overturning, and  
 589 turbulence (Durran, 1986). Lee waves may also gain/lose energy to the mean flow or break  
 590 at critical levels through interaction with the vertical shear associated with thermal wind  
 591 balance of the tilted interfaces (Kunze & Lien, 2019; Baker & Mashayek, 2021). Abrupt  
 592 changes to the the mean flow through which lee waves propagate, such as those linked to  
 593 water mass interfaces, are largely neglected in the question of how and where lee waves  
 594 dissipate their energy, but may be important for catalysing wave instability.

595 Evidence of impact of the layers of high stratification on lee waves can be seen in figure  
 596 5. In box 2, a lee wave breaking is evident in the diffusivity (figure 5b) up to the level  
 597 where stratification increases significantly, suggesting that the enhancement in stratification  
 598 may increase nonlinearity of the wave, causing it to lose energy by breaking. In box 5, a  
 599 wave is generated above a strongly stratified interface, suggesting that the interface may be  
 600 acting as a 'virtual topography' (Armi & Mayr, 2015). A large lee wave is also generated  
 601 by the interaction of the front of the dense bottom current with topography in figure 6k  
 602 at  $-56.5^\circ$  N. It is clear that the presence of stratified interfaces in the Drake Passage may  
 603 alter the nature of lee wave generation, propagation and breaking, potentially modifying  
 604 the distribution of lee wave mixing in a way that would be difficult to take into account in  
 605 parameterizations.

## 606 **6 Water Mass Transformation**

607 In order to understand how deep waters are transformed to different densities by diapyc-  
 608 nal mixing, we calculate the water mass transformation rate, equivalent to the diapycnal  
 609 velocity integrated over a density surface. In particular, it is key to elucidate whether waters

610 at some density level upwell (become lighter), or downwell (become denser). This question  
 611 gives rise to a conundrum that has been the topic of active research over the past decade  
 612 (De Lavergne et al., 2016; Ferrari et al., 2016). The diapycnal turbulent flux of buoyancy  
 613  $F_b$  can be approximated using a diffusive flux law,  $F_b = -\kappa N^2$ , where  $\kappa$  is the vertical  
 614 diffusivity (Osborn, 1980). If  $\frac{\partial F_b}{\partial z} < 0$ , then waters become lighter (upwelling), whereas if  
 615  $\frac{\partial F_b}{\partial z} > 0$ , waters become denser (downwelling). Thus, if, as is generally observed,  $\kappa$  signifi-  
 616 cantly increases towards topography without a corresponding decrease in  $N^2$ , then  $\frac{\partial F_b}{\partial z} > 0$   
 617 and downwelling occurs rather than the necessary upwelling.

618 A resolution to this conundrum has been suggested by noting that at the bottom  
 619 boundary, in the absence of geothermal heat flux, an insulating boundary condition implies  
 620 that  $F_b = 0$ . Thus, in some boundary layer,  $F_b$  (which is strictly negative for stable vertical  
 621 buoyancy gradients) must decrease with height above bottom, implying upwelling. This has  
 622 given rise to an increasingly accepted theory that waters generally downwell in the stratified  
 623 ocean interior, with this downwelling compensated by strong upwelling near topography –  
 624 resulting in net upwelling (Ferrari et al., 2016; McDougall & Ferrari, 2017; Drake et al.,  
 625 2020). Here, we are able to verify this theory within the context of our simulation, subject  
 626 to model constraints on resolution of the bottom boundary layer and uncertainties in the  
 627 parameterization of vertical diffusivity.

## 6.1 Water mass transformation framework

628 We first define the diapycnal velocity  $\tilde{\mathbf{e}}$ , that is the velocity in the cross-density surface  
 direction. By subtracting the motion of an isopycnal surface itself from the Eulerian velocity  
 of a water parcel, Ferrari et al. (2016) show that

$$\tilde{\mathbf{e}} = \frac{\nabla \cdot \mathbf{F}_b}{|N^2|} \mathbf{n}, \quad (3)$$

629 where  $\mathbf{F}_b$  is the buoyancy flux, and  $\mathbf{n}$  is the normal to the isopycnal surface defined as  
 630 pointing towards higher buoyancy. Note that this may not always be in the positive vertical  
 631 direction, and as such our definition of ‘upwelling’ refers to upwelling in buoyancy space,  
 632 which may be vertically downwards in the presence of unstable stratification. We approx-  
 633 imate the divergence of the buoyancy flux by  $\nabla \cdot \mathbf{F}_b \sim -\partial(\kappa N^2)/\partial z$ . This approximation  
 634 is often made due to the occurrence of significantly larger vertical buoyancy gradients than  
 635 horizontal ones in the ocean interior, and here we do not apply a horizontal diffusivity in  
 636 the model, so do not have explicit horizontal buoyancy fluxes. The vertical buoyancy flux  
 637  $F_b = -\kappa N^2$  is set to zero at topography to satisfy the insulating boundary condition.

In order to quantify upwelling over a density surface, we use the water mass transfor-  
 mation framework of Walin (1982); Ferrari et al. (2016). The diapycnal velocity integrated  
 over a neutral density surface  $A(\gamma)$  is denoted  $\mathcal{E}(\gamma)$ , where  $\gamma$  is neutral density, and is given  
 by:

$$\mathcal{E}(\gamma) = \int_{A(\gamma)} \tilde{\mathbf{e}} \cdot \mathbf{n} dA \simeq -\frac{\rho_0}{g} \frac{\partial}{\partial \gamma^*} \int_{\gamma > \gamma^*} \frac{\partial}{\partial z} (\kappa N^2) dV. \quad (4)$$

## 6.2 Simulated water mass transformation

638 A 30-day average of the diapycnal velocity  $\tilde{\mathbf{e}} \cdot \mathbf{n}$ , with  $\tilde{\mathbf{e}}$  as defined in equation (3), along  
 639  $-57^\circ$  N, is shown in figure 7a. Notice (red) upwelling close to topography in the bottom  
 640 50-100 m, with (blue) downwelling just above, consistent with the concept of upwelling in  
 641 a boundary layer, with downwelling in the stratified interior above. The upwelling occurs  
 642 due to complex topographic interaction processes in the bottom boundary layer creating  
 643 vertical gradients in stratification and diffusivity such that  $\frac{\partial F_b}{\partial z} < 0$ . In particular, areas  
 644 of unstable stratification near the boundary can reverse the direction of the normal vector  
 645 in equation (3), causing downwards diapycnal velocities that correspond to upwelling in  
 646 buoyancy space. The downwelling above this corresponds to stable stratification and a  
 647 strong decrease in diffusivity with height above bottom.  
 648

649 Above the downwelling, notice that there is largely weak upwelling in the interior; this  
 650 is because the vertical diffusivity is at its background value of  $5 \times 10^{-5} \text{ m}^2 \text{ s}^{-1}$  (unenhanced  
 651 by KPP), and variations in buoyancy flux are solely due to an increase in stratification  
 652 with height. The labelled neutral density contours demonstrate that, at this latitude, densi-  
 653 ties below  $28.16 \text{ kg m}^{-3}$  have intersections with topography, and therefore experience some  
 654 topographically enhanced upwelling. To formalise the importance of the topographic up-  
 655 welling and downwelling of each density class, we now calculate the domain-wide water mass  
 656 transformation, as defined by equation (4).

657 Figure 7b shows water mass transformation averaged over 30 days, using daily average  $\kappa$   
 658 and  $N^2$  fields. There are large contributions from both total upwelling (red) and downwelling  
 659 (blue), which are split by whether they occur within 250 m of topography (boundary, lighter  
 660 colours) or above this (interior, darker colours). It is clear that the majority of both up-  
 661 and downwelling occurs within 250 m of topography, as is expected from figure 7a. The  
 662 net transformation (the sum of upwelling and downwelling) is shown in green dashed, with  
 663 the white shading indicating one standard deviation of the 30-day time series. Despite  
 664 temporal variation (to be discussed later), it is clear that densities greater than  $28.19 \text{ kg}$   
 665  $\text{m}^{-3}$  (corresponding to SPDW and WSDW) upwell, whereas densities between  $28.19$  and  
 666  $28.15 \text{ kg m}^{-3}$  (corresponding to lighter LCDW) downwell. Lighter (interior) density classes  
 667 experience much less transformation, since they intersect less with topography and therefore  
 668 do not experience enhanced diffusivities.

669 The result that the densest waters upwell close to topography, with downwelling oc-  
 670 ccurring above, is, to our knowledge, the first verification of the upwelling/downwelling hy-  
 671 pothesis in a realistic, submesoscale- and internal wave-resolving numerical model with  
 672 online diffusivity parameterization. A recent study by Drake et al. (2022) resolved the  
 673 three-dimensional physical processes leading to diapycnal upwelling, downwelling, and re-  
 674 stratification near topography in a quasi-realistic simulation of a canyon in the Brazil Basin.  
 675 Using an idealised flow with an initially uniform stratification and a realistic topography,  
 676 they showed that an imposed observationally-based exponential diffusivity profile led to  
 677 near-boundary diapycnal upwelling by a three-dimensional eddying submesoscale flow. Our  
 678 work, although in a different region, therefore provides a step forwards in realism by re-  
 679 solving the larger-scale context of the flow (such as realistic large- and mesoscale currents,  
 680 non-uniform stratification, and spatially variable water masses), and by using an online  
 681 diffusivity parameterization to represent the processes that cause mixing. However, we  
 682 necessarily compromise on resolution of the bottom boundary layer, and our results must  
 683 therefore be taken with some caution.

684 By calculating the water mass transformation in the absence of the bottom grid-cell, it  
 685 becomes clear that much of the upwelling of the heaviest density classes is happening there,  
 686 where the insulating boundary condition effectively imposes upwelling. Indeed, several stud-  
 687 ies have calculated water mass transformations globally using climatologies and estimates of  
 688 mixing from various sources, by implicitly ensuring boundary upwelling in the bottom grid  
 689 cell (at any vertical resolution) due to the insulating boundary condition at topography (De  
 690 Lavergne et al., 2016; Ferrari et al., 2016; Mashayek, Salehipour, et al., 2017; Cimoli et al.,  
 691 2019).

692 The grey dashed line in figure 7b shows the net water mass transformation without  
 693 the bottom grid-cell. There remains a small amount of upwelling of the densest waters,  
 694 but downwelling largely dominates. This indicates that we are not sufficiently resolving  
 695 the bottom boundary layer to fully capture the upwelling/downwelling boundary with 25 m  
 696 vertical resolution. This is consistent with one-dimensional idealised boundary layer solu-  
 697 tions for sloping bathymetry with parameters similar to ours, which suggest that diapycnal  
 698 upwelling occurs in a layer of height  $O(50 \text{ m})$  (Holmes & McDougall, 2020). Similarly, the  
 699 quasi-realistic Brazil Basin simulations of Drake et al. (2022) with 6 m vertical resolution  
 700 demonstrated marginally resolved diapycnal upwelling in a bottom boundary layer of  $O(10)$   
 701 m.

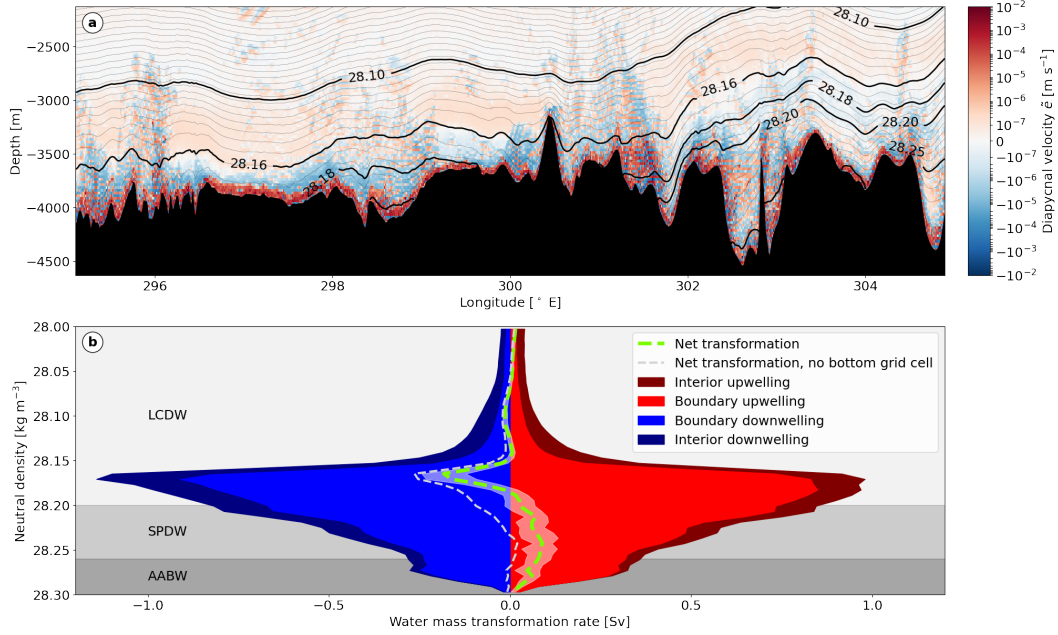


**Figure 7.** (a) 30-day average diapycnal velocity at  $-57^\circ$  N, computed as in equation (3), with neutral density contours. (b) Water mass transformation calculated using equation (4) from daily average density and vertical diffusivity fields, and averaged over 30 days. Interior and boundary contributions are defined by below/above 250 m above bottom. White shading around the net transformation (green dashed) indicates  $\pm 1$  standard deviation of the 30-day time series. The white dashed line shows net transformation when the bottom grid-cell is excluded from the calculation.

702 However, we do find that there is considerable upwelling outside of the bottom grid-cell,  
 703 as is clear from figure 7a, even though it is compensated by downwelling elsewhere. This  
 704 gives us confidence that some realistic processes inducing upwelling of the densest waters  
 705 are represented in this model. Furthermore, the daily averaged fields used to construct  
 706 figure 7b may filter out some of the higher-frequency processes generating upwelling near  
 707 the boundary, which we now investigate further.

### 708 6.3 Temporal variability

709 There is considerable temporal variability of the water mass transformation over the  
 710 30-day time period analysed, and there is therefore sensitivity to the frequency of output  
 711 fields used. In figure 8a, we show the net transformation rate over the final 10 days of the  
 712 simulation, calculated using hourly average fields, daily average fields, and 10-day average  
 713 fields. The corresponding results without the bottom grid-cell are shown as dashed lines of  
 714 the same colour.

715 In each case, upwelling occurs at densities in excess of  $28.19 \text{ kg m}^{-3}$ , with downwelling  
 716 above. This result is thus robust to the frequency of fields used. However, when using  
 717 hourly output (and therefore most accurately representing transformation rate over the 10-  
 718 day period), we find that there is significant upwelling of dense waters even when the bottom  
 719 grid-cell is not included. This suggests that higher-frequency dynamics, such as transient  
 720 boundary overturns, are key in upwelling dense waters in the bottom few hundred metres.

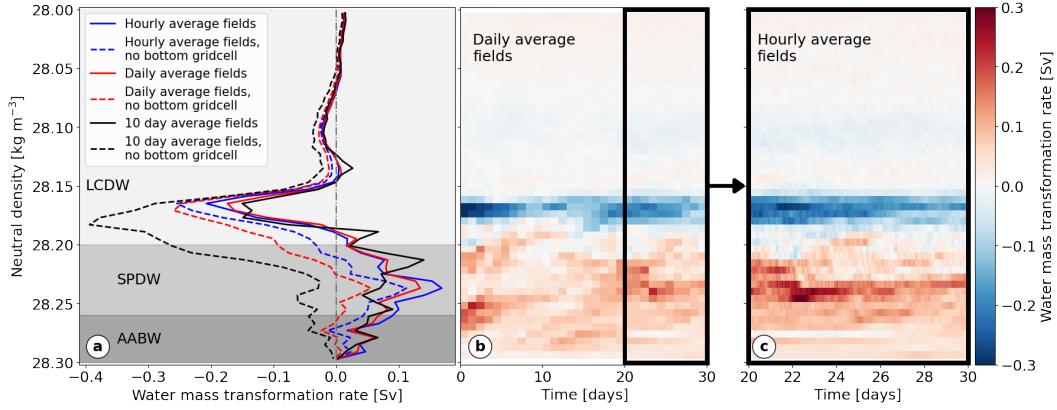


**Figure 8.** (a) Net water mass transformation rate (corresponding to green dashed line in figure 7a) as an average over 10 days, using fields saved at different frequencies. Dashed lines represent transformation rate with bottom grid-cell excluded. (b) Temporal variability of net water mass transformation rate over 30 days using daily average fields. (c) Temporal variability of net water mass transformation rate over 10 days (corresponding to final 10 days of (b)) from hourly output fields.

721 The temporal variability of transformation rate is shown using daily averages over 30  
 722 days in figure 8b, and using hourly averages over the final 10 days in figure 8c. Upwelling  
 723 below the  $28.19 \text{ kg m}^{-3}$  surface, and downwelling above it, are a feature at all times.  
 724 However, there is significant variability in the strength of the upwelling. In particular, a  
 725 high-upwelling event occurs at approximately 22 days, at densities between  $28.22$  and  $28.25$   
 726  $\text{kg m}^{-3}$ . It is very likely that this event corresponds to the high topographic mixing caused  
 727 by the AABW overflow of the West Scotia Ridge demonstrated in figure 6, which occurs  
 728 at this time. This suggests that the transformation of AABW into lighter water classes is  
 729 inherently linked to the dynamics and location of the interface across which it must mix.

730 **7 Sensitivity to model diffusivity**

731 The model-based diffusivity shown in figures 5 and 6, while rooted in sound physi-  
 732 cal concepts (i.e. shear-induced and convective mixing as parameterized through KPP), is  
 733 clearly insufficient. The diffusivity maps show mixing in the close vicinity of the seafloor  
 734 (the last few grid points of the model) and lack much information in the interior, where  
 735 diffusivity is simply set to a low background value. Observational estimates of mixing, how-  
 736 ever, show much more continuous variations in diffusivity as one approaches the seafloor  
 737 (e.g., see Waterhouse et al. (2014)), implying intermittent turbulence in the ocean interior.  
 738 The shortcoming of KPP is expected, as an important contribution of this work is per-  
 739 mitting processes (in the model) that contribute to abyssal mixing. Only further study of  
 740 such processes, which inevitably will require fully resolving them in even higher-resolution  
 741 process-study models, will enhance our physical understanding sufficiently to allow for new  
 742 parameterizations or for their integration into existing frameworks such as the KPP.

743 Since the nature of the simplistic KPP output has a bearing on the upwelling-downwelling  
 744 patterns and their corresponding net water mass transformation rates discussed in figures 7  
 745 and 8, here we also consider an alternate diffusivity parameterization. Figure 9 shows the  
 746 application of a recently developed machine learning (ML) based diffusivity parameteriza-  
 747 tion (Mashayek, Reynard, et al., 2022), which was shown to be rather skillful in the Drake  
 748 Passage region, to an hourly-average ‘snapshot’ from the simulation. The ML diffusivity

map shows a broader distribution of mixing above the seafloor (as opposed to the bottom-focused diffusivity from KPP) which simply reflects the fact that the ML-parameterization was trained on microstructure-based profiles exhibiting a gentler transition from interior to boundary mixing. The patterns emerging from the ML estimates are physically sensible, as they correspond to mixing by overturns along the seafloor (as discussed before and ‘felt’ by the KPP), but also above the seafloor due to breaking of lee waves and shearing of the sharp interfacial dynamics (neither captured by the KPP). Figure 1c confirms the good fit of the ML diffusivity estimate to observations when averaged with reference to height above bottom, and also shows that it gives a lower diffusivity at all heights above bottom than KPP.

The net transformation rates calculated from the KPP-based and ML-based diffusivities have significant differences (figures 9c,d), although the ML parameterisation still captures upwelling of the densest waters (AABW and SPDW). As discussed earlier, the rate at which the interior mixing increases towards the seafloor, and then decreases in the bottom boundary layer to yield a net zero flux at the solid boundary, controls the rate of boundary upwelling and the overlying downwelling. Thus, the smoother transition in mixing from interior to the seafloor in the ML-based estimate results in significantly weaker downwelling and upwelling rates.

Neither the KPP nor the ML representations of mixing are ideal. The former is based on physical principles, but lacks complexity due to our incomplete understanding of the processes that contribute to mixing. The latter is rooted in observations and physical understanding, but can certainly improve significantly as: (i) more observational data become available for training ML models, and (ii) more physical understanding is entrained in training the ML algorithms. Nevertheless, together, the two estimates (figures 9a,b) provide a bound on the uncertainty involved in estimates of mixing in even a realistic model of such unprecedented high resolution as ours. Thus, figure 9 helps us make two important points. First, it highlights the need for development of better mixing parameterizations in order to confidently determine the mixing of deep water masses and their net upwelling rates. Second, while at early stages, ML-based estimates, once connected with physical understanding, can prove a valuable tool for constraining deep-ocean mixing and meridional overturning.

The differences between the KPP and ML parameterizations do not impact the main messages of this paper, which are that (i) the dynamical interaction of water mass interfaces with topography is itself a source of instability and mixing in the deep ocean, (ii) the presence of these interfaces in the abyssal ocean can modify the nature of other topographic processes such as lee waves, and (iii) that small-scale, temporally variable, topographic interaction processes within a few hundred metres of the seafloor result in upwelling of AABW.

## 8 Discussion

We have used a high-resolution, realistic simulation to investigate the processes governing turbulent diapycnal mixing and water mass transformation of dense AABW as it flows through the Drake Passage. In addition to confirming the importance of known contributors to regional abyssal mixing (such as lee waves), we have also identified for the first time the dynamical role of highly stratified water mass interfaces in generating turbulence in the deep ocean.

Observational studies have previously reported the presence of highly stratified interfaces between deep water masses in several locations globally, including the Drake Passage (Sievers & Nowlin, 1984; Meredith et al., 2013; Reid et al., 1977). We have identified these stratified interfaces in further observations in the area as well as in our simulation, where the interfaces correspond to boundaries between deep CDW varieties (LCDW and SPDW) and the regional AABW (WSDW). The interfaces exhibit strong variability in time and space, and are often horizontally tilted by topography and mesoscale eddies.

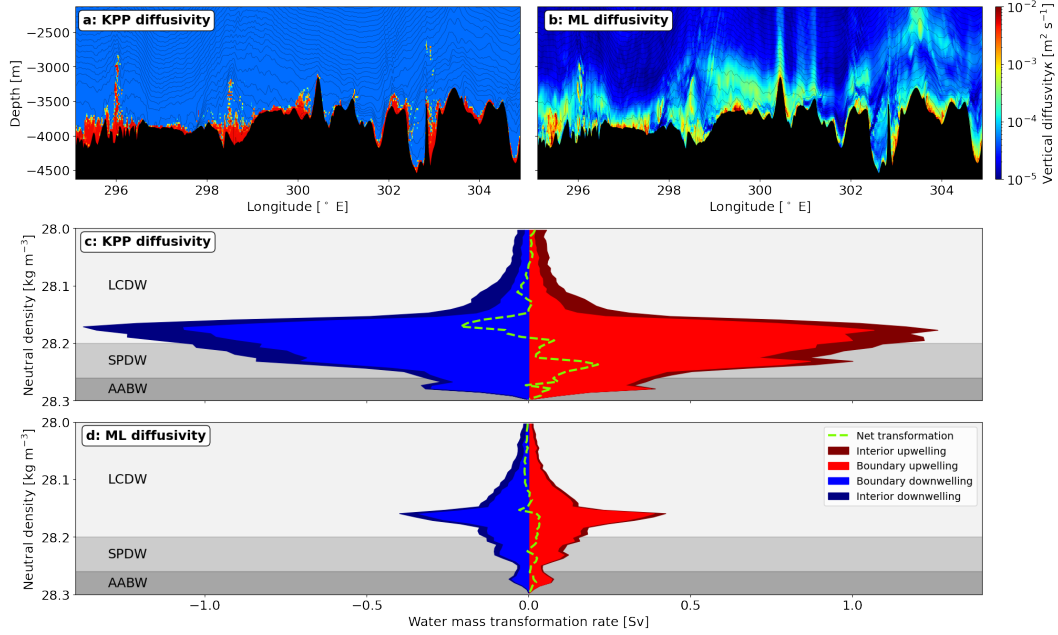


**Figure 9.** (a) Hourly average online KPP vertical diffusivity on day 94 (equivalent to figure 5b). (b) Offline diffusivity calculated from simulation fields using algorithm learnt from global observational turbulence data (Mashayek, Reynard, et al., 2022). (c) Water mass transformation calculated over the full domain from KPP diffusivity for an hourly average on day 94 (c.f. figure 7b). (d) As in (c), calculated using machine learning-based diffusivity shown in (b).

799 We conclude, based on our simulation, that these interfaces may play an important role  
 800 in the upwelling of AABW by boosting topographic mixing processes in the deep ocean.  
 801 We have identified several dynamical impacts of the interfaces: (i) creation of vertical shear  
 802 in the deep ocean by geostrophic adjustment of tilted interfaces; (ii) interaction of strong  
 803 horizontal buoyancy gradients with topography to induce convective overturning; and (iii)  
 804 impact on the generation, propagation and breaking of lee waves.

805 The evidence presented here for the existence of such water mass interfaces at depth  
 806 and their impact on abyssal dynamics raises important questions that will require further  
 807 study. We conjectured that the maintenance of the interfaces' high stratification may be  
 808 linked to frontogenetic processes in the deep ocean, but this should be examined in detail.  
 809 Further, the occurrence and relevance of these interfaces over the Southern Ocean and  
 810 globally should be investigated. Unfortunately, even state-of-the-art resolution global ocean  
 811 models, such as the 1/48° LLC4320 global simulation (Rocha et al., 2016; Su et al., 2018) do  
 812 not have sufficient vertical resolution at depth to adequately capture water mass interfaces.  
 813 We found no evidence of stratified interfaces in the LLC4320 model in the Drake Passage,  
 814 likely owing to the resolution at 4000 m depth being  $\sim 200$  m. If, as suggested here, water  
 815 mass interfaces impact topographic turbulence and lee wave generation and breaking, this  
 816 effect would be extremely challenging to account for in mixing parameterizations embedded  
 817 in coarse models.

818 Using an online parameterization of diffusivity, we were able to link topographic mixing  
 819 processes to quantification of water mass transformation in the Drake Passage. Waters  
 820 denser than 28.19, corresponding to SPDW and WSDW, were found to experience net  
 821 upwelling, whereas the LCDW above experiences net downwelling. We proposed that an

822 episode of strong AABW upwelling in the simulation was elicited by an overflow of dense  
 823 AABW over a large topographic ridge system, linking the dynamics of the interface (both  
 824 in terms of its location and effect on mixing) to cross-interface upwelling.

825 Our work constitutes a first realistic demonstration of how resolved submesoscale and  
 826 internal wave-driven mixing processes induce boundary upwelling of deep waters, as pre-  
 827 dicted by the recently put forward upwelling/downwelling paradigm (De Lavergne et al.,  
 828 2016; Ferrari et al., 2016; McDougall & Ferrari, 2017). However, still higher vertical res-  
 829 olution on the order of metres is needed to satisfactorily resolve upwelling in the bottom  
 830 boundary layer (Drake et al., 2022). We also demonstrated the need for hourly temporal res-  
 831 olution to capture the water mass transformation correctly, especially outside of the bottom  
 832 grid-cell. This implies that that the processes driving diapycnal upwelling are highly tem-  
 833 porally variable. Given the demonstrated importance of realistic topography, stratification  
 834 and flow, and of metre-scale boundary layer dynamics in quantifying AABW transforma-  
 835 tion, unprecedented model resolution would be required to fully capture the wide range of  
 836 scales of this problem.

837 Through comparison of our online KPP diffusivity parameterization and resulting water  
 838 mass transformation with results based on a recent machine learning estimate of diffusivity,  
 839 we showed that considerable uncertainties remain in the vertical diffusivity representation of  
 840 abyssal processes. This brings about a limited ability of even high resolution regional models  
 841 to adequately constrain the transformation rate of abyssal waters. Knowledge of this trans-  
 842 formation rate is essential to our understanding of the ocean’s overturning circulation and  
 843 oceanic transport and storage of climatically important tracers. Resolving these outstand-  
 844 ing questions in the future will require a multifaceted approach of higher-resolution model  
 845 process studies, innovative applications of machine learning, and more extensive abyssal  
 846 observations in different turbulent regimes.

## 847 **Appendix A Drake Passage Model Setup**

848 The simulation is performed at  $0.01^\circ$  horizontal resolution using the MITgcm (Marshall  
 849 et al., 1997) in hydrostatic configuration. There are 225 vertical levels, with resolution  $dz$   
 850 varying smoothly from  $dz = 10$  m at the surface to  $dz = 25$  m at 600 m depth,  $dz = 25$   
 851 m between 600 and 4,555 m depth, and varying smoothly from  $dz = 25$  m to 62 m at the  
 852 maximum depth of 5,660 m. Partial cells are used at topography with a minimum height of  
 853 10 m. The timestep is 24 s.

854 The simulation is forced at the open boundaries by the OCCA state estimate (Forget,  
 855 2010) as described in the main text. The nonlinear free surface is forced by near surface  
 856 air temperature, wind speed, precipitation, humidity, long and short wave radiation from  
 857 the ECMWF ERA-Interim reanalysis product (Simmons et al., 2006). The model does not  
 858 include tides. The topography is interpolated from the Smith and Sandwell (1997) v15.1  
 859 1 min bathymetric product, and contains some areas of multibeam topography alongside  
 860 satellite altimetry derived estimates of topography.

861 The bottom boundary condition is no-slip, which is implemented in the MITgcm  
 862 through an extra drag term in the bottom grid cell. In addition, we use a quadratic drag  
 863 with a coefficient of  $2.5 \times 10^{-3}$  to represent unresolved small scale topography; see MITgcm  
 864 documentation (<https://mitgcm.readthedocs.io>) and Legg et al. (2006) for details.

865 Horizontal viscosity is implemented with the biharmonic Leith scheme with a coefficient  
 866 of 2 (Fox-Kemper & Menemenlis, 2008; Leith, 1996). Background vertical viscosity and  
 867 diffusivity of temperature and salinity are set at  $5 \times 10^{-5} \text{ m}^2 \text{ s}^{-1}$ . The KPP parameterization  
 868 (Large et al., 1994) enhances vertical diffusivity (and viscosity) in the interior according to  
 869 criteria for shear and convective instability. The critical Richardson number for onset of  
 870 shear instability is  $1/3$ .

## Open Research

All software and processed data required to enable the reader to reproduce our results are published via Zenodo at [doi.org/10.5281/zenodo.7410908](https://doi.org/10.5281/zenodo.7410908) (Baker et al., 2022). The MIT-gcm (Marshall et al., 1997) is documented at <https://mitgcm.readthedocs.io> and available at [doi.org/10.5281/zenodo.1409237](https://doi.org/10.5281/zenodo.1409237) (Campin et al., 2019).

Observational CTD data along the SR1b section, collected by the ACCLAIM project and used in figures 1e and 2, and CTD and ADCP data collected by the DIMES project used in figure 4 are available from [bodc.ac.uk/data](https://bodc.ac.uk/data).

## Conflict of Interest Statement

The authors have no conflicts of interest to declare.

## Acknowledgments

L.B. was supported by the Centre for Doctoral Training in Mathematics of Planet Earth, UK EPSRC funded (Grant EP/L016613/1), and A.M. acknowledges funding from the NERC IRF fellowship grant NE/P018319/1. Computational resources provided by the Imperial College London Research Computing Service are gratefully acknowledged (<https://doi.org/10.14469/hpc/2232>).

## References

- Alford, M. H., Girton, J. B., Voet, G., Carter, G. S., Mickett, J. B., & Klymak, J. M. (2013). Turbulent mixing and hydraulic control of abyssal water in the Samoan Passage. *Geophys. Res. Lett.*, *40*(17), 4668–4674. doi: 10.1002/grl.50684
- Armi, L., & Mayr, G. J. (2015). Virtual and real topography for flows across mountain ranges. *J. Appl. Meteorol. Climatol.*, *54*(4), 723–731. doi: 10.1175/JAMC-D-14-0231.1
- Baines, P. G. (1995). *Topographic effects in stratified flows*. Cambridge: Cambridge University Press.
- Baker, L. E., & Mashayek, A. (2021). Surface reflection of bottom generated oceanic lee waves. *J. Fluid Mech.*, *924*(A17), 1–42. doi: 10.1017/jfm.2021.627
- Baker, L. E., & Mashayek, A. (2022). The Impact of Representations of Realistic Topography on Parameterized Oceanic Lee Wave Energy Flux. *J. Geophys. Res. Ocean.*, 1–34. doi: 10.1029/2022JC018995
- Baker, L. E., Mashayek, A., & Naveira-Garabato, A. C. (2022). *Enhanced upwelling of Antarctic Bottom Water by topographic interaction of water mass interfaces [Software and Dataset]*. Zenodo. doi: 10.5281/zenodo.7410908
- Callies, J. (2018). Restratification of abyssal mixing layers by submesoscale baroclinic eddies. *J. Phys. Oceanogr.*, *48*(9), 1995–2010. doi: 10.1175/JPO-D-18-0082.1
- Campin, J.-M., Heimbach, P., Losch, M., Forget, G., Edhill, A., Adcroft, A., ... Dussin, R. (2019). *MITgcm/MITgcm: checkpoint67g [Software]*. Zenodo. doi: 10.5281/zenodo.1409237
- Caulfield, C. (2021). Layering, Instabilities, and Mixing in Turbulent Stratified Flows. *Annu. Rev. Fluid Mech.*, *53*(1). doi: 10.1146/annurev-fluid-042320-100458
- Cimoli, L., Caulfield, C. c. P., Johnson, H. L., Marshall, D. P., Mashayek, A., Naveira Garabato, A. C., & Vic, C. (2019). Sensitivity of Deep Ocean Mixing to Local Internal Tide Breaking and Mixing Efficiency. *Geophys. Res. Lett.*, *46*(24), 14622–14633. doi: 10.1029/2019GL085056
- Cusack, J. M., Naveira Garabato, A. C., Smeed, D. A., & Girton, J. B. (2017). Observation of a Large Lee Wave in the Drake Passage. *J. Phys. Oceanogr.*, *47*(4), 793–810. doi: 10.1175/JPO-D-16-0153.1

- 918 De Lavergne, C., Madec, G., Le Sommer, J., Nurser, A. J., & Naveira Garabato, A. C.  
919 (2016). On the consumption of Antarctic Bottom Water in the abyssal ocean. *J.*  
920 *Phys. Oceanogr.*, *46*(2), 635–661. doi: 10.1175/JPO-D-14-0201.1
- 921 Drake, H. F., Ferrari, R., & Callies, J. (2020). Abyssal circulation driven by near-boundary  
922 mixing: Water mass transformations and interior stratification. *J. Phys. Oceanogr.*,  
923 *50*(8), 2203–2226. doi: 10.1175/JPO-D-19-0313.1
- 924 Drake, H. F., Ruan, X., Callies, J., Ogden, K., Thurnherr, A. M., & Ferrari, R. (2022).  
925 Dynamics of eddying abyssal mixing layers over sloping rough topography. *J. Phys.*  
926 *Oceanogr.*. doi: 10.1175/jpo-d-22-0009.1
- 927 Durran, D. R. (1986). Another Look at Downslope Windstorms. Part I: The Development of  
928 Analogs to Supercritical Flow in an Infinitely Deep, Continuously Stratified Fluid. *J.*  
929 *Atmos. Sci.*, *43*(21), 2527–2543. doi: 10.1175/1520-0469(1986)043<2527:ALADWP>2  
930 .0.CO;2
- 931 Emile-Geay, J., & Madec, G. (2009). Geothermal heating, diapycnal mixing and the abyssal  
932 circulation. *Ocean Sci.*, *5*(2), 203–217. doi: 10.5194/os-5-203-2009
- 933 Ferrari, R., Mashayek, A., McDougall, T. J., Nikurashin, M., & Campin, J. M. (2016).  
934 Turning ocean mixing upside down. *J. Phys. Oceanogr.*, *46*(7), 2239–2261. doi: 10  
935 .1175/JPO-D-15-0244.1
- 936 Forget, G. (2010, jun). Mapping ocean observations in a dynamical framework: A 2004-06  
937 ocean atlas. *J. Phys. Oceanogr.*, *40*(6), 1201–1221. doi: 10.1175/2009JPO4043.1
- 938 Fox-Kemper, B., & Menemenlis, D. (2008). Can large eddy simulation techniques improve  
939 mesoscale rich ocean models? *Geophys. Monogr. Ser.*, *177*, 319–337. doi: 10.1029/  
940 177GM19
- 941 Garrett, C., MacCready, P., & Rhines, P. (1993). Boundary mixing and arrested Ekman  
942 layers: rotating stratified flow near a sloping boundary. *Annu. Rev. Fluid Mech.*. doi:  
943 10.1146/annurev.fluid.25.1.291
- 944 Gregg, M., D’Asaro, E., Riley, J., & Kunze, E. (2018). Mixing Efficiency in the Ocean.  
945 *Ann. Rev. Mar. Sci.*, *10*(1), 443–473. doi: 10.1146/annurev-marine-121916-063643
- 946 Gutierrez-Villanueva, M. O., Chereskin, T. K., Sprintall, J., & Goff, J. A. (2022). Turbulent  
947 Mixing and Lee-Wave Radiation in Drake Passage: Sensitivity to Topography. *J.*  
948 *Geophys. Res. Ocean.*, *127*(5), 1–25. doi: 10.1029/2021jc018103
- 949 Holmes, R. M., & McDougall, T. J. (2020). Diapycnal transport near a sloping bottom  
950 boundary. *J. Phys. Oceanogr.*, *50*(11), 3253–3266. doi: 10.1175/JPO-D-20-0066.1
- 951 Hoskins, B. J. (1982). The mathematical theory of frontogenesis. *Annu. Rev. fluid Mech.*  
952 *Vol. 14*, 131–151. doi: 10.1146/annurev.fl.14.010182.001023
- 953 Howard, L. (1961). Note on a paper of John W. Miles. *J. Fluid Mech.*, *10*(4), 509–512. doi:  
954 10.1017/S0022112061000317
- 955 Jackett, D. R., & McDougall, T. J. (1997). A neutral density variable for the world’s  
956 oceans. *J. Phys. Oceanogr.*, *27*(2), 237–263. doi: 10.1175/1520-0485(1997)027<0237:  
957 ANDVFT>2.0.CO;2
- 958 Jagannathan, A., Winters, K. B., & Armi, L. (2020). The effect of a strong density  
959 step on blocked stratified flow over topography. *J. Fluid Mech.*, *889*. doi: 10.1017/  
960 jfm.2020.87
- 961 Johnson, G. C. (2008). Quantifying Antarctic Bottom Water and North Atlantic Deep  
962 Water volumes. *J. Geophys. Res. Ocean.*, *113*(5), 1–13. doi: 10.1029/2007JC004477
- 963 Klemp, J. B., & Lilly, D. K. (1975). The dynamics of wave-induced downslope winds. *J.*  
964 *Atmos. Sci.*, *32*. doi: 10.1175/1520-0469(1975)032<0320:TADOWID>2.0.CO;2
- 965 Klymak, J. M. (2018). Nonpropagating form drag and turbulence due to stratified flow  
966 over large-scale Abyssal Hill Topography. *J. Phys. Oceanogr.*, *48*(10), 2383–2395. doi:  
967 10.1175/JPO-D-17-0225.1
- 968 Klymak, J. M., Balwada, D., Garabato, A. N., & Abernathey, R. (2021). Parameterizing  
969 Nonpropagating Form Drag over Rough Bathymetry. *J. Phys. Oceanogr.*, *51*(5), 1489–  
970 1501. doi: 10.1175/jpo-d-20-0112.1
- 971 Kunze, E., & Lien, R.-C. (2019). Energy Sinks for Lee Waves in Shear Flow. *J. Phys.*  
972 *Oceanogr.*, 2851–2865. doi: 10.1175/jpo-d-19-0052.1

- 973 Large, W. G., McWilliams, J. C., & Doney, S. C. (1994). Oceanic vertical mixing: A review  
974 and a model with a nonlocal boundary layer parameterization. *Rev. Geophys.*, *32*(4),  
975 363–403. doi: 10.1029/94RG01872
- 976 Ledwell, J. R., Montgomery, E. T., Polzin, K. L., St. Laurent, L. C., Schmitt, R. W., &  
977 Toole, J. M. (2000). Evidence for enhanced mixing over rough topography in the  
978 abyssal ocean. *Nature*, *403*, 179–182. doi: 10.1038/35003164
- 979 Legg, S. (2021). Mixing by Oceanic Lee Waves. *Annu. Rev. Fluid Mech.*, *53*, 173–201. doi:  
980 10.1146/annurev-fluid-051220-043904
- 981 Legg, S., Hallberg, R. W., & Girton, J. B. (2006). Comparison of entrainment in overflows  
982 simulated by z-coordinate, isopycnal and non-hydrostatic models. *Ocean Model.*, *11*(1-  
983 2), 69–97. doi: 10.1016/j.ocemod.2004.11.006
- 984 Legg, S., & Klymak, J. (2008). Internal Hydraulic Jumps and Overturning Generated  
985 by Tidal Flow over a Tall Steep Ridge. *J. Phys. Oceanogr.*, *38*, 1949–1964. doi:  
986 10.1175/2008JPO3777.1
- 987 Leith, C. E. (1996). Stochastic models of chaotic systems. *Phys. D Nonlinear Phenom.*,  
988 *98*(2-4), 481–491. doi: 10.1016/0167-2789(96)00107-8
- 989 Liu, M., & Tanhua, T. (2021). Water masses in the Atlantic Ocean: Characteristics and  
990 distributions. *Ocean Sci.*, *17*(2), 463–486. doi: 10.5194/os-17-463-2021
- 991 Lumpkin, R., & Speer, K. (2007). Global ocean meridional overturning. *J. Phys. Oceanogr.*,  
992 *37*(10), 2550–2562. doi: 10.1175/JPO3130.1
- 993 MacCready, P., & Rhines, P. B. (1991). Buoyant inhibition of ekman transport on a slope  
994 and its effect on stratified spin-up. *J. Fluid Mech.*, *223*, 631–661. doi: 10.1017/  
995 S0022112091001581
- 996 Mackay, N., Ledwell, J. R., Messias, M. J., Naveira Garabato, A. C., Brearley, J. A., Meijers,  
997 A. J., ... Watson, A. J. (2018, apr). Diapycnal Mixing in the Southern Ocean  
998 Diagnosed Using the DIMES Tracer and Realistic Velocity Fields. *J. Geophys. Res.*  
999 *Ocean.*, *123*(4), 2615–2634. doi: 10.1002/2017JC013536
- 1000 MacKinnon, J., Laurent, L. S., & Garabato, A. C. N. (2013). Diapycnal Mixing Processes  
1001 in the Ocean Interior. In *Ocean circ. clim. a 21st century perspect.* (Vol. 103, pp.  
1002 159–183). Retrieved from [http://www.sciencedirect.com/science/article/pii/  
1003 B9780123918512000076](http://www.sciencedirect.com/science/article/pii/B9780123918512000076) doi: <https://doi.org/10.1016/B978-0-12-391851-2.00007-6>
- 1004 MacKinnon, J. A., Zhao, Z., Whalen, C. B., Griffies, S. M., Sun, O. M., Barna, A., ...  
1005 Norton, N. J. (2017). Climate Process Team on Internal Wave–Driven Ocean Mixing.  
1006 *Bull. Am. Meteorol. Soc.*, *98*(11), 2429–2454. doi: 10.1175/bams-d-16-0030.1
- 1007 Marshall, J., Adcroft, A., Hill, C., Perelman, L., & Heisey, C. (1997). A finite-volume,  
1008 incompressible navier stokes model for, studies of the ocean on parallel computers. *J.*  
1009 *Geophys. Res. C Ocean.*, *102*(C3), 5753–5766. doi: 10.1029/96JC02775
- 1010 Marshall, J., & Speer, K. (2012). Closure of the meridional overturning circulation through  
1011 Southern Ocean upwelling. *Nat. Geosci.*, *5*(3), 171–180. doi: 10.1038/ngeo1391
- 1012 Mashayek, A., Baker, L. E., Cael, B. B., & Caulfield, C. P. (2022). A Marginal Stability  
1013 Paradigm for Shear-Induced Diapycnal Turbulent Mixing in the Ocean. *Geophys. Res.*  
1014 *Lett.*, *49*(2), 1–11. doi: 10.1029/2021GL095715
- 1015 Mashayek, A., Caulfield, C. P., & Alford, M. H. (2021). Goldilocks mixing in oceanic shear-  
1016 induced turbulent overturns. *J. Fluid Mech.*, *928*, 1–32. doi: 10.1017/jfm.2021.740
- 1017 Mashayek, A., Ferrari, R., Merrifield, S., Ledwell, J. R., St Laurent, L., & Garabato, A. N.  
1018 (2017). Topographic enhancement of vertical turbulent mixing in the Southern Ocean.  
1019 *Nat. Commun.*, *8*, 1–12. doi: 10.1038/ncomms14197
- 1020 Mashayek, A., Ferrari, R., Vettoretti, G., & Peltier, W. R. (2013). The role of the geothermal  
1021 heat flux in driving the abyssal ocean circulation. *Geophys. Res. Lett.*, *40*(12), 3144–  
1022 3149. doi: 10.1002/grl.50640
- 1023 Mashayek, A., Reynard, N., Zhai, F., Srinivasan, K., Jelley, A., Naveira Garabato, A., &  
1024 Caulfield, C. P. (2022). Deep Ocean Learning of Small Scale Turbulence. *Geophys.*  
1025 *Res. Lett.*, *49*(15), 1–9. doi: 10.1029/2022GL098039
- 1026 Mashayek, A., Salehipour, H., Bouffard, D., Caulfield, C. P., Ferrari, R., Nikurashin, M., ...  
1027 Caulfield, C. P. (2017). Efficiency of turbulent mixing in the abyssal ocean circulation.

- 1028 *Geophys. Res. Lett.*, *44*(12), 6296–6306. doi: 10.1002/2016gl072452
- 1029 McDougall, T. J., & Ferrari, R. (2017). Abyssal upwelling and downwelling driven by near-  
1030 boundary mixing. *J. Phys. Oceanogr.*, *47*(2), 261–283. doi: 10.1175/JPO-D-16-0082.1
- 1031 McWilliams, J. C. (2021). Oceanic Frontogenesis. *Ann. Rev. Mar. Sci.*, *13*, 227–253. doi:  
1032 10.1146/annurev-marine-032320-120725
- 1033 Meredith, M. P., Brown, P. J., Naveira Garabato, A. C., Jullion, L., Venables, H. J.,  
1034 & Messias, M. J. (2013). Dense bottom layers in the Scotia Sea, Southern Ocean:  
1035 Creation, lifespan, and destruction. *Geophys. Res. Lett.*, *40*(5), 933–936. doi: 10.1002/  
1036 grl.50260
- 1037 Meredith, M. P., & Naveira Garabato, A. C. (2021). *Ocean Mixing*. Elsevier. doi: 10.1016/  
1038 C2019-0-03674-6
- 1039 Merrifield, S. T., Laurent, L. S., Owens, B., Thurnherr, A. M., & Toole, J. M. (2016).  
1040 Enhanced diapycnal diffusivity in intrusive regions of the Drake passage. *J. Phys.*  
1041 *Oceanogr.*, *46*(4), 1309–1321. doi: 10.1175/JPO-D-15-0068.1
- 1042 Miles, J. W. (1961). On the stability of heterogeneous shear flows. *J. Fluid Mech.*, *10*(4),  
1043 496–508. doi: 10.1017/S0022112061000305
- 1044 Moum, J. N. (2021). Variations in Ocean Mixing from Seconds to Years. *Ann. Rev. Mar.*  
1045 *Sci.*, *13*, 201–226. doi: 10.1146/annurev-marine-031920-122846
- 1046 Munk, W., & Wunsch, C. (1998). Abyssal recipes II Energetics of tidal and wind mixing.  
1047 *Deep. Res.*, *I*(45), 1977–2010. doi: 10.1016/S0967-0637(98)00070-3
- 1048 Naveira Garabato, A., Polzin, K., King, B., Heywood, K., & Visbeck, M. (2004). Widespread  
1049 Intense Turbulent Mixing in the Southern Ocean. *Science (80-. )*, *303*(January), 210–  
1050 213. doi: 10.1126/science.1090929
- 1051 Naveira Garabato, A. C., Frajka-Williams, E. E., Spingys, C. P., Legg, S., Polzin, K. L.,  
1052 Forryan, A., ... Meredith, M. P. (2019). Rapid mixing and exchange of deep-ocean  
1053 waters in an abyssal boundary current. *Proc. Natl. Acad. Sci. U. S. A.*, *116*(27),  
1054 13233–13238. doi: 10.1073/pnas.1904087116
- 1055 Naveira Garabato, A. C., Heywood, K. J., & Stevens, D. P. (2002). Modification and  
1056 pathways of Southern Ocean Deep Waters in the Scotia Sea. *Deep. Res. I*, *49*, 681–  
1057 705. doi: 10.1016/S0967-0637(01)00071-1
- 1058 Naveira Garabato, A. C., McDonagh, E. L., Stevens, D. P., Heywood, K. J., & Sanders,  
1059 R. J. (2002). On the export of Antarctic Bottom Water from the Weddell Sea. *Deep.*  
1060 *Res. Part II Top. Stud. Oceanogr.*, *49*(21), 4715–4742. doi: 10.1016/S0967-0645(02)  
1061 00156-X
- 1062 Naveira Garabato, A. C., Williams, A. P., & Bacon, S. (2014). The three-dimensional  
1063 overturning circulation of the Southern Ocean during the WOCE era. *Prog. Oceanogr.*,  
1064 *120*, 41–78. doi: 10.1016/j.pocean.2013.07.018
- 1065 Nikurashin, M., & Ferrari, R. (2010). Radiation and Dissipation of Internal Waves Generated  
1066 by Geostrophic Motions Impinging on Small-Scale Topography: Application to the  
1067 Southern Ocean. *J. Phys. Oceanogr.*, *40*(9), 2025–2042. doi: 10.1175/2010jpo4315.1
- 1068 Nikurashin, M., & Ferrari, R. (2011). Global energy conversion rate from geostrophic  
1069 flows into internal lee waves in the deep ocean. *Geophys. Res. Lett.*, *38*(8), 1–6. doi:  
1070 10.1029/2011GL046576
- 1071 Osborn, T. R. (1980). *Estimates of the Local Rate of Vertical Diffusion from Dissipation*  
1072 *Measurements* (Vol. 10) (No. 1). doi: 10.1175/1520-0485(1980)010<0083:eotlro>2.0.co;  
1073 2
- 1074 Peltier, W., & Clark, T. (1979). The Evolution and Stability of Finite-Amplitude Mountain  
1075 Waves. Part II: Surface Wave Drag and Severe Downslope Windstorms. *J. Atmos.*  
1076 *Sci.*, *36*(9), 1498–1529. doi: 10.1175/1520-0469(1980)037<2119:COEASO>2.0.CO;2
- 1077 Polzin, K. L., & McDougall, T. J. (2022). Mixing at the ocean’s bottom boundary. In  
1078 M. P. Meredith & A. C. Naveira Garabato (Eds.), *Ocean mix.* (pp. 145–180). Elsevier.  
1079 doi: 10.1016/b978-0-12-821512-8.00014-1
- 1080 Polzin, K. L., Toole, J. M., Ledwell, J. R., & Schmitt, R. W. (1997). Spatial variability  
1081 of turbulent mixing in the abyssal ocean. *Science (80-. )*, *276*(5309), 93–96. doi:  
1082 10.1126/science.276.5309.93

- 1083 Purkey, S. G., Smethie, W. M., Gebbie, G., Gordon, A. L., Sonnerup, R. E., Warner,  
1084 M. J., & Bullister, J. L. (2018). A synoptic view of the ventilation and circulation of  
1085 antarctic bottom water from chlorofluorocarbons and natural tracers. *Ann. Rev. Mar.*  
1086 *Sci.*, *10*(September), 503–527. doi: 10.1146/annurev-marine-121916-063414
- 1087 Rae, J. W., Burke, A., Robinson, L. F., Adkins, J. F., Chen, T., Cole, C., ... Taylor,  
1088 B. J. (2018). CO<sub>2</sub> storage and release in the deep Southern Ocean on millennial to  
1089 centennial timescales. *Nature*, *562*(7728), 569–573. doi: 10.1038/s41586-018-0614-0
- 1090 Reid, J., Nowlin, W., & Patzert, W. (1977). On the Characteristics and Circulation of  
1091 the Southwestern Atlantic Ocean. *J. Phys. Oceanogr.*, *7*, 62–91. doi: 10.1175/1520-  
1092 -0485(1977)007<0062:OTCACO>2.0.CO;2
- 1093 Rocha, C. B., Chereskin, T. K., Gille, S. T., & Menemenlis, D. (2016). Mesoscale to  
1094 submesoscale wavenumber spectra in Drake Passage. *J. Phys. Oceanogr.*, *46*(2), 601–  
1095 620. doi: 10.1175/JPO-D-15-0087.1
- 1096 Ruan, X., Thompson, A. F., & Taylor, J. R. (2019). The evolution and arrest of a turbulent  
1097 stratified oceanic bottom boundary layer over a slope: Downslope regime. *J. Phys.*  
1098 *Oceanogr.*, *49*(2), 469–487. doi: 10.1175/JPO-D-18-0079.1
- 1099 Ruan, X., Thompson, A. F., & Taylor, J. R. (2021). The evolution and arrest of a tur-  
1100 bulent stratified oceanic bottom boundary layer over a slope: Upslope regime and pv  
1101 dynamics. *J. Phys. Oceanogr.*, *51*(4), 1077–1089. doi: 10.1175/JPO-D-20-0168.1
- 1102 Sarkar, S., & Scotti, A. (2017). From Topographic Internal Gravity Waves to Turbulence.  
1103 *Annu. Rev. Fluid Mech.*, *49*(1), 195–220. doi: 10.1146/annurev-fluid-010816-060013
- 1104 Scott, R. B., Goff, J. A., Naveira Garabato, A. C., & Nurser, A. J. G. (2011). Global rate  
1105 and spectral characteristics of internal gravity wave generation by geostrophic flow  
1106 over topography. *J. Geophys. Res.*, *116*(C09029), 1–14. doi: 10.1029/2011JC007005
- 1107 Sheen, K. L., Brearley, J. A., Naveira Garabato, A. C., Smeed, D. A., Waterman, S., Ledwell,  
1108 J. R., ... Watson, A. J. (2013). Rates and mechanisms of turbulent dissipation and  
1109 mixing in the Southern Ocean: Results from the Diapycnal and Isopycnal Mixing  
1110 Experiment in the Southern Ocean (DIMES). *J. Geophys. Res. Ocean.*, *118*(6), 2774–  
1111 2792. doi: 10.1002/jgrc.20217
- 1112 Sheridan, P. F., & Vosper, S. B. (2006). A flow regime diagram for forecasting lee  
1113 waves, rotors and downslope winds. *Meteorol. Appl.*, *13*(2), 179–195. doi: 10.1017/  
1114 S1350482706002088
- 1115 Siegelman, L., Klein, P., Rivière, P., Thompson, A. F., Torres, H. S., Flexas, M., & Men-  
1116 emenlis, D. (2020). Enhanced upward heat transport at deep submesoscale ocean  
1117 fronts. *Nat. Geosci.*, *13*(1), 50–55. doi: 10.1038/s41561-019-0489-1
- 1118 Sievers, H. A., & Nowlin, W. D. (1984). The stratification and water masses at Drake  
1119 Passage. *J. Geophys. Res.*, *89*(C6), 10489. doi: 10.1029/jc089ic06p10489
- 1120 Simmons, A., Uppala, S., Dee, D., & Kobayashi, S. (2006). ERA-Interim: New ECMWF  
1121 reanalysis products from 1989 onwards. *ECMWF Newsl.*, *110*, 25–35. doi: 10.21957/  
1122 pocnex23c6
- 1123 Skinner, L., Fallon, S., Waelbroeck, C., Michel, E., & Barker, S. (2010). Ventilation of the  
1124 Deep Southern Ocean and Deglacial CO<sub>2</sub> Rise. *Science (80-. )*, *328*, 1147–1152. doi:  
1125 10.1126/science.1183627
- 1126 Smith, W. H., & Sandwell, D. T. (1997). Global sea floor topography from satellite altimetry  
1127 and ship depth soundings. *Science (80-. )*, *277*(5334), 1956–1962. doi: 10.1126/  
1128 science.277.5334.1956
- 1129 Smyth, W. D. (2020). Marginal instability and the efficiency of ocean mixing. *J. Phys.*  
1130 *Oceanogr.*, *50*(8), 2141–2150. doi: 10.1175/JPO-D-20-0083.1
- 1131 Solodoch, A., Stewart, A. L., Hogg, A. M. C., Morrison, A. K., Kiss, A. E., Thompson,  
1132 A. F., ... Cimoli, L. (2022). How Does Antarctic Bottom Water Cross the Southern  
1133 Ocean? *Geophys. Res. Lett.*, *49*(7), 1–11. doi: 10.1029/2021GL097211
- 1134 Spingys, C. P., Naveira Garabato, A. C., Legg, S., Polzin, K. L., Abrahamsen, E. P.,  
1135 Buckingham, C. E., ... Frajka-Williams, E. E. (2021, jan). Mixing and Transformation  
1136 in a Deep Western Boundary Current: A Case Study. *J. Phys. Oceanogr.*, *51*(4),  
1137 1205–1222. doi: 10.1175/jpo-d-20-0132.1

- 1138 Srinivasan, K., McWilliams, J. C., Molemaker, M. J., & Barkan, R. (2019). Submesoscale  
1139 Vortical Wakes in the Lee of Topography. *J. Phys. Oceanogr.*, *49*(7), 1949–1971. doi:  
1140 10.1175/jpo-d-18-0042.1
- 1141 St. Laurent, L., Naveira Garabato, A. C., Ledwell, J. R., Thurnherr, A. M., Toole, J. M.,  
1142 & Watson, A. J. (2012). Turbulence and diapycnal mixing in drake passage. *J. Phys.*  
1143 *Oceanogr.*, *42*(12), 2143–2152. doi: 10.1175/JPO-D-12-027.1
- 1144 St. Laurent, L. C., Toole, J. M., & Schmitt, R. W. (2001). Buoyancy forcing by turbulence  
1145 above rough topography in the abyssal Brazil Basin. *J. Phys. Oceanogr.*, *31*(12),  
1146 3476–3495. doi: 10.1175/1520-0485(2001)031<3476:BFBTAR>2.0.CO;2
- 1147 Su, Z., Wang, J., Klein, P., Thompson, A. F., & Menemenlis, D. (2018). Ocean subme-  
1148 soscales as a key component of the global heat budget. *Nat. Commun.*, *9*(1), 1–8. doi:  
1149 10.1038/s41467-018-02983-w
- 1150 Talley, L. D. (2013). Closure of the global overturning circulation through the Indian, Pacific,  
1151 and southern oceans. *Oceanography*, *26*(1), 80–97. doi: 10.5670/oceanog.2013.07
- 1152 Tamsitt, V., Drake, H. F., Morrison, A. K., Talley, L. D., Dufour, C. O., Gray, A. R., ...  
1153 Weijer, W. (2017, dec). Spiraling pathways of global deep waters to the surface of the  
1154 Southern Ocean. *Nat. Commun.*, *8*(1). doi: 10.1038/s41467-017-00197-0
- 1155 Thomas, L. N., Taylor, J. R., Ferrari, R., & Joyce, T. M. (2013, jul). Symmetric instability  
1156 in the Gulf Stream. *Deep. Res. Part II Top. Stud. Oceanogr.*, *91*, 96–110. doi: 10.1016/  
1157 j.dsr2.2013.02.025
- 1158 Thorpe, S. A., & Liu, Z. (2009). Marginal instability? *J. Phys. Oceanogr.*, *39*(9), 2373–2381.  
1159 doi: 10.1175/2009JPO4153.1
- 1160 Toggweiler, J. R. (1994). The Ocean’s Overturning Circulation. *Phys. Today*, *47*(11),  
1161 45–50. doi: 10.1063/1.881425
- 1162 Tomczak, M., & Large, D. G. B. (1989). Optimum multiparameter analysis of mixing in  
1163 the thermocline of the eastern Indian Ocean. *J. Geophys. Res.*, *94*(C11), 16141. doi:  
1164 10.1029/jc094ic11p16141
- 1165 Trossman, D. S., Arbic, B. K., Garner, S. T., Goff, J. A., Jayne, S. R., Metzger, E. J.,  
1166 & Wallcraft, A. J. (2013). Impact of parameterized lee wave drag on the energy  
1167 budget of an eddying global ocean model. *Ocean Model.*, *72*, 119–142. doi: 10.1016/  
1168 j.ocemod.2013.08.006
- 1169 Tulloch, R., Ferrari, R., Jahn, O., Klocker, A., Lacasce, J., Ledwell, J. R., ... Watson, A.  
1170 (2014). Direct estimate of lateral eddy diffusivity upstream of drake passage. *J. Phys.*  
1171 *Oceanogr.*, *44*(10), 2593–2616. doi: 10.1175/JPO-D-13-0120.1
- 1172 Voet, G., Alford, M. H., MacKinnon, J. A., & Nash, J. D. (2020). Topographic Form  
1173 Drag on Tides and Low-Frequency Flow: Observations of Nonlinear Lee Waves over  
1174 a Tall Submarine Ridge near Palau. *J. Phys. Oceanogr.*, 1489–1507. doi: 10.1175/  
1175 jpo-d-19-0257.1
- 1176 Vosper, S. B. (2004). Inversion effects on mountain lee waves. *Q. J. R. Meteorol. Soc.*,  
1177 *130*(600 PART A), 1723–1748. doi: 10.1256/qj.03.63
- 1178 Walin, G. (1982). On the relation between sea-surface heat flow and thermal circulation in  
1179 the ocean. *Tellus*, *34*(2), 187–195. doi: 10.3402/tellusa.v34i2.10801
- 1180 Waterhouse, A. F., Mackinnon, J. A., Nash, J. D., Alford, M. H., Kunze, E., Simmons,  
1181 H. L., ... Lee, C. M. (2014). Global patterns of diapycnal mixing from measurements  
1182 of the turbulent dissipation rate. *J. Phys. Oceanogr.*, *44*(7), 1854–1872. doi: 10.1175/  
1183 JPO-D-13-0104.1
- 1184 Waterman, S., Naveira Garabato, A. C., & Polzin, K. L. (2013). Internal waves and  
1185 turbulence in the antarctic circumpolar current. *J. Phys. Oceanogr.*, *43*(2), 259–282.  
1186 doi: 10.1175/JPO-D-11-0194.1
- 1187 Waterman, S., Polzin, K. L., Garabato, A. C., Sheen, K. L., & Forryan, A. (2014). Suppres-  
1188 sion of internal wave breaking in the antarctic circumpolar current near topography.  
1189 *J. Phys. Oceanogr.*, *44*(5), 1466–1492. doi: 10.1175/JPO-D-12-0154.1
- 1190 Watson, A. J., Ledwell, J. R., Messias, M. J., King, B. A., Mackay, N., Meredith, M. P.,  
1191 ... Naveira Garabato, A. C. (2013). Rapid cross-density ocean mixing at mid-depths  
1192 in the Drake Passage measured by tracer release. *Nature*, *501*(7467), 408–411. doi:

- 1193 10.1038/nature12432  
1194 Wenegrat, J. O., & Thomas, L. N. (2020). Centrifugal and symmetric instability during  
1195 Ekman adjustment of the bottom boundary layer. *J. Phys. Oceanogr.*, *50*, 1793–1812.  
1196 doi: 10.1175/JPO-D-20-0027.1
- 1197 Whalen, C. B., de Lavergne, C., Naveira Garabato, A. C., Klymak, J. M., MacKinnon,  
1198 J. A., & Sheen, K. L. (2020). Internal wave-driven mixing: governing processes and  
1199 consequences for climate. *Nat. Rev. Earth Environ.*, *1*(11), 606–621. doi: 10.1038/  
1200 s43017-020-0097-z
- 1201 Winters, K. B., & Armi, L. (2012). Hydraulic control of continuously stratified flow over  
1202 an obstacle. *J. Fluid Mech.*, *700*, 502–513. doi: 10.1017/jfm.2012.157
- 1203 Winters, K. B., & Armi, L. (2014). Topographic control of stratified flows: Upstream jets,  
1204 blocking and isolating layers. *J. Fluid Mech.*, *753*, 80–103. doi: 10.1017/jfm.2014.363
- 1205 Wunsch, C., & Ferrari, R. (2004). Vertical Mixing, Energy, and the General Circulation of  
1206 the Oceans. *Annu. Rev. Fluid Mech.*, *36*(1), 281–314. doi: 10.1146/annurev.fluid.36  
1207 .050802.122121
- 1208 Zika, J. D., Sallee, J. B., Meijers, A. J., Naveira-Garabato, A. C., Watson, A. J., Messias,  
1209 M. J., & King, B. A. (2020). Tracking the spread of a passive tracer through Southern  
1210 Ocean water masses. *Ocean Sci.*, *16*(2), 323–336. doi: 10.5194/os-16-323-2020

1 **Enhanced upwelling of Antarctic Bottom Water by**  
2 **topographic interaction of water mass interfaces**

3 **L. E. Baker<sup>1</sup>, A. Mashayek<sup>1</sup>, A. C. Naveira Garabato<sup>2</sup>**

4 <sup>1</sup>Imperial College London, United Kingdom

5 <sup>2</sup>University of Southampton, Southampton, United Kingdom

6 **Key Points:**

- 7 • Sharp density interfaces exist between Antarctic Bottom Water and overlying Cir-  
8 cumpolar Deep Water in the Drake Passage  
9 • The sharpness of the interfaces leads to rich submesoscale and internal wave dynamics  
10 and complex topographic interactions  
11 • Such dynamics may contribute significantly to upwelling of Antarctic Bottom Water

---

Corresponding author: Lois Baker, [l.baker18@imperial.ac.uk](mailto:l.baker18@imperial.ac.uk)

**Abstract**

The lower cell of the meridional overturning circulation (MOC) is sourced by dense Antarctic Bottom Water (AABW), which forms and sinks around Antarctica and subsequently fills the abyssal ocean. For the MOC to ‘overturn’, these dense waters must upwell through mixing with lighter waters above. Here, we investigate the processes underpinning such mixing, and the resulting water mass transformation, using an observationally forced, high-resolution numerical model of the Drake Passage in the Southern Ocean. In the Drake Passage, the mixing of dense AABW formed in the Weddell Sea with lighter deep waters transported from the Pacific Ocean by the Antarctic Circumpolar Current is catalysed by energetic flows impinging on rough topography. We find that multiple topographic interaction processes act to facilitate mixing of the two water masses, ultimately resulting in upwelling of waters with neutral density greater  $28.19 \text{ kg m}^{-3}$ , and downwelling of the lighter waters above. In particular, we identify the role of sharp density interfaces between AABW and overlying waters, and find that the dynamics of the interfaces’ interaction with topography can enhance mixing. Such sharp interfaces between water masses have been observed in several parts of the global ocean, but are unresolved and unrepresented in ocean and climate models. We suggest that they are likely to play an important role in abyssal dynamics and mixing, and therefore require further exploration.

**Plain Language Summary**

Dense, cold waters are formed near Antarctica, then sink and spread through the deep ocean. The global overturning circulation is maintained by the upwelling of these dense waters back to the surface. This circulation allows the abyssal ocean to exchange heat, carbon and other tracers with the upper ocean and atmosphere, and is therefore a key regulator of the climate system. The upwelling happens due to turbulence in the deep ocean mixing together dense waters with lighter waters above. This turbulent mixing is often caused by the interaction of currents with rough seafloor topography, but the processes and resulting upwelling are not well understood. In this study, we use a high-resolution, realistic numerical simulation to investigate the processes causing turbulent mixing and upwelling of dense waters in an energetic region of the Southern Ocean. We find that there are sharp interfaces between the Antarctic-sourced dense waters and the overlying lighter waters, and that these interfaces themselves play a dynamic role in generating turbulent mixing and upwelling. The interfaces are not resolved or represented in global climate models, so their impact on the deep-ocean circulation requires further exploration.

**1 Introduction**

Sea ice formation and surface cooling near Antarctica create the densest waters in the global ocean (Marshall & Speer, 2012; Talley, 2013; A. C. Naveira Garabato et al., 2014). These Antarctic Bottom Waters (AABW) sink and travel northwards below the lighter water masses, filling most of the abyssal ocean with dense, cold, relatively fresh water (Lumpkin & Speer, 2007; Johnson, 2008; Talley, 2013). Such formation of AABW feeds the lower cell of the meridional overturning circulation (MOC). For these waters to upwell back to the surface (for if they did not, the ocean would fill up with dense waters), they must first upwell across density surfaces by transforming diabatically to lighter waters. Once they are sufficiently light, they then enter the upper cell of the MOC, where they are drawn adiabatically to the surface by westerly winds in the Southern Ocean (Toggweiler, 1994; Marshall & Speer, 2012; Talley, 2013). This overturning circulation ventilates the ocean abyss on timescales of centuries to millennia, with leading-order climatic consequences for the deep-ocean storage and release of carbon, heat and other tracers (Talley, 2013; Rae et al., 2018; Skinner et al., 2010).

The primary mechanism by which AABW can upwell across density surfaces is thought to be turbulent diapycnal mixing (Munk & Wunsch, 1998; Wunsch & Ferrari, 2004; De

62 Lavergne et al., 2016; Meredith & Naveira Garabato, 2021), the other non-negligible (yet  
63 secondary) mechanism being geothermal heating (Emile-Geay & Madec, 2009; Mashayek  
64 et al., 2013; Mashayek, Salehipour, et al., 2017; De Lavergne et al., 2016; Cimoli et al.,  
65 2019). Turbulent diapycnal mixing in the ocean occurs when small-scale turbulence causes  
66 irreversible mixing of fluids with different densities. Observations show that this turbulent  
67 mixing is enhanced by several orders of magnitude within a few hundred metres of the  
68 seafloor, compared to at mid-depths (Polzin et al., 1997; Ledwell et al., 2000; A. Naveira  
69 Garabato et al., 2004; J. MacKinnon et al., 2013; Waterhouse et al., 2014; J. A. MacKinnon  
70 et al., 2017). This is due to turbulent processes generated by the interaction of currents  
71 and tides with topography at the sea floor. These processes include internal waves, which  
72 are thought to be a primary source of mixing in the ocean interior (Wunsch & Ferrari,  
73 2004; J. A. MacKinnon et al., 2017; Sarkar & Scotti, 2017; Whalen et al., 2020), and other  
74 non-propagating boundary dynamics such as hydraulic processes (Baines, 1995; Legg &  
75 Klymak, 2008; Alford et al., 2013; Klymak, 2018) and Ekman layers (Garrett et al., 1993;  
76 A. C. Naveira Garabato et al., 2019; Spingys et al., 2021).

77 However, the implication of turbulent processes being bottom-generated is that the  
78 turbulent diffusivity increases towards topography, which induces downwelling rather than  
79 upwelling across density surfaces (Polzin et al., 1997; L. C. St. Laurent et al., 2001; De  
80 Lavergne et al., 2016; Ferrari et al., 2016). This apparent conundrum can be resolved by  
81 realising that, in some boundary layer next to topography, waters cannot become denser,  
82 and so must become lighter by mixing with waters above them, thereby inducing upwelling  
83 (Ferrari et al., 2016; McDougall & Ferrari, 2017). In recent years, there has been a significant  
84 focus on the nature of diapycnal mixing and density stratification in the bottom boundary  
85 layer, due to its key role in facilitating upwelling of dense waters, as reviewed by Polzin  
86 and McDougall (2022). The processes through which near-boundary waters mix, re-stratify  
87 and are exchanged with the ocean interior, and how those processes vary geographically  
88 throughout the global ocean, are a key open question.

89 The difficulty in answering this question resides in the extreme challenge involved in ob-  
90 serving turbulence in the abyssal ocean, particularly close to the seafloor. From a modelling  
91 perspective, high-resolution, process-resolving numerical simulations must be idealised and  
92 small-scale due to computational limitations, while more realistic simulations lack accurate  
93 parameterizations for mixing processes below the grid-scale. In this study, we use a realistic,  
94 wave- and submesoscale-resolving simulation to shed light onto the abyssal processes that  
95 generate mixing and drive transformation of AABW, as this water mass flows northwards  
96 through the Southern Ocean. We choose to study the Drake Passage, a region of intense  
97 flow-topography interaction and diapycnal mixing.

98 The Drake Passage is the gap between the tip of South America and the Antarctic  
99 Peninsula, through which the energetic Antarctic Circumpolar Current (ACC) flows from  
100 west to east. Rough topography including ridges, seamounts and abyssal hills (see figures  
101 1b,d) obstructs the deep layers of the ACC, generating intense diapycnal mixing in the  
102 bottom 1-2 km (A. Naveira Garabato et al., 2004; L. St. Laurent et al., 2012; Sheen et  
103 al., 2013; Mashayek, Ferrari, et al., 2017; Mackay et al., 2018). It is thought that the main  
104 contributor to mixing at depth in the Drake Passage is the breaking of internal lee waves  
105 generated by the impingement of the vigorous mesoscale eddies of the ACC upon the rough  
106 topography (L. St. Laurent et al., 2012; Sheen et al., 2013; Nikurashin & Ferrari, 2010),  
107 although the ways in which lee waves lose energy to diapycnal mixing are still not well  
108 understood (Legg, 2021).

109 The impact of concentrated ‘hotspots’ of topographic mixing, such as the Drake Pas-  
110 sage, on global deep-water upwelling has long been recognised (Munk & Wunsch, 1998).  
111 In addition, increased tracer residence time near large-scale ridges and fracture zones has  
112 been shown to contribute to enhanced diapycnal tracer transport in the Drake Passage  
113 (Mashayek, Ferrari, et al., 2017). This makes the Drake Passage an important location, not

114 only for transformation of dense bottom waters, but also for upwelling of climate-critical  
115 tracers such as heat, carbon and nutrients (Tamsitt et al., 2017).

116 The singular role of the Drake Passage in mixing AABW is partly due to its location. It  
117 is on the northward path of the dense AABW that is formed in the Weddell Sea to the south,  
118 called Weddell Sea Deep Water (Sievers & Nowlin, 1984; A. C. Naveira Garabato, Heywood,  
119 & Stevens, 2002, hereafter, NG02a). In the Drake Passage, Lower Circumpolar Deep Water  
120 (LCDW) sits above AABW, having entered the passage from the Pacific Ocean to the west.  
121 AABW occupies only the south-east part of the Passage (NG02a), so the AABW/LCDW  
122 interface directly impinges on the rough Drake Passage topography, experiencing high levels  
123 of topographically enhanced turbulent diapycnal mixing as a result. However, the processes  
124 by which the mixing at this interface takes place are not well understood. Furthermore, the  
125 boundary layer adjacent to topography in which diapycnal upwelling is expected to happen  
126 exists over a wide range of depths in the Passage, so it is not clear which density classes can  
127 be expected to upwell, and which may instead downwell.

128 Here, we investigate how flow-topography interaction processes in the Drake Passage act  
129 to mix AABW with the overlying LCDW, and quantify the resulting water mass transfor-  
130 mation. Although the Drake Passage is an energetic region, AABW export and northward  
131 transport occur in every major ocean basin, so it is expected that the dynamics described  
132 here are not unique, and could be of more generic importance to the transformation of  
133 AABW as it navigates the ACC and rough topography of the Southern Ocean.

## 134 **2 Drake Passage Simulation**

135 We use a wave-resolving model of the Drake Passage, described in detail in Baker and  
136 Mashayek (2022) (see Appendix A for summary). The simulation is performed using the  
137 hydrostatic configuration of the Massachusetts Institute of Technology general circulation  
138 model (MITgcm, Marshall et al., 1997), with  $0.01^\circ$  horizontal resolution (600 m to 1100 m)  
139 and 225 vertical levels with variable resolution that is  $< 25$  m at all depths above -4500 m  
140 (the range of depths relevant to this work). The depth and main bathymetric features are  
141 shown in figure 1d. Figure 1b shows a daily average of vertical vorticity in the simulation  
142 domain, demonstrating the interaction of deep-reaching mesoscale eddies with the rough  
143 topography.

144 The simulation is based upon a similar simulation that was developed as part of the  
145 DIMES (Diapycnal and Isopycnal Mixing Experiment in the Southern Ocean) field pro-  
146 gramme (Mashayek, Ferrari, et al., 2017). The DIMES experiment included a release in  
147 2009 of an anthropogenic tracer in the deep ACC upstream of Drake Passage, and subse-  
148 quent measurements of tracer concentration throughout the southeastern Pacific and the  
149 Scotia Sea over the following years, to investigate the impact of turbulent mixing. The mea-  
150 sured tracer distribution was used to infer turbulent diapycnal diffusivities (Watson et al.,  
151 2013; Zika et al., 2020), along with independent microstructure measurements of diffusivity  
152 (L. St. Laurent et al., 2012; Sheen et al., 2013; Merrifield et al., 2016), which are compared  
153 to our model diffusivity in figure 1c. Mashayek, Ferrari, et al. (2017) showed that their  
154 version of this model reproduced the spreading of the DIMES tracer using an imposed di-  
155 apycnal diffusivity distribution based on observations. The current version of the model has  
156 increased vertical resolution, allowing a better representation of topographically generated  
157 processes such as lee waves, and an improved sponge layer to reduce spurious processes at  
158 the open boundaries. We also use an online parameterization of diapycnal diffusivity (to be  
159 discussed later) rather than a static ‘map’, in order to represent the mixing associated with  
160 instability of resolved small-scale processes.

161 The simulation starts in July 2009 (corresponding to the period following the DIMES  
162 tracer release), and is integrated for 100 days. We use the final 30 days of the simulation

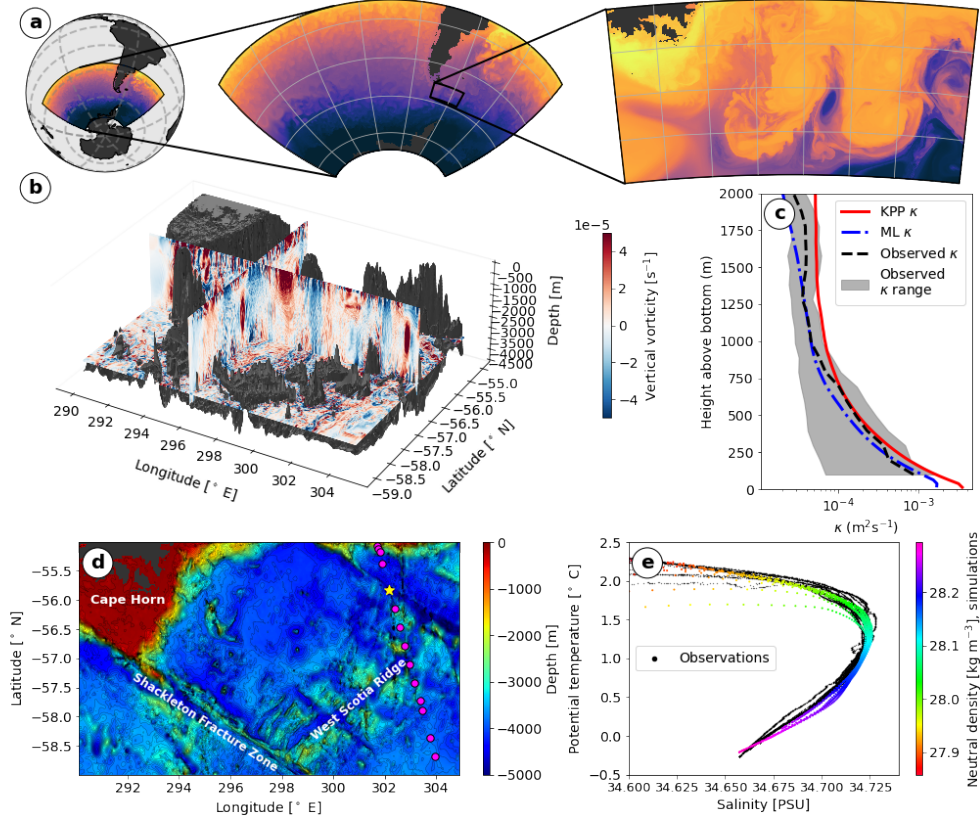


**Figure 1.** (a) Nesting diagram for Drake Passage model, showing parent simulation domain (left) and the Drake Passage domain presented here (right). (b) A daily average of vertical vorticity in the model. (c) Comparison of parameterized KPP diffusivity averaged with reference to height above bottom over the domain with microstructure observations from the Drake Passage (Merrifield et al., 2016) and a machine learning estimate of diffusivity (see §7). (d) Map of the simulation domain; shading and contours show depth. SR1b section stations are shown in pink, and the yellow star indicates the station at which profiles in figure 4 are taken. (e) Temperature-salinity diagram for the SR1b section observations and simulation data shown in figure 2. Simulation data are shaded with neutral density.

163 (early September to early October) for our analyses, with numbering of days referring to  
 164 days from the start of this selected period.

165 The model is nested within a simulation of a larger region of the Southern Ocean,  
 166 described in Tulloch et al. (2014) and shown in figure 1a. The larger simulation is itself  
 167 forced at the open boundaries by restoring velocity, temperature and salinity to the Ocean  
 168 Comprehensive Atlas (OCCA), a 3-year-long ocean state estimate that assimilated altimeter  
 169 data, satellite sea surface temperature, and Argo profiles (Forget, 2010). The hydrography  
 170 and eddy kinetic energy of the larger simulation was verified against observations by Tulloch  
 171 et al. (2014). Neither this simulation, nor ours, includes tidal forcing, thus the interaction  
 172 of tides with topography and corresponding generation of internal tides is not represented  
 173 in our model.

174 Our nested simulation uses open boundary conditions derived from the parent sim-  
 175 ulation for sea surface height, potential temperature, salinity, and meridional and zonal  
 176 velocities. In addition, a restoring boundary condition creates a sponge layer of 1 degree  
 177 thickness (removed for analysis purposes, except in figure 3) in which the potential tem-  
 178 perature, salinity, and zonal and meridional velocities are relaxed to the parent simulation.  
 179 The model hydrography is therefore expected to be realistic, and can be compared to in-situ  
 180 observations.

181 To validate the salinity, potential temperature, and neutral density in our simulation,  
 182 we use a set of shipboard conductivity-temperature-depth (CTD) observations that were  
 183 performed as part of the ACCLAIM (Antarctic Circumpolar Current Levels by Altimetry  
 184 and Island Measurements) project along the SR1b section in the Drake Passage in November  
 185 2009. The stations at which observations were taken are shown in figure 1d. We sample  
 186 our simulation at these locations for a like-for-like comparison, and in both cases compare  
 187 potential temperature, practical salinity, and neutral density (Jackett & McDougall, 1997).  
 188 The date of the fields sampled in our simulation is 10<sup>th</sup> October 2009 (day 30), which is  
 189 close to the observations in November 2009.

190 Figure 2 shows the observational data (left) and simulation data (right). Although  
 191 expectedly not identical (see later discussion of temporal variation of deep-ocean water  
 192 masses), there is very good agreement in temperature, salinity, and neutral density. In both  
 193 cases, a bottom layer of fresh, cold, dense water underlies saltier, warmer, lighter waters. A  
 194 temperature-salinity diagram (figure 1e) for the observations (black) and simulation (colour)  
 195 at the locations in figure 2 confirms the agreement between observations and simulation.

196 Turbulent processes and their associated mixing are not explicitly resolved in the model,  
 197 and must be parameterized. Typically, transition to turbulence occurs due to increased  
 198 vertical shear (shear instability), or unstable buoyancy gradients (convective instability),  
 199 although other instability mechanisms such as symmetric and inertial instabilities can also be  
 200 the primary cause of instability in geophysical flows, leading to secondary shear or convective  
 201 instabilities (Thomas et al., 2013; A. C. Naveira Garabato et al., 2019). The susceptibility of  
 202 flows to be unstable to shear and convective instabilities can be captured by the Richardson  
 203 number  $Ri = N^2/S^2$ , which quantifies the ratio of the stabilising effect of stratification  $N^2$  to  
 204 the destabilising squared vertical shear of horizontal velocities  $S^2$ . The stratification  $N^2 =$   
 205  $\partial b/\partial z$  is defined to be the vertical gradient of buoyancy  $b = -\rho g/\rho_0$ , where  $\rho$  is the density  
 206 and  $\rho_0$  is a reference density, and the squared shear is given by  $S^2 = (\partial u/\partial z)^2 + (\partial v/\partial z)^2$ ,  
 207 where  $u$  and  $v$  are the zonal and meridional velocities respectively.

208 Stratified shear instability can be shown analytically to be possible below a critical  
 209 Richardson number  $Ri_c = 0.25$  by the Miles-Howard Theorem (Miles, 1961; Howard, 1961),  
 210 although at finite model resolution it is not clear what  $Ri_c$  should be, and several shear  
 211 instabilities can occur for  $Ri \sim O(1)$  (Caulfield, 2021). Convective instability occurs when  
 212  $Ri < 0$ , corresponding to unstable vertical buoyancy gradients with  $N^2 < 0$ . Susceptibility  
 213 to submesoscale instabilities, such as symmetric and inertial instabilities, can also be quan-

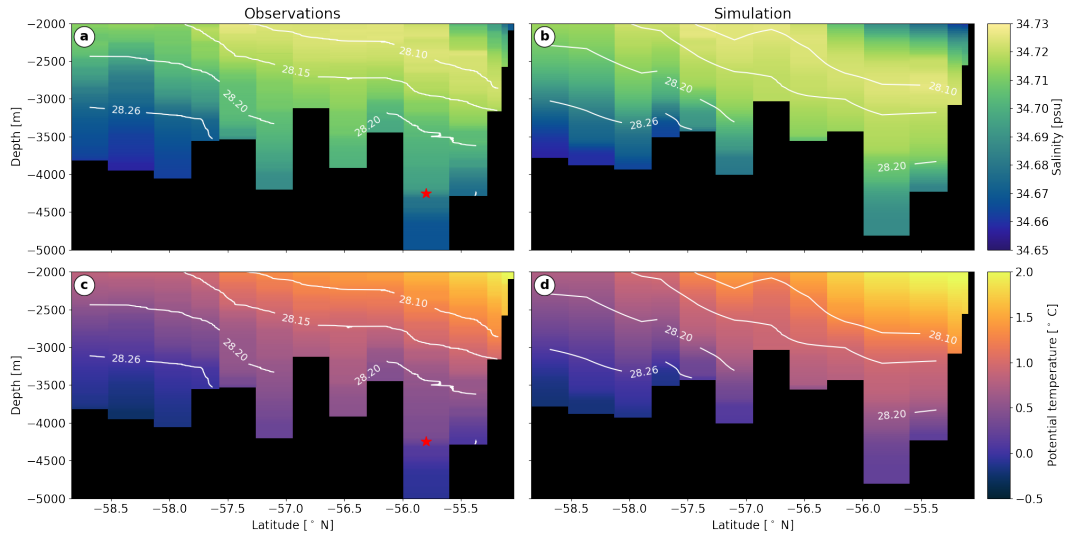


**Figure 2.** Comparison of (top) salinity and (bottom) potential temperature between (right) simulation and (left) observations. Contours indicate neutral density. Observations are from the SR1b section, collected in November 2009 as part of cruise JR195 of the ACCLAIM project, with locations shown in figure 1d. Simulation data are from a daily average on day 30, corresponding to 10<sup>th</sup> October 2009, and sampled at the same locations as the observations.

214 tified using a Richardson number criterion, which reduces to  $Ri < 1$  for larger-scale flows  
 215 in which the Earth’s rotation dominates inertial forces (Thomas et al., 2013). Support for  
 216 a criticality condition in  $Ri$  being appropriate in an oceanic context is given by evidence  
 217 for ‘marginal instability’; that is, observations of the Richardson number in an oceanic flow  
 218 fluctuating close to some critical value, typically near 0.25 (Thorpe & Liu, 2009; Smyth,  
 219 2020; Mashayek, Baker, et al., 2022).

220 The essence of  $Ri$  criticality is captured by the  $K$ -profile parameterization (KPP) (Large  
 221 et al., 1994), which enhances the vertical diffusivity  $\kappa$  when  $Ri < Ri_c$ . Here, we use the  
 222 KPP parameterization with  $Ri_c = 1/3$ , which is a reasonable measure of turbulence stabil-  
 223 ity in an environment when some background turbulence exists; see Mashayek et al. (2021);  
 224 Mashayek, Baker, et al. (2022) for a discussion. In order to validate the use of this parame-  
 225 terization, we compare diffusivity averaged in height-above-bottom coordinates throughout  
 226 our domain with DIMES observational, microstructure-based estimates of diffusivity in the  
 227 Drake Passage obtained by Merrifield et al. (2016). Figure 1c shows these profiles, which,  
 228 subject to observational uncertainty, assumptions with respect to mixing efficiency (Osborn,  
 229 1980; Gregg et al., 2018), and the known temporal and spatial variability of mixing events  
 230 (Moum, 2021), confirm that KPP does a satisfactory job in this domain, at least when  
 231 averaged with reference to height above bottom.

232 We parameterize mixing in this way to support our goal of demonstrating the processes  
 233 that lead to the transformation of AABW. However, in §7, we discuss the sensitivity of water  
 234 mass transformation to the parameterization of mixing, by presenting an independent, offline  
 235 machine learning estimate of diffusivity in our domain. This will highlight the need for more  
 236 sophisticated parameterization of oceanic processes at the sub-grid-scale of ocean models.

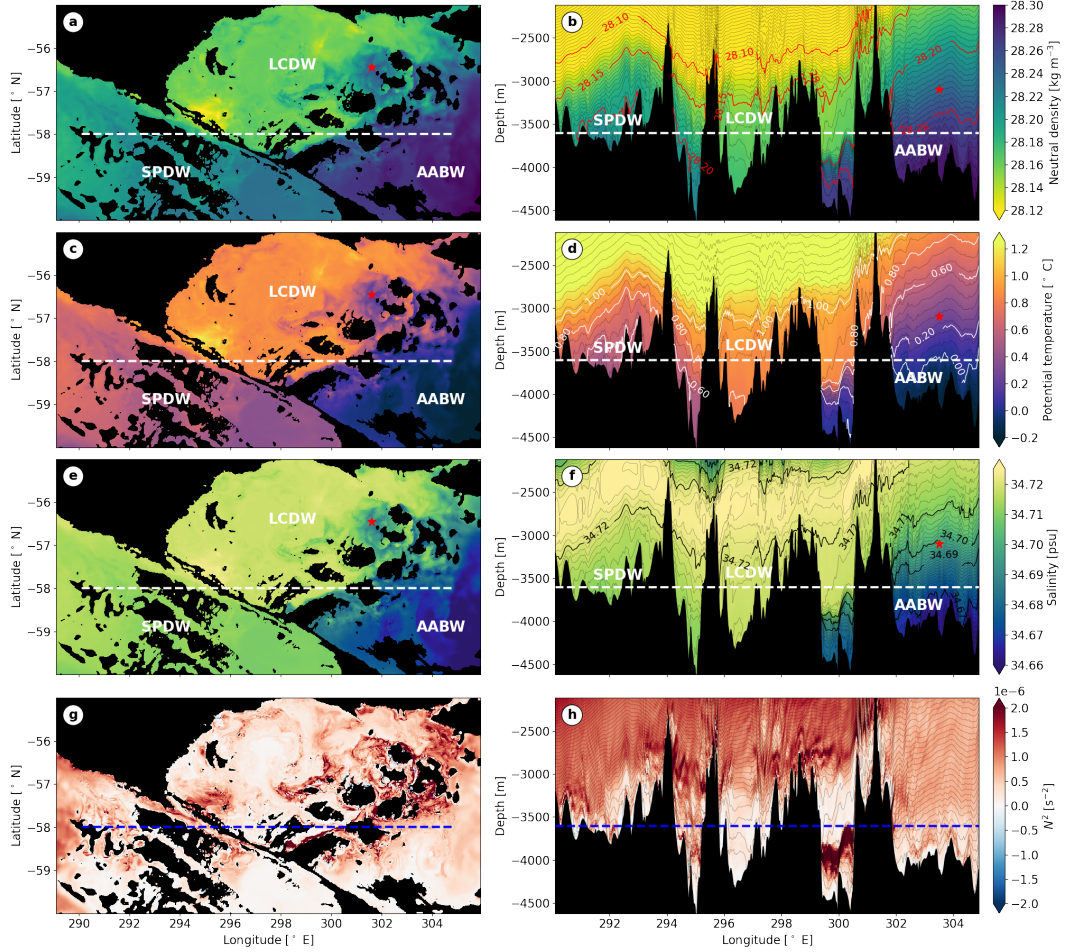


**Figure 3.** (a,b) Neutral density, (c,d) potential temperature, (e,f) salinity, and (g,h) stratification  $N^2$  at (left column) 3600 m depth and (right column)  $-58^\circ$  N. White and blue dashed lines show correspondence between columns. Red stars indicate locations of mixed AABW/SPDW referred to in the main text. A corresponding movie is available in the supporting information (movie S1).

237

### 3 Water mass classification

238

239

240

241

242

243

244

245

246

247

The Southern Ocean connects the major ocean basins (with the exception of the Arctic), and is a hub for global deep water masses. The lack of continental boundaries at the latitude band of the Drake Passage allows the strong westerly winds to draw deep isopycnals up to the surface, along which the deep waters of the global ocean can upwell and ventilate at the surface (Toggweiler, 1994; Lumpkin & Speer, 2007). The Drake Passage region is home to several distinct water masses formed in different parts of the global ocean. These water masses can be identified by their temperature, salinity and density properties, as well as by tracers such as oxygen, silicate and others (Tomczak & Large, 1989; Purkey et al., 2018; Liu & Tanhua, 2021). Here, we focus on temperature, salinity and neutral density, as tracers that can be calculated from our model.

248

249

250

251

The primary water mass of the Drake Passage, and of the Southern Ocean, is Circumpolar Deep Water (CDW), which is advected around the Southern Ocean by the ACC. The denser class of this CDW is called Lower Circumpolar Deep Water (LCDW), and occupies the neutral density range between  $28.0 \text{ kg m}^{-3}$  and  $28.26 \text{ kg m}^{-3}$  (NG02a). LCDW is

252 characterised by a salinity maximum that is derived from North Atlantic Deep Water in the  
 253 Atlantic sector (Sievers & Nowlin, 1984, NG02a). A. C. Naveira Garabato, McDonagh, et  
 254 al. (2002) (hereafter, NG02b) define LCDW in the Drake Passage as having salinity gen-  
 255 erally above 34.70, exceeding 34.73 at its mid-depth maximum, and potential temperature  
 256 between 0.2 and 1.9° C. An additional dense variety of LCDW in the Drake Passage result-  
 257 ing from interaction of LCDW with the deep waters of the Ross Sea was defined by Sievers  
 258 and Nowlin (1984). This Southeast Pacific Deep Water (SPDW) is characterised by neutral  
 259 densities between 28.2 and 28.26 kg m<sup>-3</sup>, and is colder than 0.6 °, and fresher than 34.71  
 260 (NG02a).

261 AABW is defined by NG02a to have neutral densities greater than 28.26 kg m<sup>-3</sup>. In the  
 262 Drake Passage, the relevant variety of AABW is Weddell Sea Deep Water (WSDW), which  
 263 is formed in the Weddell Sea to the south of the Drake Passage by the mixing of dense,  
 264 shelf-derived Weddell Sea Bottom Waters with CDW. WSDW flows northward at depth  
 265 over the South Scotia Ridge and into the Scotia Sea before reaching the Drake Passage  
 266 (NG02b). Using a global simulation with a tracer injection in the Weddell Sea, Solodoch  
 267 et al. (2022) showed that WSDW travels only downstream of the Drake Passage, with high  
 268 concentrations in the Atlantic basin, and eventually occupying the Indian basin and west  
 269 Pacific basin. WSDW is fresher, colder and denser than the overlying LCDW.

270 Figures 3a,c,e show neutral density, potential temperature, and salinity at 3600 m depth  
 271 in the simulation. At this depth, there is a clear demarcation of three distinct water masses,  
 272 separated from each other by the north-west/south-east running ridge of the Shackleton  
 273 Fracture Zone, and the south-west/north-east running West Scotia Ridge system (see figure  
 274 1d for labelling of bathymetric features). The vertical structures of these water masses  
 275 are illustrated in figures 3b,d,f, with the dashed lines showing the depth and latitudinal  
 276 correspondence between the left and right columns. Movie S1 shows some of these panels  
 277 over a 30-day period, and reveals that the locations and depths of the water masses vary  
 278 with time.

279 With reference to the above definitions of Drake Passage water masses, figure 3b shows  
 280 that most of the domain below 2000 m depth is filled with LCDW. The salinity maximum  
 281 described above that is characteristic of LCDW is evident in figure 3f, and has a value of  
 282 34.73. The denser, fresher waters of the LCDW below 28.2 kg m<sup>-3</sup> can be identified as  
 283 SPDW. At 3600 m depth, there is a clear lateral boundary (seen in figures 3a,c,e) between  
 284 the denser SPDW and the lighter class of LCDW, formed by the ridge of the Shackleton  
 285 Fracture Zone. The denser SPDW is unable to overflow this ridge, so the basin in the north  
 286 of the domain is filled with the lighter LCDW only, as can be seen in figures 3b,d,f.

287 The neutral density contour of 28.26 kg m<sup>-3</sup>, potential temperature contour of 0.2°C,  
 288 and salinity contour 34.69 are almost co-located, consistent with the definition by NG02b,  
 289 of the boundary between LCDW and the colder, fresher WSDW. WSDW is only present in  
 290 the south-east of the domain, consistent with its origin in the Weddell Sea and westward  
 291 path from the South Scotia Ridge to the Drake Passage. From figure 3a,c,f, it is clear that  
 292 WSDW is also topographically bounded - to the west from the SPDW by the Shackleton  
 293 Fracture Zone, and to the north-west by the West Scotia Ridge. Some lighter WSDW does  
 294 however overflow the West Scotia Ridge, in particular during a significant event around day  
 295 20 (visible in movie S1, and to be discussed further in §5.3.2). This highlights the temporal  
 296 variability of the water mass locations.

## 297 4 Stratified water mass interfaces

298 There are often sharp interfaces between the different water masses in the simulation,  
 299 with corresponding high stratification due to their differing densities. Figures 3g,h show that  
 300 stratification is enhanced at several interfaces in the domain. The elevated stratification is  
 301 due to sharp gradients in both salinity (figure 3b) and temperature (figure 3d). This is

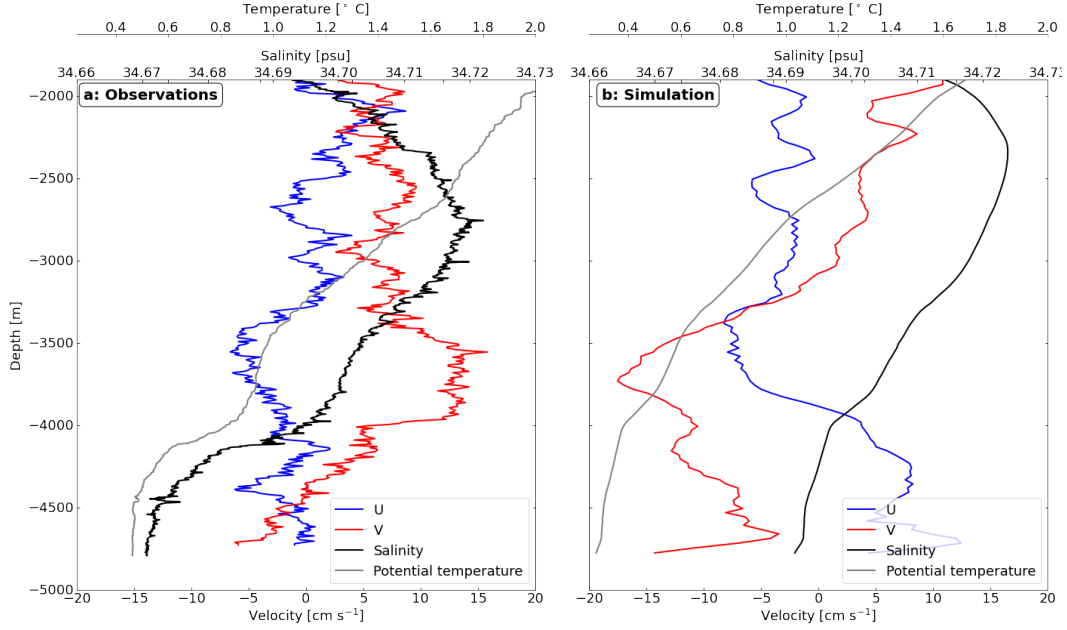


**Figure 4.** Velocity, temperature and salinity profiles at the location shown by the yellow star in figure 1d. Steps in temperature and salinity are accompanied by strong vertical shear of horizontal velocities. (a) In-situ observational data from DIMES, March 2013; and (b) simulation data on day 0.

302 consistent with the observations of Sievers and Nowlin (1984), who, on investigating the  
 303 various water masses of the Drake Passage, found that they were generally separated by  
 304 highly stratified interfaces, which they termed stability strata.

305 Steps in salinity and temperature have been previously observed at many locations in  
 306 the global ocean, and interpreted as boundaries between water masses; in particular in the  
 307 Drake Passage (Sievers & Nowlin, 1984), the East Scotia Sea (Meredith et al., 2013), and  
 308 the South West Atlantic (Reid et al., 1977). In the observations shown in figure 2a,c, sharp  
 309 gradients in temperature and salinity are also visible, for example at the location marked  
 310 by a red star.

311 In a different set of observations along transect SR1b, taken by the DIMES project  
 312 in March 2013, there are similar steps in temperature and salinity at depth, which were  
 313 co-located with high vertical shear as measured with a lowered acoustic Doppler current  
 314 profiler (ADCP). These steps and the corresponding velocities are shown in figure 4a, with  
 315 one such step and associated sharp vertical velocity gradient located just below 4000 m  
 316 depth. A corresponding profile at the same location from the simulation is shown in figure  
 317 4b, also demonstrating a step in temperature and salinity just above 4000 m depth, with  
 318 co-located vertical gradients in horizontal velocities. The occurrence of vertical shear of  
 319 horizontal velocities at a sharp density interface might be expected if the interface is tilted  
 320 horizontally, creating a strong horizontal buoyancy gradient and thereby vertical shear, in  
 321 order to maintain thermal wind balance. We will later demonstrate this mechanism using  
 322 the simulation.

323 The presence of sharp interfaces between water masses and the corresponding high  
 324 stratification, both in observations and in our model, is of great interest, as it is likely to  
 325 relate to how AABW mixes with overlying waters. Can the sharpness of an interface give

us insight into the mixing that its bounding water masses have experienced in the past, or are there other mechanisms that generate and destroy strong interfacial gradients?

There is evidence in the simulation (for example, at locations marked with a red star in figure 3) of waters that have properties intermediate between those of WSDW and LCDW. These waters are lighter than  $28.26 \text{ kg m}^{-3}$  (i.e. lighter than WSDW), but are also fresher than the freshest LCDW (SPDW) entering from the west of the domain. Thus, the waters in question are likely to be the result of WSDW mixing with the LCDW above. NG02a note that the WSDW entering the Drake Passage from the east is the lightest fraction of WSDW overflowing the South Scotia Ridge from the Weddell Sea, and is warmer and more saline than ‘pure’ WSDW following intense diapycnal mixing with LCDW (specifically, SPDW) on its westward transit to the Drake Passage. The easternmost part of the domain shown in figure 3b,d,f,h does not exhibit a sharp interface between AABW and SPDW, suggesting that the water masses have been rather thoroughly mixed.

However, elsewhere in the domain, strongly stratified interfaces do exist, albeit not always exactly aligned with the definitions given above for the LCDW/SPDW/WSDW boundaries (e.g., see figure 3h). These interfaces are also present in the larger SO simulation in which this model is nested (see §2 and figure 1a), which can resolve them with its vertical resolution of 50 m. The interfaces may therefore be inherited from observations via this larger model and the ocean state estimate with which it is itself forced. Although it is possible that the sharp interfaces are purely inherited remnants of the initial meeting of the distinct water masses (and a lack of mixing between such waters), the spatial heterogeneity of interface sharpness points to the leading-order involvement of a dynamical mechanism besides mixing. In the upper ocean, frontogenesis is well known to sharpen pre-existing horizontal density gradients (Hoskins, 1982; McWilliams, 2021), and there is also evidence of frontogenesis acting at submesoscale fronts in the ocean interior (Siegelman et al., 2020). It is clear from figure 3h that interfaces are often tilted from the horizontal. This is likely due to the flow moving over large-scale bottom topography, geographical variations in the water mass locations, and the passing of mesoscale eddies. The horizontal tilting of interface results in horizontal density gradients; frontal processes may therefore occur in the deep ocean to sharpen or widen these ambient gradients.

A further implication of the occurrence of water mass interfaces is the modification of dynamics associated with the layer of high stratification itself. Next, we investigate the potential impact of water mass interfaces on mixing processes in the deep ocean.

## 5 The phenomenology of topographic mixing

We wish to understand how different physical processes contribute to enhancing turbulence near topography. As discussed in §2, the Richardson number  $Ri = N^2/S^2$  can be used to quantify the susceptibility of a flow to shear and convective instabilities, and it is a Richardson number-based criterion that informs the mixing parameterization in the model. We therefore consider mechanisms that decrease stratification  $N^2$  and increase vertical shear  $S^2$  as a proxy for enhancing diapycnal mixing on the sub-grid-scale.

### 5.1 The nature of modelled mixing

Figure 5 and the corresponding movie S2 illustrate the complex dynamics of flow-topography interaction in the simulation. Figure 5a shows the Richardson number, and figure 5b the corresponding vertical diffusivity  $\kappa$ , for an hourly average of a section of the simulation at  $-57^\circ$  N. In general,  $\kappa$  is at its background value of  $5 \times 10^{-5} \text{ m}^2 \text{ s}^{-1}$  outside of the bottom few hundred metres, and outside of the upper-ocean mixed layer (not shown), corresponding to Richardson numbers greater than the critical value  $Ri_c = 1/3$  used here. In some locations, breaking topographic waves enhance  $\kappa$  up to 1000 m above the bottom. Within the bottom few hundred metres,  $\kappa$  is enhanced by the KPP

375 parameterization due to shear instability ( $0 < Ri < Ri_c$ ) or convective instability ( $Ri < 0$ ).  
 376 From consideration of the stratification (figure 5c) and squared vertical shear (figure 5d), it is  
 377 clear that many of the areas of enhanced  $\kappa$  are due to both high shear and low stratification,  
 378 acting together to decrease  $Ri$ . Furthermore, figure 5c shows that there are several areas of  
 379 unstable stratification close to the boundary, indicating conditions for convective instability  
 380 and overturning. These patches of  $N^2 < 0$  are a feature throughout the domain, and play  
 381 an important role in the near-boundary dynamics.

To understand how these areas of convective instability form, we can consider the simple unforced buoyancy equation:

$$\frac{\partial b}{\partial t} = -\mathbf{u} \cdot \nabla b + \frac{\partial}{\partial z} \left( \kappa \frac{\partial b}{\partial z} \right), \quad (1)$$

where  $b$  is buoyancy,  $\mathbf{u}$  is velocity, and the horizontal component of diffusion is taken to be zero, since the vertical gradients of the density and turbulent density flux tend to dominate over the horizontal components (Ferrari et al., 2016). Taking the vertical derivative, we obtain:

$$\frac{DN^2}{Dt} = - \underbrace{\frac{\partial \mathbf{u}_H}{\partial z} \cdot \nabla_H b}_{(A)} - \underbrace{\frac{\partial w}{\partial z} N^2}_{(B)} + \underbrace{\frac{\partial^2}{\partial z^2} (\kappa N^2)}_{(C)}, \quad (2)$$

382 where  $D/Dt \equiv \partial/\partial t + \mathbf{u} \cdot \nabla$  is the full derivative following a water parcel, and  $H$  represents  
 383 the horizontal components of velocity and the gradient operator.

384 Each of the three terms on the right hand side of equation (2) represents a way in  
 385 which the stratification following a water parcel can change. Term (C) encapsulates verti-  
 386 cal diffusion, and it is through this term that turbulent processes (represented within the  
 387 parameterized turbulent diffusivity  $\kappa$ ) act to diffuse vertical gradients in buoyancy, thereby  
 388 causing irreversible mixing. The vertical gradients of  $\kappa$  and  $N^2$  and corresponding turbu-  
 389 lent buoyancy fluxes play a leading-order role in the boundary layer dynamics (Polzin &  
 390 McDougall, 2022). However, this term alone cannot change the sign of  $N^2$  from positive  
 391 to negative. Suppose that (A) and (B) are zero, and that initially  $N^2 > 0$  everywhere  
 392 except on the boundary, and zero at the boundary itself since there should be no buoyancy  
 393 flux across the boundary (an insulating boundary condition). Then, suppose that at some  
 394 interior location  $N^2$  becomes zero. Given  $\kappa \geq 0$ , this point is thus a local minimum of  $\kappa N^2$ ,  
 395 so (C) is greater than zero, and  $DN^2/Dt \geq 0$  by equation (2), hence the sign of  $N^2$  cannot  
 396 change.

397 Similarly, term (B), which represents changes to the vertical buoyancy gradient due  
 398 to vertical convergence or divergence of the vertical velocity, cannot alone change the sign  
 399 of  $N^2$ . If (A) and (C) are zero, the solutions to equation (2) are exponential, and thus  
 400 single-signed.

401 Therefore, term (A) must be responsible for generating areas of convective instability  
 402 from a stable flow. This term corresponds to vertical shear of horizontal velocities acting  
 403 upon horizontal buoyancy gradients, which physical intuition confirms can overturn isopy-  
 404 cnals – by advecting dense water above light water and creating conditions for convective  
 405 instability.

406 An important aspect of term (A) is that, if the velocities and buoyancy gradients are  
 407 in thermal wind balance, such that  $\mathbf{f} \times \partial \mathbf{u}_H / \partial z = -\nabla_H b$ , where  $\mathbf{f} = (0, 0, f)$  with  $f$  as the  
 408 Coriolis parameter, then (A) vanishes and this shear mechanism cannot cause overturning.  
 409 Thus, for convective instability conditions to occur in the absence of forcing (such as surface  
 410 cooling or bottom thermal flux), the flow must be unbalanced; this imbalance could be  
 411 associated with internal gravity waves, fronts, or boundary processes.

412 The preceding analysis serves to highlight the important role of vertical shear in gener-  
 413 ating conditions for instability. Not only is vertical shear needed to destabilise a statically

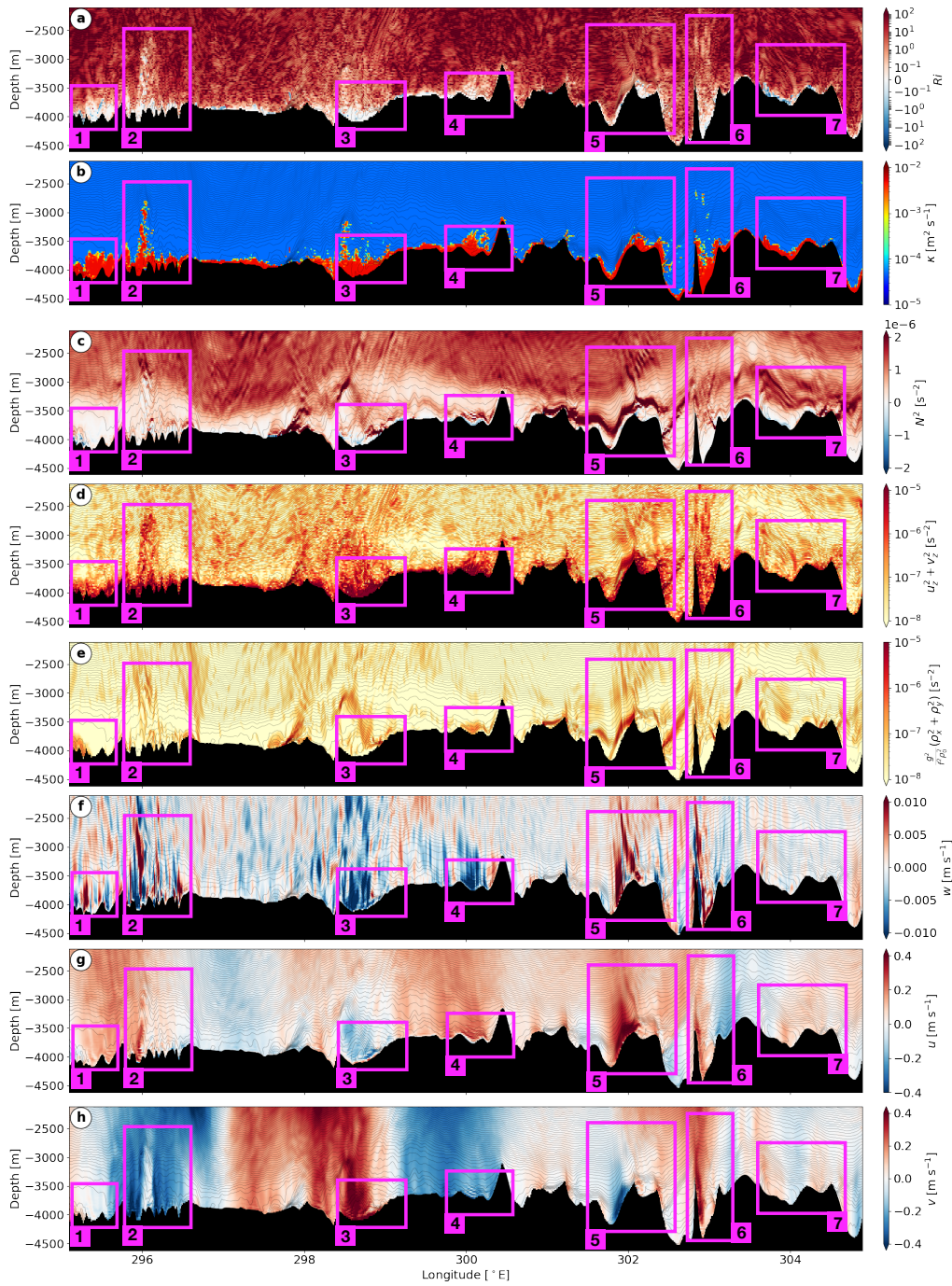


**Figure 5.** Various dynamical variables at  $-57^\circ$  N, demonstrating a range of mixing processes. (a) Richardson number, (b) vertical diffusivity, (c) stratification, (d) squared vertical shear of horizontal velocities, (e) squared vertical shear of horizontal velocities, as implied by the thermal wind balance relation applied to the horizontal density gradients, (f) vertical velocity, (g) zonal velocity, and (h) meridional velocity. Magenta boxes highlight processes discussed in the main text. A corresponding movie is available in the supporting information (movie S2).

414 stable flow via the onset of shear instability, but it is also required to create the conditions  
 415 for convective instability from horizontal buoyancy gradients. Having identified the role of  
 416 vertical shear in creating the conditions for mixing, we now discuss the physical processes  
 417 that govern vertical shear near the boundary.

## 418 **5.2 Topographically-induced processes**

419 First, we consider the complex topographic interaction processes that take place in the  
 420 absence of the highly stratified interfaces separating the different water masses. Then, we  
 421 examine the processes arising from the these interfaces' presence.

### 422 **5.2.1 Boundary layer frictional processes**

423 Wherever a flow encounters a boundary with friction (see Appendix A for a description  
 424 of the modelled no-slip boundary condition), shear may arise as the flow experiences drag  
 425 in a thin boundary layer. This drag alone can be expected to create shear even when the  
 426 topography is flat, and it is clear from figure 5d that vertical shear is always enhanced near  
 427 the boundary.

428 In a rotating geophysical flow, the force balance between friction, rotation, and pressure  
 429 gradients modifies the boundary layer dynamics by generating an Ekman spiral, in which  
 430 the flow turns clockwise (in the Southern Hemisphere) as the boundary is approached. We  
 431 find that the flow direction, averaged over the entire simulation domain, turns on average  
 432  $12^\circ$  clockwise in the bottom 25 m, and on average  $4^\circ$  clockwise in the 25 m above this,  
 433 consistent with Ekman theory. We are therefore permitting Ekman dynamics at the bottom  
 434 boundary, but not fully resolving them, since the depth of the Ekman layer is of the same  
 435 order as the 25 m vertical grid resolution.

436 When the bottom boundary is sloped, these dynamics become more complex yet. A  
 437 cross-slope flow can induce an upslope or downslope Ekman current, which can become ar-  
 438 rested by the restoring buoyancy force on isopycnals (MacCready & Rhines, 1991; Garrett  
 439 et al., 1993; Ruan et al., 2019, 2021). An example of a near-boundary flow that is consistent  
 440 with an unsteady upslope Ekman current is shown by the zonal and meridional velocities in  
 441 figure 5g,h in box 3, in which the flow turns clockwise in the bottom few grid cells, with the  
 442 corresponding enhanced vertical shear shown in figure 5d. Observational evidence suggests  
 443 that a downslope Ekman flow can generate low stratification and large shear near topogra-  
 444 phy, producing conditions favourable for the development of submesoscale instabilities and  
 445 intense mixing in a deep western boundary current (A. C. Naveira Garabato et al., 2019;  
 446 Spingys et al., 2021). Numerical studies also suggest that submesoscale instabilities dur-  
 447 ing Ekman adjustment may have an overlooked role in topographic mixing (Callies, 2018;  
 448 Wenegrat & Thomas, 2020). However, the rough topography and unsteady, energetic nature  
 449 of the flow in the Drake Passage suggests other explanations for the elevated diffusivities  
 450 several hundred metres above topography seen in this model.

### 451 **5.2.2 Lee waves, blocking, and breaking**

452 When stratified flows interact with rough topography, a number of processes can occur  
 453 that generate turbulence and mixing. For topographic wavenumbers  $\mathbf{k}$  such that  $f^2 <$   
 454  $(\mathbf{U} \cdot \mathbf{k})^2 < N^2$ , where  $\mathbf{U}$  and  $N$  are the near-bottom velocity and stratification, vertically  
 455 propagating lee waves are generated. Lee waves extract energy from the mean flow and cause  
 456 turbulent mixing when they break. They are thought to be a leading-order source of mixing  
 457 in the Southern Ocean (A. Naveira Garabato et al., 2004; Scott et al., 2011; Nikurashin &  
 458 Ferrari, 2011; Trossman et al., 2013; De Lavergne et al., 2016).

459 A recent study of the lee wave field in this simulation found that there was strong  
 460 and nonlinear lee wave generation throughout the domain, especially in areas of rough

461 topographic features such as the Shackleton Fracture Zone and the West Scotia Ridge, and  
 462 in areas of high bottom currents (Baker & Mashayek, 2022). The vertical velocity, shown in  
 463 figure 5f, exhibits (for example, box 2) lee waves generated at topography and propagating  
 464 vertically upwards. In this simulation, lee waves can propagate through the entire water  
 465 column and interact with the surface (Baker & Mashayek, 2021).

466 The mechanisms of lee wave breaking and resulting vertical distribution of mixing are  
 467 poorly constrained (Legg, 2021). In the presence of a strong lee wave field in the simulation,  
 468 there is enhanced diffusivity in the bottom 100-400 m (e.g., boxes 1 and 2, figure 5b),  
 469 consistent with the results of Klymak (2018) for idealised simulations with representative  
 470 Southern Ocean parameters and multi-scale topography. The waves generate high shear  
 471 and even areas of static instability in the lee of topography (figure 5c, box 2), and thus  
 472 contribute significantly to mixing near topography.

473 Above the bottom few hundred metres, the modelled lee waves generally do not become  
 474 shear- or convectively unstable, so vertical diffusivity is not enhanced by the KPP parame-  
 475 terization and, instead, the waves experience the background diffusivity. However, in some  
 476 locations, highly nonlinear lee waves do become unstable up to 1000 m above the bottom,  
 477 such as in box 2 (figure 5b,f).

478 The lack of any significant interior lee wave-driven mixing in the simulation suggests  
 479 a need for better parameterization of mixing driven by nonlinear wave interactions in the  
 480 ocean interior in models such as this that resolve only part of the internal wave spectrum.  
 481 However, the ultimate sink for lee wave energy in the interior remains poorly understood.  
 482 Observations in the Drake Passage have shown that rates of dissipation are an order of  
 483 magnitude smaller than would be expected if all lee wave energy was dissipated locally near  
 484 topography, which suggests that the waves have an energy sink elsewhere (Sheen et al., 2013;  
 485 Waterman et al., 2013, 2014; Cusack et al., 2017; Voet et al., 2020; Gutierrez-Villanueva et  
 486 al., 2022).

487 The topographic Froude number  $Fr = Nh/|\mathbf{U}|$ , where  $h$  is the characteristic height  
 488 of topography, indicates the nonlinearity of the generated lee wave field. When  $Fr \gtrsim 1$ ,  
 489 the flow cannot all go over a topographic obstacle, and is instead blocked or split, giving  
 490 rise to non-propagating processes as well as a nonlinear propagating lee wave field. These  
 491 non-propagating processes are also an important source of turbulence and mixing (Klymak,  
 492 2018; Klymak et al., 2021). Such processes include downslope windstorms (Klemp & Lilly,  
 493 1975; Peltier & Clark, 1979; Durran, 1986), hydraulic control and jumps (Winters & Armi,  
 494 2012, 2014), and wake vortices (Srinivasan et al., 2019), which can all generate high shear,  
 495 instabilities, and mixing. Box 6 in figure 5 shows an example of flow interacting with a tall  
 496 topographic feature. At its peak, lee waves are generated (visible in the vertical velocity  
 497 field, figure 5f, box 6), but velocities are accelerated down to the feature's base as the flow  
 498 is topographically steered (figures 5g,h, box 6). This generates shear (figure 5d, box 6) and  
 499 high diffusivity (figure 5b, box 6).

### 500 **5.3 Role of stratified interfaces**

501 The layers of high stratification that separate the various water masses discussed in §3  
 502 can dynamically influence the topographic interaction processes discussed above, as well as  
 503 creating new mechanisms of mixing.

#### 504 **5.3.1 Generation of vertical shear**

505 The interfaces between different water masses can be identified by the layers of high  
 506 stratification in figure 5c and movie S2, panel c. There is not one continuous interface, rather  
 507 several interfaces, separating different layers of fluid that move throughout the domain (as  
 508 illustrated by the salinity in movie S2, panel e). The complex patterns of the areas of high  
 509 stratification in figures 3g,h are further evidence of this. The layers are not horizontal,

510 but undulate with the topography (e.g., figure 5c, box 5), with the geographical location  
 511 of the water masses (e.g., figure 3b), and with the translation of mesoscale eddies through  
 512 the domain. The tilting of these vertically stratified interfaces creates strong horizontal  
 513 buoyancy gradients. In a non-rotating flow, baroclinic production of vorticity would act to  
 514 flatten the tilted isopycnals. However, in a rotating fluid, geostrophic adjustment acts to  
 515 increase vertical shear, such that the horizontal buoyancy gradients approach thermal wind  
 516 balance.

517 Figure 5e shows scaled horizontal buoyancy gradient  $g^2(\gamma_x^2 + \gamma_y^2)/f^2/\rho_0^2$ , where  $g$  is the  
 518 acceleration due to gravity,  $\rho_0$  is a reference density,  $\gamma$  is the neutral density, and subscripts  
 519 denote derivatives. Not only does this figure show that strong horizontal buoyancy gradients  
 520 correspond to the stratified interfaces (e.g. box 5), but it can also be compared to the vertical  
 521 shear in figure 5d. Were the flow in exact thermal wind balance, the two panels d and e  
 522 would be identical. There is a clear correspondence between areas of high vertical shear  
 523 (panel d), high horizontal buoyancy gradients (panel e), and stratified interfaces (panel c).  
 524 The zonal and meridional velocities (panels g and h) also exhibit jets next to topography  
 525 in box 5 due to the locally elevated vertical shear. Observational evidence for vertical shear  
 526 associated with stratified interfaces was presented in figure 4a, and based on this and our  
 527 simulation, we conclude that one of the mechanisms of generating vertical shear in the deep  
 528 ocean is the tilting of water mass interfaces.

529 However, it is not clear that this vertical shear and the interfaces themselves can then  
 530 cause instability. It was already shown in equation (2) that vertical shear in thermal wind  
 531 balance cannot cause overturning, and the interfaces by definition possess large stratification  
 532  $N^2$  alongside high squared vertical shear  $S^2$ ; thus, the Richardson number is not necessarily  
 533 reduced at the interfaces. For example, the regions of high shear in figure 5d, box 5, do not  
 534 correspond to increased diffusivity in figure 5b. Instead, it is the interaction of the interfaces  
 535 with topography that causes instability and generates mixing.

### 536 **5.3.2 Interaction with topography**

537 When the strong horizontal buoyancy gradients of the water mass interfaces interact  
 538 with the rough topography of the Drake Passage, they frequently cause overturning of  
 539 isopycnals and conditions for instability. Areas of unstable stratification near topography  
 540 associated with the passing of horizontal gradients in buoyancy (tilted isopycnals) can be  
 541 seen in figure 5c, boxes 1, 3, 4, and 7, and in movie S2. Friction at the boundary (§5.2.1) or  
 542 small-scale topographic processes such as lee waves (§5.2.2) perturb and sometimes overturn  
 543 tilted isopycnals as a dense water mass moves along topography, leaving behind it weakly  
 544 stratified or unstable fluid. This mechanism relies strongly on the temporal variability of  
 545 the water masses.

546 To demonstrate this temporal variability, we show in figure 6 and movie S3 an example  
 547 of a fast-moving overflow of dense waters over the West Scotia Ridge. As discussed in  
 548 §3, this class of water is lighter than the WSDW to the south-east of the domain, as it  
 549 has mixed with LCDW above. The top row of figure 6 shows salinity at 3600 m depth,  
 550 demonstrating how over a period of seven days, dense, fresh waters that were previously  
 551 trapped by the ridge (e.g., see figure 3c, showing the salinity field on day 0) push through  
 552 the topography and enter the northern part of the domain. This overflowing event is driven  
 553 by fast northward velocities associated with a surface-enhanced mesoscale eddy that spans  
 554 the entire water column (figure 6j,k,l). The corresponding motion of the stratified interface  
 555 over topography contributes to turbulence and mixing in its wake.

556 The second row of figure 6 corresponds to the white dashed lines in the top row, and  
 557 shows the progression of the denser water class as it flows northwards, using salinity as  
 558 a tracer. There are several stratified interfaces, the movement of which is clear from the  
 559 stratification time series in the third row, and from movie S3. Behind (to the south of) the  
 560 contact point of the interfaces with topography, there are areas of negative stratification

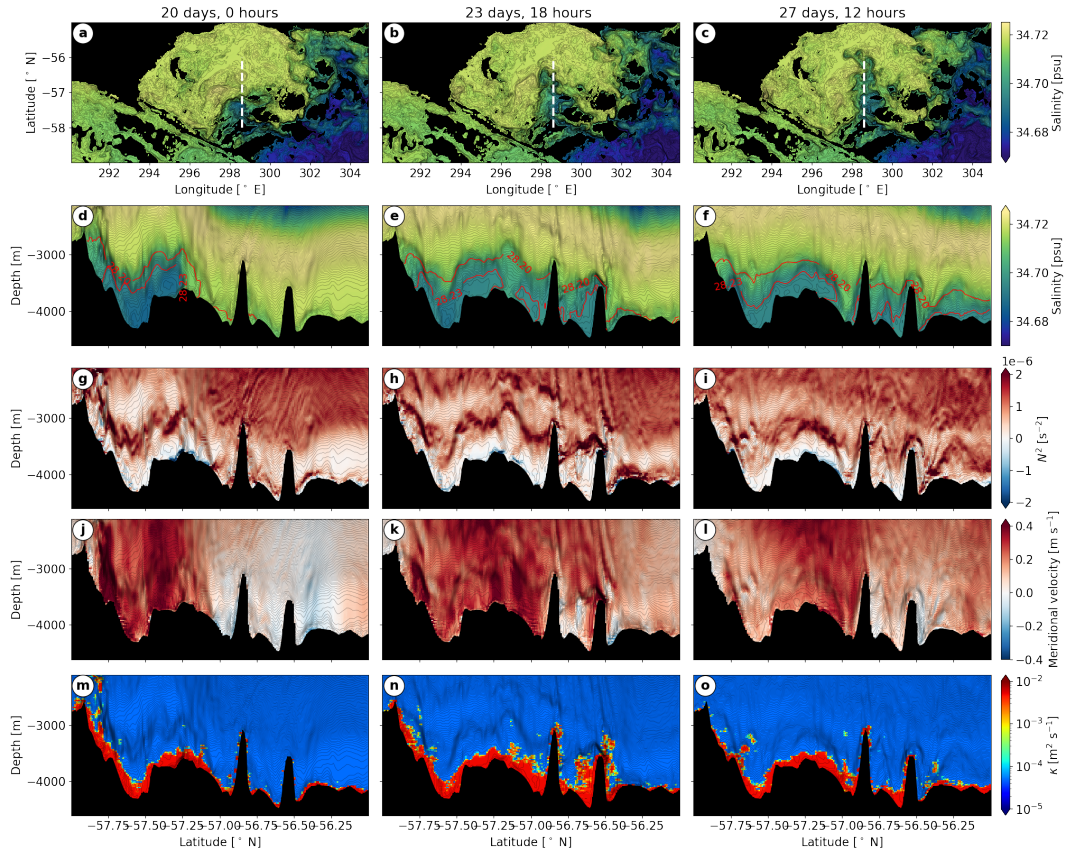


**Figure 6.** Time series (time increasing from left to right) over  $\sim 7$  days of an overflow of AABW passing northwards over the West Scotia Ridge. (a-c) Salinity at 3600 m depth, with white dashed line indicating the section shown in the remaining panels at  $298.6^\circ$  E. (d-f) Salinity, (g-i) stratification (or squared buoyancy frequency), (j-l) meridional velocity and (m-o) vertical diffusivity. All contours show neutral density. A corresponding movie is available in the supporting information (movie S3).

561 caused by the isopycnals overturning with the motion of the front. Beneath the interface,  
 562 after the contact point has passed, the fluid is weakly stratified and the areas of negative  
 563 stratification are persistent, slowly increasing in stability as they are mixed by the enhanced  
 564 vertical diffusivity.

565 The fast flow speeds and tilted isopycnals of the dense bottom current moving over the  
 566 rough topography result in increased diffusivity along the current's path, as shown in the  
 567 bottom row of figure 6. We will later present evidence that this event is associated with  
 568 increased upwelling of the dense waters.

### 569 **5.3.3 Impact on propagating lee waves**

570 The presence of the stratified interfaces near topography can also influence the genera-  
 571 tion, propagation and breaking of lee waves. While the deep ocean is generally considered to  
 572 be weakly and uniformly stratified, the impact of a stratified interface has been extensively  
 573 studied in the context of atmospheric mountain wave generation beneath a temperature  
 574 inversion or the highly stratified stratosphere. The occurrence of hydraulic jumps, breaking  
 575 lee waves, lee wave rotors (flow circulations in the lee of topography), resonant trapped lee  
 576 waves on the interface, and downslope wind storms have been found to be highly dependent  
 577 on the height of the stratified interface, the density difference across the interface, and the  
 578 topographic Froude number  $Fr$  (Klemp & Lilly, 1975; Durran, 1986; Vosper, 2004; Sheri-  
 579 dan & Vosper, 2006). Jagannathan et al. (2020) established that the location of a strong  
 580 density step above topography impacted whether or not it plunged downwards in the lee  
 581 of the topography, thereby giving rise to a wave field aloft that was six times more ener-  
 582 getic than in the absence of interface plunging. Armi and Mayr (2015) found that when a  
 583 strong density step exists above topography, this can act as a 'virtual topography' control-  
 584 ling the stratified flow response aloft. The presence of these density steps in the deep ocean  
 585 could therefore have implications on the way we represent topography in oceanic lee wave  
 586 parameterizations.

587 Away from topography, when encountering a region of high stratification, lee wave  
 588 horizontal velocities increase, resulting in enhanced nonlinearity, wave overturning, and  
 589 turbulence (Durran, 1986). Lee waves may also gain/lose energy to the mean flow or break  
 590 at critical levels through interaction with the vertical shear associated with thermal wind  
 591 balance of the tilted interfaces (Kunze & Lien, 2019; Baker & Mashayek, 2021). Abrupt  
 592 changes to the the mean flow through which lee waves propagate, such as those linked to  
 593 water mass interfaces, are largely neglected in the question of how and where lee waves  
 594 dissipate their energy, but may be important for catalysing wave instability.

595 Evidence of impact of the layers of high stratification on lee waves can be seen in figure  
 596 5. In box 2, a lee wave breaking is evident in the diffusivity (figure 5b) up to the level  
 597 where stratification increases significantly, suggesting that the enhancement in stratification  
 598 may increase nonlinearity of the wave, causing it to lose energy by breaking. In box 5, a  
 599 wave is generated above a strongly stratified interface, suggesting that the interface may be  
 600 acting as a 'virtual topography' (Armi & Mayr, 2015). A large lee wave is also generated  
 601 by the interaction of the front of the dense bottom current with topography in figure 6k  
 602 at  $-56.5^\circ$  N. It is clear that the presence of stratified interfaces in the Drake Passage may  
 603 alter the nature of lee wave generation, propagation and breaking, potentially modifying  
 604 the distribution of lee wave mixing in a way that would be difficult to take into account in  
 605 parameterizations.

## 606 **6 Water Mass Transformation**

607 In order to understand how deep waters are transformed to different densities by diapyc-  
 608 nal mixing, we calculate the water mass transformation rate, equivalent to the diapycnal  
 609 velocity integrated over a density surface. In particular, it is key to elucidate whether waters

610 at some density level upwell (become lighter), or downwell (become denser). This question  
 611 gives rise to a conundrum that has been the topic of active research over the past decade  
 612 (De Lavergne et al., 2016; Ferrari et al., 2016). The diapycnal turbulent flux of buoyancy  
 613  $F_b$  can be approximated using a diffusive flux law,  $F_b = -\kappa N^2$ , where  $\kappa$  is the vertical  
 614 diffusivity (Osborn, 1980). If  $\frac{\partial F_b}{\partial z} < 0$ , then waters become lighter (upwelling), whereas if  
 615  $\frac{\partial F_b}{\partial z} > 0$ , waters become denser (downwelling). Thus, if, as is generally observed,  $\kappa$  signifi-  
 616 cantly increases towards topography without a corresponding decrease in  $N^2$ , then  $\frac{\partial F_b}{\partial z} > 0$   
 617 and downwelling occurs rather than the necessary upwelling.

618 A resolution to this conundrum has been suggested by noting that at the bottom  
 619 boundary, in the absence of geothermal heat flux, an insulating boundary condition implies  
 620 that  $F_b = 0$ . Thus, in some boundary layer,  $F_b$  (which is strictly negative for stable vertical  
 621 buoyancy gradients) must decrease with height above bottom, implying upwelling. This has  
 622 given rise to an increasingly accepted theory that waters generally downwell in the stratified  
 623 ocean interior, with this downwelling compensated by strong upwelling near topography –  
 624 resulting in net upwelling (Ferrari et al., 2016; McDougall & Ferrari, 2017; Drake et al.,  
 625 2020). Here, we are able to verify this theory within the context of our simulation, subject  
 626 to model constraints on resolution of the bottom boundary layer and uncertainties in the  
 627 parameterization of vertical diffusivity.

## 6.1 Water mass transformation framework

628 We first define the diapycnal velocity  $\tilde{\mathbf{e}}$ , that is the velocity in the cross-density surface  
 direction. By subtracting the motion of an isopycnal surface itself from the Eulerian velocity  
 of a water parcel, Ferrari et al. (2016) show that

$$\tilde{\mathbf{e}} = \frac{\nabla \cdot \mathbf{F}_b}{|N^2|} \mathbf{n}, \quad (3)$$

629 where  $\mathbf{F}_b$  is the buoyancy flux, and  $\mathbf{n}$  is the normal to the isopycnal surface defined as  
 630 pointing towards higher buoyancy. Note that this may not always be in the positive vertical  
 631 direction, and as such our definition of ‘upwelling’ refers to upwelling in buoyancy space,  
 632 which may be vertically downwards in the presence of unstable stratification. We approx-  
 633 imate the divergence of the buoyancy flux by  $\nabla \cdot \mathbf{F}_b \sim -\partial(\kappa N^2)/\partial z$ . This approximation  
 634 is often made due to the occurrence of significantly larger vertical buoyancy gradients than  
 635 horizontal ones in the ocean interior, and here we do not apply a horizontal diffusivity in  
 636 the model, so do not have explicit horizontal buoyancy fluxes. The vertical buoyancy flux  
 637  $F_b = -\kappa N^2$  is set to zero at topography to satisfy the insulating boundary condition.

In order to quantify upwelling over a density surface, we use the water mass transfor-  
 mation framework of Walin (1982); Ferrari et al. (2016). The diapycnal velocity integrated  
 over a neutral density surface  $A(\gamma)$  is denoted  $\mathcal{E}(\gamma)$ , where  $\gamma$  is neutral density, and is given  
 by:

$$\mathcal{E}(\gamma) = \int_{A(\gamma)} \tilde{\mathbf{e}} \cdot \mathbf{n} dA \simeq -\frac{\rho_0}{g} \frac{\partial}{\partial \gamma^*} \int_{\gamma > \gamma^*} \frac{\partial}{\partial z} (\kappa N^2) dV. \quad (4)$$

## 6.2 Simulated water mass transformation

638 A 30-day average of the diapycnal velocity  $\tilde{\mathbf{e}} \cdot \mathbf{n}$ , with  $\tilde{\mathbf{e}}$  as defined in equation (3), along  
 639  $-57^\circ$  N, is shown in figure 7a. Notice (red) upwelling close to topography in the bottom  
 640 50-100 m, with (blue) downwelling just above, consistent with the concept of upwelling in  
 641 a boundary layer, with downwelling in the stratified interior above. The upwelling occurs  
 642 due to complex topographic interaction processes in the bottom boundary layer creating  
 643 vertical gradients in stratification and diffusivity such that  $\frac{\partial F_b}{\partial z} < 0$ . In particular, areas  
 644 of unstable stratification near the boundary can reverse the direction of the normal vector  
 645 in equation (3), causing downwards diapycnal velocities that correspond to upwelling in  
 646 buoyancy space. The downwelling above this corresponds to stable stratification and a  
 647 strong decrease in diffusivity with height above bottom.  
 648

649 Above the downwelling, notice that there is largely weak upwelling in the interior; this  
 650 is because the vertical diffusivity is at its background value of  $5 \times 10^{-5} \text{ m}^2 \text{ s}^{-1}$  (unenhanced  
 651 by KPP), and variations in buoyancy flux are solely due to an increase in stratification  
 652 with height. The labelled neutral density contours demonstrate that, at this latitude, densi-  
 653 ties below  $28.16 \text{ kg m}^{-3}$  have intersections with topography, and therefore experience some  
 654 topographically enhanced upwelling. To formalise the importance of the topographic up-  
 655 welling and downwelling of each density class, we now calculate the domain-wide water mass  
 656 transformation, as defined by equation (4).

657 Figure 7b shows water mass transformation averaged over 30 days, using daily average  $\kappa$   
 658 and  $N^2$  fields. There are large contributions from both total upwelling (red) and downwelling  
 659 (blue), which are split by whether they occur within 250 m of topography (boundary, lighter  
 660 colours) or above this (interior, darker colours). It is clear that the majority of both up-  
 661 and downwelling occurs within 250 m of topography, as is expected from figure 7a. The  
 662 net transformation (the sum of upwelling and downwelling) is shown in green dashed, with  
 663 the white shading indicating one standard deviation of the 30-day time series. Despite  
 664 temporal variation (to be discussed later), it is clear that densities greater than  $28.19 \text{ kg}$   
 665  $\text{m}^{-3}$  (corresponding to SPDW and WSDW) upwell, whereas densities between  $28.19$  and  
 666  $28.15 \text{ kg m}^{-3}$  (corresponding to lighter LCDW) downwell. Lighter (interior) density classes  
 667 experience much less transformation, since they intersect less with topography and therefore  
 668 do not experience enhanced diffusivities.

669 The result that the densest waters upwell close to topography, with downwelling oc-  
 670 ccurring above, is, to our knowledge, the first verification of the upwelling/downwelling hy-  
 671 pothesis in a realistic, submesoscale- and internal wave-resolving numerical model with  
 672 online diffusivity parameterization. A recent study by Drake et al. (2022) resolved the  
 673 three-dimensional physical processes leading to diapycnal upwelling, downwelling, and re-  
 674 stratification near topography in a quasi-realistic simulation of a canyon in the Brazil Basin.  
 675 Using an idealised flow with an initially uniform stratification and a realistic topography,  
 676 they showed that an imposed observationally-based exponential diffusivity profile led to  
 677 near-boundary diapycnal upwelling by a three-dimensional eddying submesoscale flow. Our  
 678 work, although in a different region, therefore provides a step forwards in realism by re-  
 679 solving the larger-scale context of the flow (such as realistic large- and mesoscale currents,  
 680 non-uniform stratification, and spatially variable water masses), and by using an online  
 681 diffusivity parameterization to represent the processes that cause mixing. However, we  
 682 necessarily compromise on resolution of the bottom boundary layer, and our results must  
 683 therefore be taken with some caution.

684 By calculating the water mass transformation in the absence of the bottom grid-cell, it  
 685 becomes clear that much of the upwelling of the heaviest density classes is happening there,  
 686 where the insulating boundary condition effectively imposes upwelling. Indeed, several stud-  
 687 ies have calculated water mass transformations globally using climatologies and estimates of  
 688 mixing from various sources, by implicitly ensuring boundary upwelling in the bottom grid  
 689 cell (at any vertical resolution) due to the insulating boundary condition at topography (De  
 690 Lavergne et al., 2016; Ferrari et al., 2016; Mashayek, Salehipour, et al., 2017; Cimoli et al.,  
 691 2019).

692 The grey dashed line in figure 7b shows the net water mass transformation without  
 693 the bottom grid-cell. There remains a small amount of upwelling of the densest waters,  
 694 but downwelling largely dominates. This indicates that we are not sufficiently resolving  
 695 the bottom boundary layer to fully capture the upwelling/downwelling boundary with 25 m  
 696 vertical resolution. This is consistent with one-dimensional idealised boundary layer solu-  
 697 tions for sloping bathymetry with parameters similar to ours, which suggest that diapycnal  
 698 upwelling occurs in a layer of height  $O(50 \text{ m})$  (Holmes & McDougall, 2020). Similarly, the  
 699 quasi-realistic Brazil Basin simulations of Drake et al. (2022) with 6 m vertical resolution  
 700 demonstrated marginally resolved diapycnal upwelling in a bottom boundary layer of  $O(10)$   
 701 m.

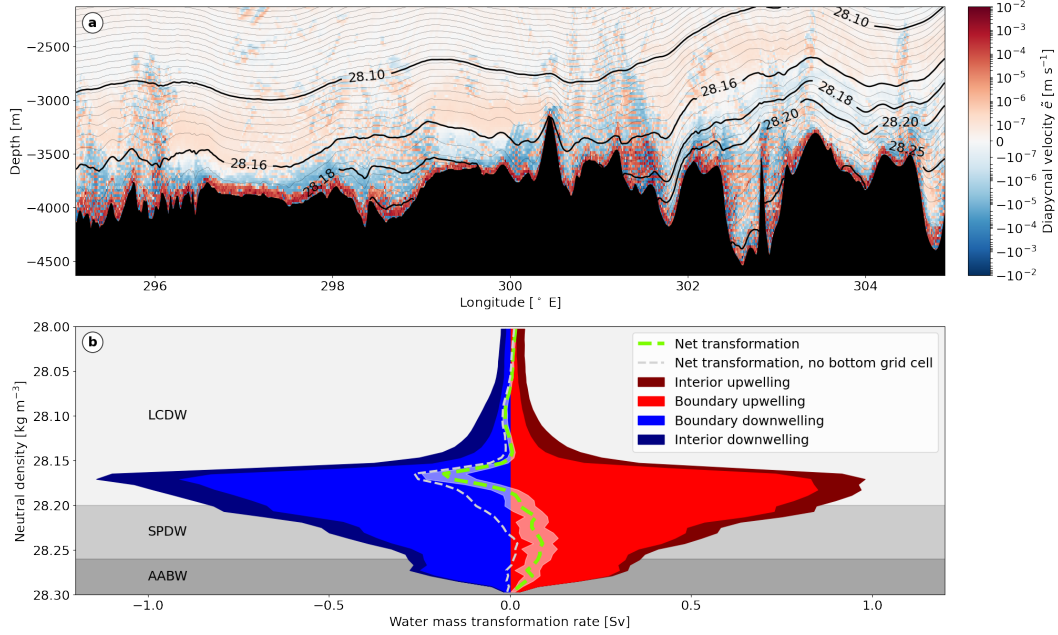


**Figure 7.** (a) 30-day average diapycnal velocity at  $-57^\circ$  N, computed as in equation (3), with neutral density contours. (b) Water mass transformation calculated using equation (4) from daily average density and vertical diffusivity fields, and averaged over 30 days. Interior and boundary contributions are defined by below/above 250 m above bottom. White shading around the net transformation (green dashed) indicates  $\pm 1$  standard deviation of the 30-day time series. The white dashed line shows net transformation when the bottom grid-cell is excluded from the calculation.

702 However, we do find that there is considerable upwelling outside of the bottom grid-cell,  
 703 as is clear from figure 7a, even though it is compensated by downwelling elsewhere. This  
 704 gives us confidence that some realistic processes inducing upwelling of the densest waters  
 705 are represented in this model. Furthermore, the daily averaged fields used to construct  
 706 figure 7b may filter out some of the higher-frequency processes generating upwelling near  
 707 the boundary, which we now investigate further.

### 708 6.3 Temporal variability

709 There is considerable temporal variability of the water mass transformation over the  
 710 30-day time period analysed, and there is therefore sensitivity to the frequency of output  
 711 fields used. In figure 8a, we show the net transformation rate over the final 10 days of the  
 712 simulation, calculated using hourly average fields, daily average fields, and 10-day average  
 713 fields. The corresponding results without the bottom grid-cell are shown as dashed lines of  
 714 the same colour.

715 In each case, upwelling occurs at densities in excess of  $28.19 \text{ kg m}^{-3}$ , with downwelling  
 716 above. This result is thus robust to the frequency of fields used. However, when using  
 717 hourly output (and therefore most accurately representing transformation rate over the 10-  
 718 day period), we find that there is significant upwelling of dense waters even when the bottom  
 719 grid-cell is not included. This suggests that higher-frequency dynamics, such as transient  
 720 boundary overturns, are key in upwelling dense waters in the bottom few hundred metres.

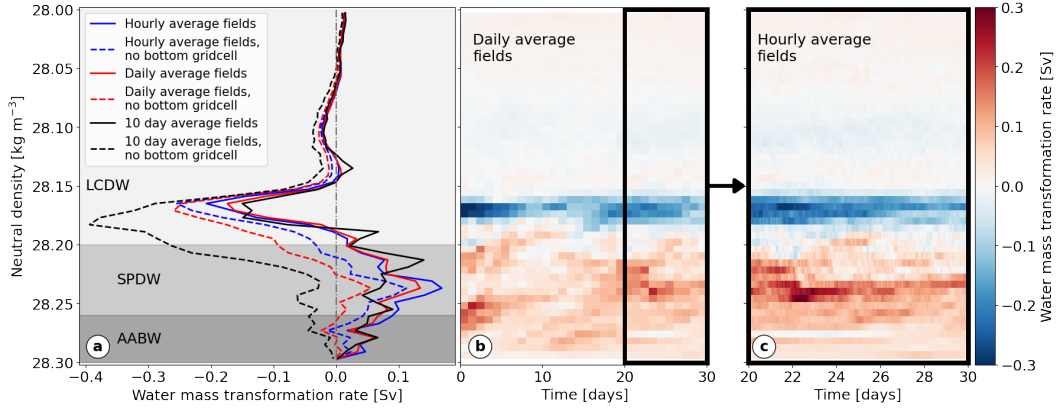


**Figure 8.** (a) Net water mass transformation rate (corresponding to green dashed line in figure 7a) as an average over 10 days, using fields saved at different frequencies. Dashed lines represent transformation rate with bottom grid-cell excluded. (b) Temporal variability of net water mass transformation rate over 30 days using daily average fields. (c) Temporal variability of net water mass transformation rate over 10 days (corresponding to final 10 days of (b)) from hourly output fields.

721 The temporal variability of transformation rate is shown using daily averages over 30  
 722 days in figure 8b, and using hourly averages over the final 10 days in figure 8c. Upwelling  
 723 below the  $28.19 \text{ kg m}^{-3}$  surface, and downwelling above it, are a feature at all times.  
 724 However, there is significant variability in the strength of the upwelling. In particular, a  
 725 high-upwelling event occurs at approximately 22 days, at densities between  $28.22$  and  $28.25$   
 726  $\text{kg m}^{-3}$ . It is very likely that this event corresponds to the high topographic mixing caused  
 727 by the AABW overflow of the West Scotia Ridge demonstrated in figure 6, which occurs  
 728 at this time. This suggests that the transformation of AABW into lighter water classes is  
 729 inherently linked to the dynamics and location of the interface across which it must mix.

730 **7 Sensitivity to model diffusivity**

731 The model-based diffusivity shown in figures 5 and 6, while rooted in sound physi-  
 732 cal concepts (i.e. shear-induced and convective mixing as parameterized through KPP), is  
 733 clearly insufficient. The diffusivity maps show mixing in the close vicinity of the seafloor  
 734 (the last few grid points of the model) and lack much information in the interior, where  
 735 diffusivity is simply set to a low background value. Observational estimates of mixing, how-  
 736 ever, show much more continuous variations in diffusivity as one approaches the seafloor  
 737 (e.g., see Waterhouse et al. (2014)), implying intermittent turbulence in the ocean interior.  
 738 The shortcoming of KPP is expected, as an important contribution of this work is per-  
 739 mitting processes (in the model) that contribute to abyssal mixing. Only further study of  
 740 such processes, which inevitably will require fully resolving them in even higher-resolution  
 741 process-study models, will enhance our physical understanding sufficiently to allow for new  
 742 parameterizations or for their integration into existing frameworks such as the KPP.

743 Since the nature of the simplistic KPP output has a bearing on the upwelling-downwelling  
 744 patterns and their corresponding net water mass transformation rates discussed in figures 7  
 745 and 8, here we also consider an alternate diffusivity parameterization. Figure 9 shows the  
 746 application of a recently developed machine learning (ML) based diffusivity parameteriza-  
 747 tion (Mashayek, Reynard, et al., 2022), which was shown to be rather skillful in the Drake  
 748 Passage region, to an hourly-average ‘snapshot’ from the simulation. The ML diffusivity

map shows a broader distribution of mixing above the seafloor (as opposed to the bottom-focused diffusivity from KPP) which simply reflects the fact that the ML-parameterization was trained on microstructure-based profiles exhibiting a gentler transition from interior to boundary mixing. The patterns emerging from the ML estimates are physically sensible, as they correspond to mixing by overturns along the seafloor (as discussed before and ‘felt’ by the KPP), but also above the seafloor due to breaking of lee waves and shearing of the sharp interfacial dynamics (neither captured by the KPP). Figure 1c confirms the good fit of the ML diffusivity estimate to observations when averaged with reference to height above bottom, and also shows that it gives a lower diffusivity at all heights above bottom than KPP.

The net transformation rates calculated from the KPP-based and ML-based diffusivities have significant differences (figures 9c,d), although the ML parameterisation still captures upwelling of the densest waters (AABW and SPDW). As discussed earlier, the rate at which the interior mixing increases towards the seafloor, and then decreases in the bottom boundary layer to yield a net zero flux at the solid boundary, controls the rate of boundary upwelling and the overlying downwelling. Thus, the smoother transition in mixing from interior to the seafloor in the ML-based estimate results in significantly weaker downwelling and upwelling rates.

Neither the KPP nor the ML representations of mixing are ideal. The former is based on physical principles, but lacks complexity due to our incomplete understanding of the processes that contribute to mixing. The latter is rooted in observations and physical understanding, but can certainly improve significantly as: (i) more observational data become available for training ML models, and (ii) more physical understanding is entrained in training the ML algorithms. Nevertheless, together, the two estimates (figures 9a,b) provide a bound on the uncertainty involved in estimates of mixing in even a realistic model of such unprecedented high resolution as ours. Thus, figure 9 helps us make two important points. First, it highlights the need for development of better mixing parameterizations in order to confidently determine the mixing of deep water masses and their net upwelling rates. Second, while at early stages, ML-based estimates, once connected with physical understanding, can prove a valuable tool for constraining deep-ocean mixing and meridional overturning.

The differences between the KPP and ML parameterizations do not impact the main messages of this paper, which are that (i) the dynamical interaction of water mass interfaces with topography is itself a source of instability and mixing in the deep ocean, (ii) the presence of these interfaces in the abyssal ocean can modify the nature of other topographic processes such as lee waves, and (iii) that small-scale, temporally variable, topographic interaction processes within a few hundred metres of the seafloor result in upwelling of AABW.

## 8 Discussion

We have used a high-resolution, realistic simulation to investigate the processes governing turbulent diapycnal mixing and water mass transformation of dense AABW as it flows through the Drake Passage. In addition to confirming the importance of known contributors to regional abyssal mixing (such as lee waves), we have also identified for the first time the dynamical role of highly stratified water mass interfaces in generating turbulence in the deep ocean.

Observational studies have previously reported the presence of highly stratified interfaces between deep water masses in several locations globally, including the Drake Passage (Sievers & Nowlin, 1984; Meredith et al., 2013; Reid et al., 1977). We have identified these stratified interfaces in further observations in the area as well as in our simulation, where the interfaces correspond to boundaries between deep CDW varieties (LCDW and SPDW) and the regional AABW (WSDW). The interfaces exhibit strong variability in time and space, and are often horizontally tilted by topography and mesoscale eddies.

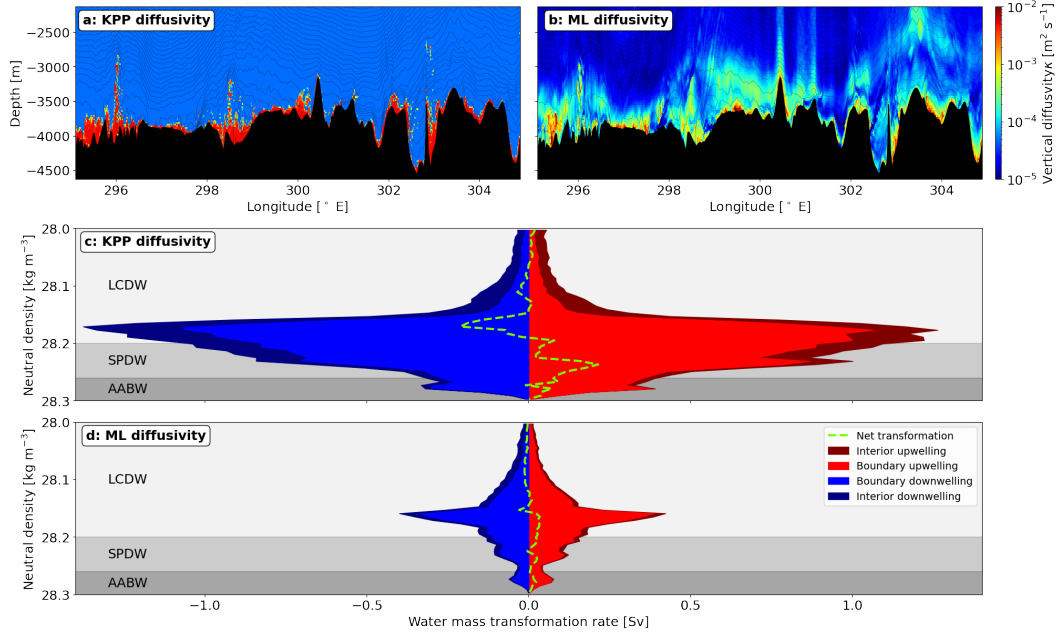


**Figure 9.** (a) Hourly average online KPP vertical diffusivity on day 94 (equivalent to figure 5b). (b) Offline diffusivity calculated from simulation fields using algorithm learnt from global observational turbulence data (Mashayek, Reynard, et al., 2022). (c) Water mass transformation calculated over the full domain from KPP diffusivity for an hourly average on day 94 (c.f. figure 7b). (d) As in (c), calculated using machine learning-based diffusivity shown in (b).

799 We conclude, based on our simulation, that these interfaces may play an important role  
 800 in the upwelling of AABW by boosting topographic mixing processes in the deep ocean.  
 801 We have identified several dynamical impacts of the interfaces: (i) creation of vertical shear  
 802 in the deep ocean by geostrophic adjustment of tilted interfaces; (ii) interaction of strong  
 803 horizontal buoyancy gradients with topography to induce convective overturning; and (iii)  
 804 impact on the generation, propagation and breaking of lee waves.

805 The evidence presented here for the existence of such water mass interfaces at depth  
 806 and their impact on abyssal dynamics raises important questions that will require further  
 807 study. We conjectured that the maintenance of the interfaces' high stratification may be  
 808 linked to frontogenetic processes in the deep ocean, but this should be examined in detail.  
 809 Further, the occurrence and relevance of these interfaces over the Southern Ocean and  
 810 globally should be investigated. Unfortunately, even state-of-the-art resolution global ocean  
 811 models, such as the 1/48° LLC4320 global simulation (Rocha et al., 2016; Su et al., 2018) do  
 812 not have sufficient vertical resolution at depth to adequately capture water mass interfaces.  
 813 We found no evidence of stratified interfaces in the LLC4320 model in the Drake Passage,  
 814 likely owing to the resolution at 4000 m depth being  $\sim 200$  m. If, as suggested here, water  
 815 mass interfaces impact topographic turbulence and lee wave generation and breaking, this  
 816 effect would be extremely challenging to account for in mixing parameterizations embedded  
 817 in coarse models.

818 Using an online parameterization of diffusivity, we were able to link topographic mixing  
 819 processes to quantification of water mass transformation in the Drake Passage. Waters  
 820 denser than 28.19, corresponding to SPDW and WSDW, were found to experience net  
 821 upwelling, whereas the LCDW above experiences net downwelling. We proposed that an

episode of strong AABW upwelling in the simulation was elicited by an overflow of dense AABW over a large topographic ridge system, linking the dynamics of the interface (both in terms of its location and effect on mixing) to cross-interface upwelling.

Our work constitutes a first realistic demonstration of how resolved submesoscale and internal wave-driven mixing processes induce boundary upwelling of deep waters, as predicted by the recently put forward upwelling/downwelling paradigm (De Lavergne et al., 2016; Ferrari et al., 2016; McDougall & Ferrari, 2017). However, still higher vertical resolution on the order of metres is needed to satisfactorily resolve upwelling in the bottom boundary layer (Drake et al., 2022). We also demonstrated the need for hourly temporal resolution to capture the water mass transformation correctly, especially outside of the bottom grid-cell. This implies that the processes driving diapycnal upwelling are highly temporally variable. Given the demonstrated importance of realistic topography, stratification and flow, and of metre-scale boundary layer dynamics in quantifying AABW transformation, unprecedented model resolution would be required to fully capture the wide range of scales of this problem.

Through comparison of our online KPP diffusivity parameterization and resulting water mass transformation with results based on a recent machine learning estimate of diffusivity, we showed that considerable uncertainties remain in the vertical diffusivity representation of abyssal processes. This brings about a limited ability of even high resolution regional models to adequately constrain the transformation rate of abyssal waters. Knowledge of this transformation rate is essential to our understanding of the ocean’s overturning circulation and oceanic transport and storage of climatically important tracers. Resolving these outstanding questions in the future will require a multifaceted approach of higher-resolution model process studies, innovative applications of machine learning, and more extensive abyssal observations in different turbulent regimes.

## Appendix A Drake Passage Model Setup

The simulation is performed at  $0.01^\circ$  horizontal resolution using the MITgcm (Marshall et al., 1997) in hydrostatic configuration. There are 225 vertical levels, with resolution  $dz$  varying smoothly from  $dz = 10$  m at the surface to  $dz = 25$  m at 600 m depth,  $dz = 25$  m between 600 and 4,555 m depth, and varying smoothly from  $dz = 25$  m to 62 m at the maximum depth of 5,660 m. Partial cells are used at topography with a minimum height of 10 m. The timestep is 24 s.

The simulation is forced at the open boundaries by the OCCA state estimate (Forget, 2010) as described in the main text. The nonlinear free surface is forced by near surface air temperature, wind speed, precipitation, humidity, long and short wave radiation from the ECMWF ERA-Interim reanalysis product (Simmons et al., 2006). The model does not include tides. The topography is interpolated from the Smith and Sandwell (1997) v15.1 1 min bathymetric product, and contains some areas of multibeam topography alongside satellite altimetry derived estimates of topography.

The bottom boundary condition is no-slip, which is implemented in the MITgcm through an extra drag term in the bottom grid cell. In addition, we use a quadratic drag with a coefficient of  $2.5 \times 10^{-3}$  to represent unresolved small scale topography; see MITgcm documentation (<https://mitgcm.readthedocs.io>) and Legg et al. (2006) for details.

Horizontal viscosity is implemented with the biharmonic Leith scheme with a coefficient of 2 (Fox-Kemper & Menemenlis, 2008; Leith, 1996). Background vertical viscosity and diffusivity of temperature and salinity are set at  $5 \times 10^{-5} \text{ m}^2 \text{ s}^{-1}$ . The KPP parameterization (Large et al., 1994) enhances vertical diffusivity (and viscosity) in the interior according to criteria for shear and convective instability. The critical Richardson number for onset of shear instability is  $1/3$ .

## Open Research

All software and processed data required to enable the reader to reproduce our results are published via Zenodo at [doi.org/10.5281/zenodo.7410908](https://doi.org/10.5281/zenodo.7410908) (Baker et al., 2022). The MIT-gcm (Marshall et al., 1997) is documented at <https://mitgcm.readthedocs.io> and available at [doi.org/10.5281/zenodo.1409237](https://doi.org/10.5281/zenodo.1409237) (Campin et al., 2019).

Observational CTD data along the SR1b section, collected by the ACCLAIM project and used in figures 1e and 2, and CTD and ADCP data collected by the DIMES project used in figure 4 are available from [bodc.ac.uk/data](https://bodc.ac.uk/data).

## Conflict of Interest Statement

The authors have no conflicts of interest to declare.

## Acknowledgments

L.B. was supported by the Centre for Doctoral Training in Mathematics of Planet Earth, UK EPSRC funded (Grant EP/L016613/1), and A.M. acknowledges funding from the NERC IRF fellowship grant NE/P018319/1. Computational resources provided by the Imperial College London Research Computing Service are gratefully acknowledged (<https://doi.org/10.14469/hpc/2232>).

## References

- Alford, M. H., Girton, J. B., Voet, G., Carter, G. S., Mickett, J. B., & Klymak, J. M. (2013). Turbulent mixing and hydraulic control of abyssal water in the Samoan Passage. *Geophys. Res. Lett.*, *40*(17), 4668–4674. doi: 10.1002/grl.50684
- Armi, L., & Mayr, G. J. (2015). Virtual and real topography for flows across mountain ranges. *J. Appl. Meteorol. Climatol.*, *54*(4), 723–731. doi: 10.1175/JAMC-D-14-0231.1
- Baines, P. G. (1995). *Topographic effects in stratified flows*. Cambridge: Cambridge University Press.
- Baker, L. E., & Mashayek, A. (2021). Surface reflection of bottom generated oceanic lee waves. *J. Fluid Mech.*, *924*(A17), 1–42. doi: 10.1017/jfm.2021.627
- Baker, L. E., & Mashayek, A. (2022). The Impact of Representations of Realistic Topography on Parameterized Oceanic Lee Wave Energy Flux. *J. Geophys. Res. Ocean.*, 1–34. doi: 10.1029/2022JC018995
- Baker, L. E., Mashayek, A., & Naveira-Garabato, A. C. (2022). *Enhanced upwelling of Antarctic Bottom Water by topographic interaction of water mass interfaces [Software and Dataset]*. Zenodo. doi: 10.5281/zenodo.7410908
- Callies, J. (2018). Restratification of abyssal mixing layers by submesoscale baroclinic eddies. *J. Phys. Oceanogr.*, *48*(9), 1995–2010. doi: 10.1175/JPO-D-18-0082.1
- Campin, J.-M., Heimbach, P., Losch, M., Forget, G., Edhill, A., Adcroft, A., ... Dussin, R. (2019). *MITgcm/MITgcm: checkpoint67g [Software]*. Zenodo. doi: 10.5281/zenodo.1409237
- Caulfield, C. (2021). Layering, Instabilities, and Mixing in Turbulent Stratified Flows. *Annu. Rev. Fluid Mech.*, *53*(1). doi: 10.1146/annurev-fluid-042320-100458
- Cimoli, L., Caulfield, C. c. P., Johnson, H. L., Marshall, D. P., Mashayek, A., Naveira Garabato, A. C., & Vic, C. (2019). Sensitivity of Deep Ocean Mixing to Local Internal Tide Breaking and Mixing Efficiency. *Geophys. Res. Lett.*, *46*(24), 14622–14633. doi: 10.1029/2019GL085056
- Cusack, J. M., Naveira Garabato, A. C., Smeed, D. A., & Girton, J. B. (2017). Observation of a Large Lee Wave in the Drake Passage. *J. Phys. Oceanogr.*, *47*(4), 793–810. doi: 10.1175/JPO-D-16-0153.1

- 918 De Lavergne, C., Madec, G., Le Sommer, J., Nurser, A. J., & Naveira Garabato, A. C.  
919 (2016). On the consumption of Antarctic Bottom Water in the abyssal ocean. *J.*  
920 *Phys. Oceanogr.*, *46*(2), 635–661. doi: 10.1175/JPO-D-14-0201.1
- 921 Drake, H. F., Ferrari, R., & Callies, J. (2020). Abyssal circulation driven by near-boundary  
922 mixing: Water mass transformations and interior stratification. *J. Phys. Oceanogr.*,  
923 *50*(8), 2203–2226. doi: 10.1175/JPO-D-19-0313.1
- 924 Drake, H. F., Ruan, X., Callies, J., Ogden, K., Thurnherr, A. M., & Ferrari, R. (2022).  
925 Dynamics of eddying abyssal mixing layers over sloping rough topography. *J. Phys.*  
926 *Oceanogr.*. doi: 10.1175/jpo-d-22-0009.1
- 927 Durran, D. R. (1986). Another Look at Downslope Windstorms. Part I: The Development of  
928 Analogs to Supercritical Flow in an Infinitely Deep, Continuously Stratified Fluid. *J.*  
929 *Atmos. Sci.*, *43*(21), 2527–2543. doi: 10.1175/1520-0469(1986)043<2527:ALADWP>2  
930 .0.CO;2
- 931 Emile-Geay, J., & Madec, G. (2009). Geothermal heating, diapycnal mixing and the abyssal  
932 circulation. *Ocean Sci.*, *5*(2), 203–217. doi: 10.5194/os-5-203-2009
- 933 Ferrari, R., Mashayek, A., McDougall, T. J., Nikurashin, M., & Campin, J. M. (2016).  
934 Turning ocean mixing upside down. *J. Phys. Oceanogr.*, *46*(7), 2239–2261. doi: 10  
935 .1175/JPO-D-15-0244.1
- 936 Forget, G. (2010, jun). Mapping ocean observations in a dynamical framework: A 2004-06  
937 ocean atlas. *J. Phys. Oceanogr.*, *40*(6), 1201–1221. doi: 10.1175/2009JPO4043.1
- 938 Fox-Kemper, B., & Menemenlis, D. (2008). Can large eddy simulation techniques improve  
939 mesoscale rich ocean models? *Geophys. Monogr. Ser.*, *177*, 319–337. doi: 10.1029/  
940 177GM19
- 941 Garrett, C., MacCready, P., & Rhines, P. (1993). Boundary mixing and arrested Ekman  
942 layers: rotating stratified flow near a sloping boundary. *Annu. Rev. Fluid Mech.*. doi:  
943 10.1146/annurev.fluid.25.1.291
- 944 Gregg, M., D’Asaro, E., Riley, J., & Kunze, E. (2018). Mixing Efficiency in the Ocean.  
945 *Ann. Rev. Mar. Sci.*, *10*(1), 443–473. doi: 10.1146/annurev-marine-121916-063643
- 946 Gutierrez-Villanueva, M. O., Chereskin, T. K., Sprintall, J., & Goff, J. A. (2022). Turbulent  
947 Mixing and Lee-Wave Radiation in Drake Passage: Sensitivity to Topography. *J.*  
948 *Geophys. Res. Ocean.*, *127*(5), 1–25. doi: 10.1029/2021jc018103
- 949 Holmes, R. M., & McDougall, T. J. (2020). Diapycnal transport near a sloping bottom  
950 boundary. *J. Phys. Oceanogr.*, *50*(11), 3253–3266. doi: 10.1175/JPO-D-20-0066.1
- 951 Hoskins, B. J. (1982). The mathematical theory of frontogenesis. *Annu. Rev. fluid Mech.*  
952 *Vol. 14*, 131–151. doi: 10.1146/annurev.fl.14.010182.001023
- 953 Howard, L. (1961). Note on a paper of John W. Miles. *J. Fluid Mech.*, *10*(4), 509–512. doi:  
954 10.1017/S0022112061000317
- 955 Jackett, D. R., & McDougall, T. J. (1997). A neutral density variable for the world’s  
956 oceans. *J. Phys. Oceanogr.*, *27*(2), 237–263. doi: 10.1175/1520-0485(1997)027<0237:  
957 ANDVFT>2.0.CO;2
- 958 Jagannathan, A., Winters, K. B., & Armi, L. (2020). The effect of a strong density  
959 step on blocked stratified flow over topography. *J. Fluid Mech.*, *889*. doi: 10.1017/  
960 jfm.2020.87
- 961 Johnson, G. C. (2008). Quantifying Antarctic Bottom Water and North Atlantic Deep  
962 Water volumes. *J. Geophys. Res. Ocean.*, *113*(5), 1–13. doi: 10.1029/2007JC004477
- 963 Klemp, J. B., & Lilly, D. K. (1975). The dynamics of wave-induced downslope winds. *J.*  
964 *Atmos. Sci.*, *32*. doi: 10.1175/1520-0469(1975)032<0320:TADOWID>2.0.CO;2
- 965 Klymak, J. M. (2018). Nonpropagating form drag and turbulence due to stratified flow  
966 over large-scale Abyssal Hill Topography. *J. Phys. Oceanogr.*, *48*(10), 2383–2395. doi:  
967 10.1175/JPO-D-17-0225.1
- 968 Klymak, J. M., Balwada, D., Garabato, A. N., & Abernathey, R. (2021). Parameterizing  
969 Nonpropagating Form Drag over Rough Bathymetry. *J. Phys. Oceanogr.*, *51*(5), 1489–  
970 1501. doi: 10.1175/jpo-d-20-0112.1
- 971 Kunze, E., & Lien, R.-C. (2019). Energy Sinks for Lee Waves in Shear Flow. *J. Phys.*  
972 *Oceanogr.*, 2851–2865. doi: 10.1175/jpo-d-19-0052.1

- 973 Large, W. G., McWilliams, J. C., & Doney, S. C. (1994). Oceanic vertical mixing: A review  
974 and a model with a nonlocal boundary layer parameterization. *Rev. Geophys.*, *32*(4),  
975 363–403. doi: 10.1029/94RG01872
- 976 Ledwell, J. R., Montgomery, E. T., Polzin, K. L., St. Laurent, L. C., Schmitt, R. W., &  
977 Toole, J. M. (2000). Evidence for enhanced mixing over rough topography in the  
978 abyssal ocean. *Nature*, *403*, 179–182. doi: 10.1038/35003164
- 979 Legg, S. (2021). Mixing by Oceanic Lee Waves. *Annu. Rev. Fluid Mech.*, *53*, 173–201. doi:  
980 10.1146/annurev-fluid-051220-043904
- 981 Legg, S., Hallberg, R. W., & Girton, J. B. (2006). Comparison of entrainment in overflows  
982 simulated by z-coordinate, isopycnal and non-hydrostatic models. *Ocean Model.*, *11*(1-  
983 2), 69–97. doi: 10.1016/j.ocemod.2004.11.006
- 984 Legg, S., & Klymak, J. (2008). Internal Hydraulic Jumps and Overturning Generated  
985 by Tidal Flow over a Tall Steep Ridge. *J. Phys. Oceanogr.*, *38*, 1949–1964. doi:  
986 10.1175/2008JPO3777.1
- 987 Leith, C. E. (1996). Stochastic models of chaotic systems. *Phys. D Nonlinear Phenom.*,  
988 *98*(2-4), 481–491. doi: 10.1016/0167-2789(96)00107-8
- 989 Liu, M., & Tanhua, T. (2021). Water masses in the Atlantic Ocean: Characteristics and  
990 distributions. *Ocean Sci.*, *17*(2), 463–486. doi: 10.5194/os-17-463-2021
- 991 Lumpkin, R., & Speer, K. (2007). Global ocean meridional overturning. *J. Phys. Oceanogr.*,  
992 *37*(10), 2550–2562. doi: 10.1175/JPO3130.1
- 993 MacCready, P., & Rhines, P. B. (1991). Buoyant inhibition of ekman transport on a slope  
994 and its effect on stratified spin-up. *J. Fluid Mech.*, *223*, 631–661. doi: 10.1017/  
995 S0022112091001581
- 996 Mackay, N., Ledwell, J. R., Messias, M. J., Naveira Garabato, A. C., Brearley, J. A., Meijers,  
997 A. J., ... Watson, A. J. (2018, apr). Diapycnal Mixing in the Southern Ocean  
998 Diagnosed Using the DIMES Tracer and Realistic Velocity Fields. *J. Geophys. Res.*  
999 *Ocean.*, *123*(4), 2615–2634. doi: 10.1002/2017JC013536
- 1000 MacKinnon, J., Laurent, L. S., & Garabato, A. C. N. (2013). Diapycnal Mixing Processes  
1001 in the Ocean Interior. In *Ocean circ. clim. a 21st century perspect.* (Vol. 103, pp.  
1002 159–183). Retrieved from [http://www.sciencedirect.com/science/article/pii/  
1003 B9780123918512000076](http://www.sciencedirect.com/science/article/pii/B9780123918512000076) doi: <https://doi.org/10.1016/B978-0-12-391851-2.00007-6>
- 1004 MacKinnon, J. A., Zhao, Z., Whalen, C. B., Griffies, S. M., Sun, O. M., Barna, A., ...  
1005 Norton, N. J. (2017). Climate Process Team on Internal Wave–Driven Ocean Mixing.  
1006 *Bull. Am. Meteorol. Soc.*, *98*(11), 2429–2454. doi: 10.1175/bams-d-16-0030.1
- 1007 Marshall, J., Adcroft, A., Hill, C., Perelman, L., & Heisey, C. (1997). A finite-volume,  
1008 incompressible navier stokes model for, studies of the ocean on parallel computers. *J.*  
1009 *Geophys. Res. C Ocean.*, *102*(C3), 5753–5766. doi: 10.1029/96JC02775
- 1010 Marshall, J., & Speer, K. (2012). Closure of the meridional overturning circulation through  
1011 Southern Ocean upwelling. *Nat. Geosci.*, *5*(3), 171–180. doi: 10.1038/ngeo1391
- 1012 Mashayek, A., Baker, L. E., Cael, B. B., & Caulfield, C. P. (2022). A Marginal Stability  
1013 Paradigm for Shear-Induced Diapycnal Turbulent Mixing in the Ocean. *Geophys. Res.*  
1014 *Lett.*, *49*(2), 1–11. doi: 10.1029/2021GL095715
- 1015 Mashayek, A., Caulfield, C. P., & Alford, M. H. (2021). Goldilocks mixing in oceanic shear-  
1016 induced turbulent overturns. *J. Fluid Mech.*, *928*, 1–32. doi: 10.1017/jfm.2021.740
- 1017 Mashayek, A., Ferrari, R., Merrifield, S., Ledwell, J. R., St Laurent, L., & Garabato, A. N.  
1018 (2017). Topographic enhancement of vertical turbulent mixing in the Southern Ocean.  
1019 *Nat. Commun.*, *8*, 1–12. doi: 10.1038/ncomms14197
- 1020 Mashayek, A., Ferrari, R., Vettoretti, G., & Peltier, W. R. (2013). The role of the geothermal  
1021 heat flux in driving the abyssal ocean circulation. *Geophys. Res. Lett.*, *40*(12), 3144–  
1022 3149. doi: 10.1002/grl.50640
- 1023 Mashayek, A., Reynard, N., Zhai, F., Srinivasan, K., Jelley, A., Naveira Garabato, A., &  
1024 Caulfield, C. P. (2022). Deep Ocean Learning of Small Scale Turbulence. *Geophys.*  
1025 *Res. Lett.*, *49*(15), 1–9. doi: 10.1029/2022GL098039
- 1026 Mashayek, A., Salehipour, H., Bouffard, D., Caulfield, C. P., Ferrari, R., Nikurashin, M., ...  
1027 Caulfield, C. P. (2017). Efficiency of turbulent mixing in the abyssal ocean circulation.

- 1028 *Geophys. Res. Lett.*, *44*(12), 6296–6306. doi: 10.1002/2016gl072452
- 1029 McDougall, T. J., & Ferrari, R. (2017). Abyssal upwelling and downwelling driven by near-  
1030 boundary mixing. *J. Phys. Oceanogr.*, *47*(2), 261–283. doi: 10.1175/JPO-D-16-0082.1
- 1031 McWilliams, J. C. (2021). Oceanic Frontogenesis. *Ann. Rev. Mar. Sci.*, *13*, 227–253. doi:  
1032 10.1146/annurev-marine-032320-120725
- 1033 Meredith, M. P., Brown, P. J., Naveira Garabato, A. C., Jullion, L., Venables, H. J.,  
1034 & Messias, M. J. (2013). Dense bottom layers in the Scotia Sea, Southern Ocean:  
1035 Creation, lifespan, and destruction. *Geophys. Res. Lett.*, *40*(5), 933–936. doi: 10.1002/  
1036 grl.50260
- 1037 Meredith, M. P., & Naveira Garabato, A. C. (2021). *Ocean Mixing*. Elsevier. doi: 10.1016/  
1038 C2019-0-03674-6
- 1039 Merrifield, S. T., Laurent, L. S., Owens, B., Thurnherr, A. M., & Toole, J. M. (2016).  
1040 Enhanced diapycnal diffusivity in intrusive regions of the Drake passage. *J. Phys.*  
1041 *Oceanogr.*, *46*(4), 1309–1321. doi: 10.1175/JPO-D-15-0068.1
- 1042 Miles, J. W. (1961). On the stability of heterogeneous shear flows. *J. Fluid Mech.*, *10*(4),  
1043 496–508. doi: 10.1017/S0022112061000305
- 1044 Moum, J. N. (2021). Variations in Ocean Mixing from Seconds to Years. *Ann. Rev. Mar.*  
1045 *Sci.*, *13*, 201–226. doi: 10.1146/annurev-marine-031920-122846
- 1046 Munk, W., & Wunsch, C. (1998). Abyssal recipes II Energetics of tidal and wind mixing.  
1047 *Deep. Res.*, *1*(45), 1977–2010. doi: 10.1016/S0967-0637(98)00070-3
- 1048 Naveira Garabato, A., Polzin, K., King, B., Heywood, K., & Visbeck, M. (2004). Widespread  
1049 Intense Turbulent Mixing in the Southern Ocean. *Science (80-. )*, *303*(January), 210–  
1050 213. doi: 10.1126/science.1090929
- 1051 Naveira Garabato, A. C., Frajka-Williams, E. E., Spingys, C. P., Legg, S., Polzin, K. L.,  
1052 Forryan, A., ... Meredith, M. P. (2019). Rapid mixing and exchange of deep-ocean  
1053 waters in an abyssal boundary current. *Proc. Natl. Acad. Sci. U. S. A.*, *116*(27),  
1054 13233–13238. doi: 10.1073/pnas.1904087116
- 1055 Naveira Garabato, A. C., Heywood, K. J., & Stevens, D. P. (2002). Modification and  
1056 pathways of Southern Ocean Deep Waters in the Scotia Sea. *Deep. Res. I*, *49*, 681–  
1057 705. doi: 10.1016/S0967-0637(01)00071-1
- 1058 Naveira Garabato, A. C., McDonagh, E. L., Stevens, D. P., Heywood, K. J., & Sanders,  
1059 R. J. (2002). On the export of Antarctic Bottom Water from the Weddell Sea. *Deep.*  
1060 *Res. Part II Top. Stud. Oceanogr.*, *49*(21), 4715–4742. doi: 10.1016/S0967-0645(02)  
1061 00156-X
- 1062 Naveira Garabato, A. C., Williams, A. P., & Bacon, S. (2014). The three-dimensional  
1063 overturning circulation of the Southern Ocean during the WOCE era. *Prog. Oceanogr.*,  
1064 *120*, 41–78. doi: 10.1016/j.pocean.2013.07.018
- 1065 Nikurashin, M., & Ferrari, R. (2010). Radiation and Dissipation of Internal Waves Generated  
1066 by Geostrophic Motions Impinging on Small-Scale Topography: Application to the  
1067 Southern Ocean. *J. Phys. Oceanogr.*, *40*(9), 2025–2042. doi: 10.1175/2010jpo4315.1
- 1068 Nikurashin, M., & Ferrari, R. (2011). Global energy conversion rate from geostrophic  
1069 flows into internal lee waves in the deep ocean. *Geophys. Res. Lett.*, *38*(8), 1–6. doi:  
1070 10.1029/2011GL046576
- 1071 Osborn, T. R. (1980). *Estimates of the Local Rate of Vertical Diffusion from Dissipation*  
1072 *Measurements* (Vol. 10) (No. 1). doi: 10.1175/1520-0485(1980)010<0083:eotlro>2.0.co;  
1073 2
- 1074 Peltier, W., & Clark, T. (1979). The Evolution and Stability of Finite-Amplitude Mountain  
1075 Waves. Part II: Surface Wave Drag and Severe Downslope Windstorms. *J. Atmos.*  
1076 *Sci.*, *36*(9), 1498–1529. doi: 10.1175/1520-0469(1980)037<2119:COEASO>2.0.CO;2
- 1077 Polzin, K. L., & McDougall, T. J. (2022). Mixing at the ocean’s bottom boundary. In  
1078 M. P. Meredith & A. C. Naveira Garabato (Eds.), *Ocean mix.* (pp. 145–180). Elsevier.  
1079 doi: 10.1016/b978-0-12-821512-8.00014-1
- 1080 Polzin, K. L., Toole, J. M., Ledwell, J. R., & Schmitt, R. W. (1997). Spatial variability  
1081 of turbulent mixing in the abyssal ocean. *Science (80-. )*, *276*(5309), 93–96. doi:  
1082 10.1126/science.276.5309.93

- 1083 Purkey, S. G., Smethie, W. M., Gebbie, G., Gordon, A. L., Sonnerup, R. E., Warner,  
1084 M. J., & Bullister, J. L. (2018). A synoptic view of the ventilation and circulation of  
1085 antarctic bottom water from chlorofluorocarbons and natural tracers. *Ann. Rev. Mar.*  
1086 *Sci.*, *10*(September), 503–527. doi: 10.1146/annurev-marine-121916-063414
- 1087 Rae, J. W., Burke, A., Robinson, L. F., Adkins, J. F., Chen, T., Cole, C., ... Taylor,  
1088 B. J. (2018). CO<sub>2</sub> storage and release in the deep Southern Ocean on millennial to  
1089 centennial timescales. *Nature*, *562*(7728), 569–573. doi: 10.1038/s41586-018-0614-0
- 1090 Reid, J., Nowlin, W., & Patzert, W. (1977). On the Characteristics and Circulation of  
1091 the Southwestern Atlantic Ocean. *J. Phys. Oceanogr.*, *7*, 62–91. doi: 10.1175/1520-  
1092 -0485(1977)007<0062:OTCACO>2.0.CO;2
- 1093 Rocha, C. B., Chereskin, T. K., Gille, S. T., & Menemenlis, D. (2016). Mesoscale to  
1094 submesoscale wavenumber spectra in Drake Passage. *J. Phys. Oceanogr.*, *46*(2), 601–  
1095 620. doi: 10.1175/JPO-D-15-0087.1
- 1096 Ruan, X., Thompson, A. F., & Taylor, J. R. (2019). The evolution and arrest of a turbulent  
1097 stratified oceanic bottom boundary layer over a slope: Downslope regime. *J. Phys.*  
1098 *Oceanogr.*, *49*(2), 469–487. doi: 10.1175/JPO-D-18-0079.1
- 1099 Ruan, X., Thompson, A. F., & Taylor, J. R. (2021). The evolution and arrest of a tur-  
1100 bulent stratified oceanic bottom boundary layer over a slope: Upslope regime and pv  
1101 dynamics. *J. Phys. Oceanogr.*, *51*(4), 1077–1089. doi: 10.1175/JPO-D-20-0168.1
- 1102 Sarkar, S., & Scotti, A. (2017). From Topographic Internal Gravity Waves to Turbulence.  
1103 *Annu. Rev. Fluid Mech.*, *49*(1), 195–220. doi: 10.1146/annurev-fluid-010816-060013
- 1104 Scott, R. B., Goff, J. A., Naveira Garabato, A. C., & Nurser, A. J. G. (2011). Global rate  
1105 and spectral characteristics of internal gravity wave generation by geostrophic flow  
1106 over topography. *J. Geophys. Res.*, *116*(C09029), 1–14. doi: 10.1029/2011JC007005
- 1107 Sheen, K. L., Brearley, J. A., Naveira Garabato, A. C., Smeed, D. A., Waterman, S., Ledwell,  
1108 J. R., ... Watson, A. J. (2013). Rates and mechanisms of turbulent dissipation and  
1109 mixing in the Southern Ocean: Results from the Diapycnal and Isopycnal Mixing  
1110 Experiment in the Southern Ocean (DIMES). *J. Geophys. Res. Ocean.*, *118*(6), 2774–  
1111 2792. doi: 10.1002/jgrc.20217
- 1112 Sheridan, P. F., & Vosper, S. B. (2006). A flow regime diagram for forecasting lee  
1113 waves, rotors and downslope winds. *Meteorol. Appl.*, *13*(2), 179–195. doi: 10.1017/  
1114 S1350482706002088
- 1115 Siegelman, L., Klein, P., Rivière, P., Thompson, A. F., Torres, H. S., Flexas, M., & Men-  
1116 emenlis, D. (2020). Enhanced upward heat transport at deep submesoscale ocean  
1117 fronts. *Nat. Geosci.*, *13*(1), 50–55. doi: 10.1038/s41561-019-0489-1
- 1118 Sievers, H. A., & Nowlin, W. D. (1984). The stratification and water masses at Drake  
1119 Passage. *J. Geophys. Res.*, *89*(C6), 10489. doi: 10.1029/jc089ic06p10489
- 1120 Simmons, A., Uppala, S., Dee, D., & Kobayashi, S. (2006). ERA-Interim: New ECMWF  
1121 reanalysis products from 1989 onwards. *ECMWF Newsl.*, *110*, 25–35. doi: 10.21957/  
1122 pocnex23c6
- 1123 Skinner, L., Fallon, S., Waelbroeck, C., Michel, E., & Barker, S. (2010). Ventilation of the  
1124 Deep Southern Ocean and Deglacial CO<sub>2</sub> Rise. *Science (80-. )*, *328*, 1147–1152. doi:  
1125 10.1126/science.1183627
- 1126 Smith, W. H., & Sandwell, D. T. (1997). Global sea floor topography from satellite altimetry  
1127 and ship depth soundings. *Science (80-. )*, *277*(5334), 1956–1962. doi: 10.1126/  
1128 science.277.5334.1956
- 1129 Smyth, W. D. (2020). Marginal instability and the efficiency of ocean mixing. *J. Phys.*  
1130 *Oceanogr.*, *50*(8), 2141–2150. doi: 10.1175/JPO-D-20-0083.1
- 1131 Solodoch, A., Stewart, A. L., Hogg, A. M. C., Morrison, A. K., Kiss, A. E., Thompson,  
1132 A. F., ... Cimoli, L. (2022). How Does Antarctic Bottom Water Cross the Southern  
1133 Ocean? *Geophys. Res. Lett.*, *49*(7), 1–11. doi: 10.1029/2021GL097211
- 1134 Spingys, C. P., Naveira Garabato, A. C., Legg, S., Polzin, K. L., Abrahamsen, E. P.,  
1135 Buckingham, C. E., ... Frajka-Williams, E. E. (2021, jan). Mixing and Transformation  
1136 in a Deep Western Boundary Current: A Case Study. *J. Phys. Oceanogr.*, *51*(4),  
1137 1205–1222. doi: 10.1175/jpo-d-20-0132.1

- 1138 Srinivasan, K., McWilliams, J. C., Molemaker, M. J., & Barkan, R. (2019). Submesoscale  
1139 Vortical Wakes in the Lee of Topography. *J. Phys. Oceanogr.*, *49*(7), 1949–1971. doi:  
1140 10.1175/jpo-d-18-0042.1
- 1141 St. Laurent, L., Naveira Garabato, A. C., Ledwell, J. R., Thurnherr, A. M., Toole, J. M.,  
1142 & Watson, A. J. (2012). Turbulence and diapycnal mixing in drake passage. *J. Phys.*  
1143 *Oceanogr.*, *42*(12), 2143–2152. doi: 10.1175/JPO-D-12-027.1
- 1144 St. Laurent, L. C., Toole, J. M., & Schmitt, R. W. (2001). Buoyancy forcing by turbulence  
1145 above rough topography in the abyssal Brazil Basin. *J. Phys. Oceanogr.*, *31*(12),  
1146 3476–3495. doi: 10.1175/1520-0485(2001)031<3476:BFBTAR>2.0.CO;2
- 1147 Su, Z., Wang, J., Klein, P., Thompson, A. F., & Menemenlis, D. (2018). Ocean subme-  
1148 soscales as a key component of the global heat budget. *Nat. Commun.*, *9*(1), 1–8. doi:  
1149 10.1038/s41467-018-02983-w
- 1150 Talley, L. D. (2013). Closure of the global overturning circulation through the Indian, Pacific,  
1151 and southern oceans. *Oceanography*, *26*(1), 80–97. doi: 10.5670/oceanog.2013.07
- 1152 Tamsitt, V., Drake, H. F., Morrison, A. K., Talley, L. D., Dufour, C. O., Gray, A. R., ...  
1153 Weijer, W. (2017, dec). Spiraling pathways of global deep waters to the surface of the  
1154 Southern Ocean. *Nat. Commun.*, *8*(1). doi: 10.1038/s41467-017-00197-0
- 1155 Thomas, L. N., Taylor, J. R., Ferrari, R., & Joyce, T. M. (2013, jul). Symmetric instability  
1156 in the Gulf Stream. *Deep. Res. Part II Top. Stud. Oceanogr.*, *91*, 96–110. doi: 10.1016/  
1157 j.dsr2.2013.02.025
- 1158 Thorpe, S. A., & Liu, Z. (2009). Marginal instability? *J. Phys. Oceanogr.*, *39*(9), 2373–2381.  
1159 doi: 10.1175/2009JPO4153.1
- 1160 Toggweiler, J. R. (1994). The Ocean’s Overturning Circulation. *Phys. Today*, *47*(11),  
1161 45–50. doi: 10.1063/1.881425
- 1162 Tomczak, M., & Large, D. G. B. (1989). Optimum multiparameter analysis of mixing in  
1163 the thermocline of the eastern Indian Ocean. *J. Geophys. Res.*, *94*(C11), 16141. doi:  
1164 10.1029/jc094ic11p16141
- 1165 Trossman, D. S., Arbic, B. K., Garner, S. T., Goff, J. A., Jayne, S. R., Metzger, E. J.,  
1166 & Wallcraft, A. J. (2013). Impact of parameterized lee wave drag on the energy  
1167 budget of an eddying global ocean model. *Ocean Model.*, *72*, 119–142. doi: 10.1016/  
1168 j.ocemod.2013.08.006
- 1169 Tulloch, R., Ferrari, R., Jahn, O., Klocker, A., Lacasce, J., Ledwell, J. R., ... Watson, A.  
1170 (2014). Direct estimate of lateral eddy diffusivity upstream of drake passage. *J. Phys.*  
1171 *Oceanogr.*, *44*(10), 2593–2616. doi: 10.1175/JPO-D-13-0120.1
- 1172 Voet, G., Alford, M. H., MacKinnon, J. A., & Nash, J. D. (2020). Topographic Form  
1173 Drag on Tides and Low-Frequency Flow: Observations of Nonlinear Lee Waves over  
1174 a Tall Submarine Ridge near Palau. *J. Phys. Oceanogr.*, 1489–1507. doi: 10.1175/  
1175 jpo-d-19-0257.1
- 1176 Vosper, S. B. (2004). Inversion effects on mountain lee waves. *Q. J. R. Meteorol. Soc.*,  
1177 *130*(600 PART A), 1723–1748. doi: 10.1256/qj.03.63
- 1178 Walin, G. (1982). On the relation between sea-surface heat flow and thermal circulation in  
1179 the ocean. *Tellus*, *34*(2), 187–195. doi: 10.3402/tellusa.v34i2.10801
- 1180 Waterhouse, A. F., Mackinnon, J. A., Nash, J. D., Alford, M. H., Kunze, E., Simmons,  
1181 H. L., ... Lee, C. M. (2014). Global patterns of diapycnal mixing from measurements  
1182 of the turbulent dissipation rate. *J. Phys. Oceanogr.*, *44*(7), 1854–1872. doi: 10.1175/  
1183 JPO-D-13-0104.1
- 1184 Waterman, S., Naveira Garabato, A. C., & Polzin, K. L. (2013). Internal waves and  
1185 turbulence in the antarctic circumpolar current. *J. Phys. Oceanogr.*, *43*(2), 259–282.  
1186 doi: 10.1175/JPO-D-11-0194.1
- 1187 Waterman, S., Polzin, K. L., Garabato, A. C., Sheen, K. L., & Forryan, A. (2014). Suppres-  
1188 sion of internal wave breaking in the antarctic circumpolar current near topography.  
1189 *J. Phys. Oceanogr.*, *44*(5), 1466–1492. doi: 10.1175/JPO-D-12-0154.1
- 1190 Watson, A. J., Ledwell, J. R., Messias, M. J., King, B. A., Mackay, N., Meredith, M. P.,  
1191 ... Naveira Garabato, A. C. (2013). Rapid cross-density ocean mixing at mid-depths  
1192 in the Drake Passage measured by tracer release. *Nature*, *501*(7467), 408–411. doi:

- 1193 10.1038/nature12432  
1194 Wenegrat, J. O., & Thomas, L. N. (2020). Centrifugal and symmetric instability during  
1195 Ekman adjustment of the bottom boundary layer. *J. Phys. Oceanogr.*, *50*, 1793–1812.  
1196 doi: 10.1175/JPO-D-20-0027.1
- 1197 Whalen, C. B., de Lavergne, C., Naveira Garabato, A. C., Klymak, J. M., MacKinnon,  
1198 J. A., & Sheen, K. L. (2020). Internal wave-driven mixing: governing processes and  
1199 consequences for climate. *Nat. Rev. Earth Environ.*, *1*(11), 606–621. doi: 10.1038/  
1200 s43017-020-0097-z
- 1201 Winters, K. B., & Armi, L. (2012). Hydraulic control of continuously stratified flow over  
1202 an obstacle. *J. Fluid Mech.*, *700*, 502–513. doi: 10.1017/jfm.2012.157
- 1203 Winters, K. B., & Armi, L. (2014). Topographic control of stratified flows: Upstream jets,  
1204 blocking and isolating layers. *J. Fluid Mech.*, *753*, 80–103. doi: 10.1017/jfm.2014.363
- 1205 Wunsch, C., & Ferrari, R. (2004). Vertical Mixing, Energy, and the General Circulation of  
1206 the Oceans. *Annu. Rev. Fluid Mech.*, *36*(1), 281–314. doi: 10.1146/annurev.fluid.36  
1207 .050802.122121
- 1208 Zika, J. D., Sallee, J. B., Meijers, A. J., Naveira-Garabato, A. C., Watson, A. J., Messias,  
1209 M. J., & King, B. A. (2020). Tracking the spread of a passive tracer through Southern  
1210 Ocean water masses. *Ocean Sci.*, *16*(2), 323–336. doi: 10.5194/os-16-323-2020

# Supporting Information for “Enhanced upwelling of Antarctic Bottom Water by topographic interaction of water mass interfaces”

L. E. Baker<sup>1</sup>, A. Mashayek<sup>1</sup>, A. C. Naveira Garabato<sup>2</sup>

<sup>1</sup>Imperial College London, United Kingdom

<sup>2</sup>University of Southampton, Southampton, United Kingdom

## Contents of this file

1. Captions for Movies S1 to S3

## Additional Supporting Information (Files uploaded separately)

1. Movies S1-S3

## Introduction

Movies corresponding to selected panels of figures 3, 5, and 6 in the main text are provided and captioned here to further illustrate the complex dynamics of water masses and flow-topography interaction processes in the Drake Passage. The movies are created using model output from the Drake Passage model described fully in Appendix A of the main text.

**Movie S1.** 30 day animation of daily average fields corresponding to panels a,b,e,f,g,h of figure 3. (a,b) Neutral density, (c,d) salinity, and (g,h) stratification  $N^2$  at (left column)

---

3600 m depth and (right column)  $-58^\circ$  N. White and blue dashed lines show correspondence between columns.

**Movie S2.** 10 day animation of hourly average fields corresponding to panels a,b,c,d of figure 5. (a) Richardson number, (b) vertical diffusivity, (c) stratification, (d) squared vertical shear of horizontal velocities and (e) salinity, all at  $-57^\circ$  N.

**Movie S3.** 10 day animation of hourly average fields corresponding to the top three and bottom rows of figure 6. (a) Salinity at 3600 m depth, with white dashed line indicating the section shown in the remaining panels at  $298.6^\circ$  E. (b) Salinity, (c) stratification and (d) vertical diffusivity.